RETRIEVAL OF INHERENT OPTICAL PROPERTIES FROM REFLECTANCE SPECTRA IN OCEANIC AND COASTAL WATERS WITH NEURAL NETWORK MODELING

by

IOANNIS IOANNOU

A dissertation submitted to the Graduate Faculty in Engineering in partial fulfillment of the requirements for the degree of Doctor of Philosophy, The City University of New York

2011

This manuscript has been read and accepted for the
Graduate Faculty in Engineering in satisfaction of the
dissertation requirement for the degree of Doctor of Philosophy.

Dr. Samir Ahmed

Date — Chair of Examining Committee

Dr. Mumtaz K. Kassir

Date — Executive Officer

Dr. Alexander Gilerson

Dr. Barry Gross

Dr. Fred Moshary

Dr. Tristan Harmel

Dr. Menghua Wang
Supervisory Committee

THE CITY UNIVERSITY OF NEW YORK

Abstract

RETRIEVAL OF INHERENT OPTICAL PROPERTIES FROM REFLECTANCE SPECTRA IN OCEANIC AND COASTAL WATERS WITH NEURAL NETWORK MODELING

by

Ioannis Ioannou

Adviser: Professor Samir Ahmed

Co – adviser: Professor Alex Gilerson

Retrieving inherent optical properties of water from remote sensing multispectral reflectance measurements is difficult due to both the complex nature of the forward modeling and the inherent nonlinearity of the inverse problem. In such cases, neural network (NN) techniques have a long history in inverting complex nonlinear systems. In this study we present the construction and validation of three NN's working in parallel to model the inverse problem for both case 1 and case 2 waters. The first NN is used to relate the remote sensing reflectance at available MODIS visible wavelengths (except the 678 nm fluorescence channel) to the absorption and backscatter coefficients at 442nm (peak of phytoplankton absorption). The second NN separates algal and non-algal absorption components, outputting the ratio of algal to non-algal absorption and the third, in a similar manner, outputs the ratio of non-algal particulate to dissolved absorption coefficient. With the outputs of these statistically derived networks we can thereafter analytically obtain the absorbing properties of the three known major water components. These include the color dissolved organic matter (CDOM), phytoplankton, and non-algal particulates (NAP).

The resulting synthetically trained algorithm is tested using both the NASA Bio-Optical Marine Algorithm Data set (NOMAD), as well as our own field data sets from the Chesapeake Bay and Long Island Sound, New York. Very good agreement is obtained, when the retrievals are compared with the measurements of both the NOMAD dataset as well as our field data. Furthermore we apply our algorithm on satellite imagery and finally we test to what extent the empirical relationships used to describe the IOPs can be applied.

ΣΤΗΝ ΟΙΚΟΓΕΝΕΙΑ ΜΟΥ

Acknowledgements

First I would like to thank Prof. Samir Ahmed who gave me the opportunity to continue my studies at CCNY with full financial support after receiving my Bachelor degree in electrical engineering here at CCNY. From my interaction with him, during the past 5 years, I attained knowledge, beyond science and engineering that will very much benefit me in the years to come.

Also working as part of a team, this thesis has contributions from my many colleagues including professors and research associates in the Optical Remote Sensing Lab at City College. It has been a great opportunity for me to have worked side by side with Prof. Alex Gilerson who has a very broad experience in this field. I would also like to thank Prof. Barry Gross for many discussions that helped clarify, organize and furnish my papers. Last but not least I would like to thank Prof. William Rossow for his help and advice during the neural network algorithm development.

I also would like to thank W. Balch, F. Chavez, L. Harding, S. Hooker, G. Mitchell, R. Morrison, F. Muller-Karger, N. Nelson, D. Siegel, A. Subramaniam, R. Stumpf, and all of their co-investigators for their contribution to SeaBASS data. The success of the study presented here heavily relies on the SeaBASS dataset.

This manuscript is also dedicated to my family and their consistent and unconditional love and support. No words can express my appreciation for what they have given to me.

Table of Contents

CHAPTER 1 INTRODUCTION **1**

CHAPTER 2 WATER OPTICAL PROPERTIES **8**

2.1 THEORETICAL BACKGROUND 9

2.1.1 Absorption and scattering coefficient *9*

2.1.2 Reflectance *11*

2.2 OPTICALLY SIGNIFICANT WATER CONSTITUENTS AND THEIR BIO-OPTICAL MODELING 12

2.2.1 Optically significant constituents *12*

2.2.2 Relationship between R_{rs} and IOP's *13*

2.2.3 Water contribution *14*

2.2.4 Algal component *14*

2.2.5 Non-algal Particulates *17*

2.2.6 Colored dissolved organic matter *19*

2.2.7 Accumulation of the Dataset *20*

2.3 FIELD MEASUREMENTS IN CHESAPEAKE BAY AND LONG ISLAND 25

2.3.1 Optical instruments *25*

2.3.2 Variability of the measurements *27*

2.4 SUMMARY 29

CHAPTER 3 INVERSION TECHNIQUES **31**

3.1 INVERSE PROBLEMS 31

3.2 ESTABLISHED ALGORITHMS 32

3.2.1 Semi analytical linear matrix inversion *32*

3.2.2 Quasi Analytical Algorithm (QAA) *33*

3.3 NEURAL NETWORK INVERSION SCHEME 33

3.3.1 Nonlinear model: the multilayer perceptron neural network *33*

3.3.2 Optimization algorithm: Bayesian Regularization *36*

3.3.3 Algorithm Description *37*

3.3.4 Normalizing the Data *39*

3.3.5 Architecture *41*

3.3.6 Algorithm Implementation *42*

3.4 SUMMARY 45

CHAPTER 4 APPLICATION OF THE IOP INVERSION ALGORITHMS 47

4.1 VALIDATING THE NEURAL NETWORK 47

4.1.1 Simulated Data *47*

4.2 COMPARISON OF THE ALGORITHMS 62

4.2.1 Field Data *62*

4.2.2 Implementation on Satellite Data *69*

4.3 SUMMARY 88

CHAPTER 5 HOW WELL DO THE EMPIRICAL RELATIONSHIPS DESCRIBE THE IOPS? 89

5.1 PREDICTING THE ABSORPTION AT MULTISPECTRAL VISIBLE BANDS 89

5.1.1 Empirical relationships for algal, non-algal particulate, and CDOM absorptions *89*

5.1.2 Estimating the absorption at MODIS bands *91*

5.2 PARAMETERIZATION OF THE ALGAL NORMALIZED SPECIFIC ABSORPTION 97

5.2.1 Parameterization for multispectral satellite bands *97*

5.2.2 Solving for the size parameter, Sf and [Chl] *103*

5.3 IMPLEMENTATION OF THE MODEL ON MODIS DATA 109

5.3.1 Comparing our results with the MODIS [Chl] product *109*

5.3.2 Exploring the influence of the non- algal components on the MODIS [Chl] product *114*

5.5 SUMMARY 117

CHAPTER 6 SUMMARY OF THE STUDY 119

BIBLIOGRAPHY 121

List of Tables

Table 3.1. Mean and standard deviation of the inputs for the α_{pg} and $b_{b\text{-}p}$ network. .. 42

Table 3.2. Mean and standard deviation of the inputs for the network $R_{a_{dg}}^{a_{ph}}(442)$ 42

Table 3.3. Mean and standard deviation of the inputs for the network $R_{a_g}^{a_{dm}}(442)$ 42

Table 3.4. Mean and standard deviation of the outputs in the simulated dataset. The values in the parenthesis are the product of the fitting to the field data (refer to section 4.1.2). 45

Table 4.1. Statistics of comparison for Figures 4.1 and 4.2 without noise. The values in the parenthesis indicate the results when $a_{ph}(442)$ is at least 10% of $a_{dg}(442)$..... 51

Table 4.2. Statistics of comparison for Figures 4.1 and 4.2 when 10% noise is added at each R_{rs}. The values in the parenthesis indicate the results when $a_{ph}(442)$ is at least 10% of $a_{dg}(442)$..... 51

Table 4.3. Statistics of comparison for Figures 4.1 and 4.2 when 20% noise is added at each $R_{rs.}$ The values in the parenthesis indicate the results when $a_{ph}(442)$ is at least 10% of $a_{dg}(442)$..... 51

Table 4.4. Statistics of comparison for Figure 4.3 for $a_{dm}(442)$. The values in the parenthesis indicate the results when $a_{dm}(442)$ is at least 10% of $a_g(442)$ and vice versa. The noise, ε that was added to the reflectance, is indicated in the first column. 53

Table 4.5. Statistics of comparison for Figure 4.3 for $a_g(442)$. The values in the parenthesis indicate the results when $a_{dm}(442)$ is at least 10% of $a_g(442)$ and vice

versa. The noise, ε that was added to the reflectance, is indicated in the first column. 53

Table 4.6. Statistics of comparison for Figure 4.5 Chesapeake Bay and Long Island NY. 58

Table 4.7. Statistics of comparison for Figures 4.4 and 4.6 for the NOMAD dataset. The values in the parenthesis for $a_{ph}(442)$ and $a_{dg}(442)$ indicate the statistics after the 'Fitting'(see text). 59

Table 4.8. Statistics of comparison for the NOMAD dataset Figure 4.7 for $a_{dm}(442)$ and $a_g(442)$ and $a_p(442)$, m^{-1} 60

Table 4.9. Statistics of comparison of the three algorithms for $a(442)$ m^{-1}. N is the number of successful retrievals of the SAA (with the 10 and 20% criterion) and QAA. 62

Table 4.10. Statistics of comparison of the three algorithms for $a_{ph}(442)$ m^{-1}. N is the number of successful retrievals of the SAA (with the 10 and 20% criterion) and QAA. 64

Table 4.11. Statistics of comparison of the three algorithms for $a_{dg}(442)$ m^{-1}. N is the number of successful retrievals of the SAA (with the 10 and 20% criterion) and QAA. 66

Table 4.12. Statistics of comparison of the three algorithms for $b_b(442)$ m^{-1}. N is the number of successful retrievals of the SAA (with the 10 and 20% criterion) and QAA. 66

Table 5.1. Statistics for Figure 5.2. Units in m^{-1} 93

Table 5.2. Statistics for Figure 5.3. Units in m^{-1} 94

Table 5.3. Statistics for Figure 5.4. Units in m^{-1} 95

Table 5.4. Statistics for Figure 5.5. Units in m^{-1} 96

Table 5.5. Statistics for Figure 5.8. Units in m^{-1} 101

Table 5.6. Statistics for Figure 5.9. Units in m^{-1} 102

Table 5.7. Statistics for Figure 5.11. Units in m^{-1} 107

Table 5.8. Statistics for Figure 5.12. Units in m^{-1} 108

List of Figures

Fig. 2.1. Geometry used to define IOP's 10

Fig. 2.2. Diagram of optically significant constituents 12

Fig. 2.3. The specific absorption of two phytoplankton species, the pico-plankton absorption (black) and the micro-plankton absorption (red). A combination of these two absorptions is used in the construction of the simulated dataset. 15

Fig. 2.4. The spectral variation of the NAP absorption coefficient with the minimum and maximum spectral slopes, S_{dm} (nm^{-1}). Both absorption spectra are normalized at 440 nm. 18

Fig. 2.5. The spectral variation of the CDOM absorption coefficient with the minimum and maximum spectral slopes, S_g (nm^{-1}). Both absorption spectra are normalized at 440 nm..... 20

Fig. 2.6. Normalized distributions of the simulated dataset parameters (black line) and the NOMAD dataset (grey). Noticeably the measurements fall within the range of our simulations. 22

Fig. 2.7. Relationships of the three components at the reference wavelength used in the simulations according to the distribution functions used in our dataset. The black dots indicate the simulated datasets while the grey points indicate the measurements of the NOMAD dataset. 23

Fig. 2.8. Comparison between in situ and simulated dataset as indicated in IOCCG report 5 [2006]. The field data generally fall within our simulations. 24

Fig. 2.9. Map of Chesapeake Bay (left) and Long Island (Right) representing the locations of the 85 stations sampled. 25

Fig. 2.10. Near surface measured absorption coefficient (upper) and attenuation coefficients (lower) as a function of wavelength for all the 85 stations. The Red lines represent the Long Island measurements while the Black lines represent the Chesapeake Bay Stations. 28

Fig. 2.11. Measured spectral reflectance just below the surface for all the 85 stations. The Red lines represent the Long Island Sound measurements while the Black lines represent the Chesapeake Bay Stations..... 29

Fig. 3.1 General architecture of the MLP (a). Exact architecture of the three one layer MLPs that are used model the inverse problem of Ocean color for MODIS(b)..... 35

Fig. 3.2 Algorithm description and levels of products as explained in section 3.3.3. 39

Fig. 4.1. Performance of the neural network on the part of our simulated dataset that was not used in the training stage. Inverted $a(442)$ m^{-1} (left columns) and $b_b(442)$ m^{-1} (right) (x-axis) plotted against the "known" values from our simulated dataset. Noise levels, ε, up to 20% (the top row is ε=0%) were added at each R_{rs}. The corresponding statistics are shown in Tables 4.1 – 4.3 below. 48

Fig. 4.2. Performance of the neural network on the part of our simulated dataset that was not used in the training stage. Inverted $a_{ph}(442)$ m^{-1} (left columns) and $a_{dg}(442)$ m^{-1} (right) (x-axis) plotted against the "known" values for these parameters from our simulated dataset. Noise levels, ε, up to 20% (the top row is ε=0%) were added at

each R_{rs}. The grey dots indicate the cases where $a_{ph}(442)$ is less than 10% of $a_{dg}(442)$. The corresponding statistics are shown in Tables 4.1 - 4.3 below. 50

Fig. 4.3. Performance of the neural network on the part of our simulated dataset that was not used in the training stage. Inverted $a_{dm}(442)$ m^{-1} (left columns) and $a_g(442)$ m^{-1} (right) (x-axis) plotted against the "known" values for these parameters from our simulated dataset. Noise levels, ε, up to 30% (the top row is ε=0%) were added at each R_{rs}. The grey dots indicate the cases where $a_{dm}(442)$ is less than 10% of $a_g(442)$ and vice versa. See Table 4.4 and 4.5 for the corresponding statistics..... 52

Fig. 4.4. Inverted IOP from the neural network (x-axis) plotted against the in situ values from the NOMAD dataset for $a(442)$ m^{-1}, $b_b(442)$ m^{-1} and K_d (442) m^{-1}. The lower graphs illustrate the relationship of $K_d(442)$ $m^{-1}$and $a(442)$ m^{-1} and $b_b(442)$ m^{-1} (left) and $K_d\{a(442),b_b(442)\}$ m^{-1} from Eq. (4.3) right. Refer to Table 4.7 for statistics..... 56

Fig. 4.5. Inverted IOP's from the neural network (x-axis) plotted against the in situ values for our field dataset for $a(442)$ m^{-1} (upper) and $b_b(442)$ m^{-1}(lower). The statistics are shown in the parenthesis in Table 4.6. 57

Fig. 4.6. Inverted IOP's from the neural network (x-axis) plotted against the in situ values from the NOMAD dataset for a_{ph} (442) $m^{-1}$and a_{gd} (442) m^{-1}. The first row represents the outputs of the neural network before "fitting" the output with the measurements (see text). The second row represents the results after the adjustment with the field data. Statistics are shown in Table 4.7..... 60

Fig. 4.7. Inverted IOP's from the neural network (x-axis) plotted against the in situ values from the NOMAD dataset for a_{dm} (442) m^{-1} (upper plot) and a_g (442) m^{-1} (middle) and a_p (442) m^{-1} (lower). The corresponding statistics are shown in Table 4.8..... 61

Fig. 4.8. Retrievals of the SAA, QAA and neural network (x-axis) vs. in-situ measurement for a(442) m^{-1}..... 63

Fig. 4.9. Retrievals of the SAA, QAA, and neural network (x-axis) vs. in-situ measurement for a_{ph}(442) m^{-1}..... 65

Fig. 4.10. Retrievals of the SAA, QAA and neural network (x-axis) vs. the in-situ measurement for a_{dg}(442) m^{-1}..... 67

Fig. 4.11. Retrievals of the SAA, QAA and neural network (x-axis) vs. in-situ measurement for b_b(442) m^{-1}. 68

Fig. 4.12. Retrievals of the neural network of the total absorption coefficient, a(442) m^{-1}(upper), and the total backscattering coefficient b_b(442) m^{-1} (lower). The color bar is adjusted in the smaller images on the left to make the turbid regions visible..... 71

Fig. 4.13. Retrievals of the SAA of the total absorption coefficient, a(442), m^{-1} (upper), and the total backscattering coefficient b_b(442) m^{-1} (lower)..... 72

Fig. 4.14. The NN retrieval of a(442) m^{-1} x-axis plotted against the SAA (top) and QAA (lower). R^2=99.16 with a slope of 0.9421 and an intercept of -0.0945 for the SAA, and R^2=0.9915, a slope of 1.0365 and an intercept of -0.0359 for the QAA. All the available retrievals for all algorithms are shown. 73

Fig. 4.15. The NN retrieval of $b_b(442)$ m^{-1} x-axis plotted against the SAA left and QAA right. R^2= 0.9822 with a slope of 0.8854 and an intercept of -0.298 for the SAA, and R^2= 0.9866, a slope of 0.9426 and an intercept of -0.18 for the QAA. All the available retrievals for all algorithms are shown. 74

Fig. 4.16. Retrievals of the neural network of the phytoplankton absorption coefficient, $a_{ph}(442)$ m^{-1} (upper), and the non-algal and dissolved absorption coefficient $a_{dg}(442)$ m^{-1} (lower). The color bar is adjusted in the smaller images on the left to make the turbid regions visible..... 75

Fig. 4.17. Retrievals of the SAA of the phytoplankton absorption coefficient, $a_{ph}(442)$ m^{-1} (upper), and the non-algal and dissolved absorption coefficient $a_{dg}(442)$ m^{-1} (lower)..... 76

Fig. 4.18. The NN retrieval of $a_{dg}(442)$ m^{-1} x-axis plotted against the SAA (top) and QAA (lower). R^2= 0.9806 with a slope of 0.8569 and an intercept of -0.1179 for the SAA, and R^2= 0.9620, a slope of 1.0143 and an intercept of 0.0948 for the QAA. All the available retrievals for all algorithms are shown. 77

Fig. 4.19. The NN retrieval of $a_{ph}(442)$ m^{-1} x-axis plotted against the SAA (top) and QAA (lower). R^2= 0.6893 with a slope of 1.0641 and an intercept of -0.2264 for the SAA, and R^2=0.5949, a slope of 1.0802 and an intercept of -0.2648 for the QAA. All the available retrievals for all algorithms are shown. 78

Fig. 4.20. Retrievals of the neural network of the non-algal particulate absorption coefficient, $a_{dm}(442)$ m^{-1}. The color bar is adjusted in the left image to make the turbid regions visible..... 79

Fig. 4.21. Retrievals of the neural network of the dissolved absorption coefficient $a_g(442)$ m^{-1}. The color bar is adjusted in the left image to make the turbid regions visible. 80

Fig. 4.22. The MODIS [*Chl*] product x-axis plotted against the NN retrieval of $a_{ph}(442)$ m^{-1} divided by the MODIS [*Chl*] mg m^{-3} (specific absorption of algae). Specific absorptions of less than 0.01 which consistently appear in the higher [*Chl*] mg m^{-3} are probably due to CDOM contaminated [*Chl*] mg m^{-3} retrievals. Three models are shown from [*Morel,* 1991] (magenta), [Bricaud, 1995] (red) and [*IOCCG Dataset,* 2003] (cyan)..... 82

Fig. 4.23. The NN retrieval of $a_{ph}(442)$ m^{-1} x-axis plotted against the MODIS [*Chl*] mg m^{-3} product. The disagreement of the two algorithms in the higher [*Chl*] mg m^{-3} (red ellipse) values indicates case 2 waters. There is a very good agreement between the two algorithms in the [*Chl*] mg m^{-3} for all other cases indicating that the all constituents increase in a similar manner which indicates case 1 waters. 83

Fig. 4.24. The MODIS measurement of $R_{rs}(667)$ sr^{-1} x-axis plotted against the NN retrieval of $a_{dm}(442)$ m^{-1}. The red line indicates the relationship between the two parameters. 84

Fig. 4.25. The MODIS measurement of $R_{rs}(667)$ sr^{-1} x-axis plotted against the NN retrieval of $a_g(442)$ m^{-1}. The two ellipses indicate Case 1(blue) and Case 2(red) waters. The apparent relationship between the $R_{rs}(667)$ sr^{-1} and $a_g(442)$ m^{-1} for the low absorbing waters (usually case 1) is most likely due to the co-variation of the dissolved substance with the other scattering constituents 85

Fig. 4.26. The MODIS Blue Green ratio $R_{rs}(488)/ R_{rs}(547)$ x-axis plotted against the NN retrieval of $a_{dm}(442)$ m^{-1}. The relationship between these two parameters is weak as the non-algal particulate absorption is not dominant..... 86

Fig. 4.27. The MODIS Blue Green ratio $R_{rs}(488)/ R_{rs}(547)$ x-axis plotted against the NN retrieval of $a_g(442)$ m^{-1}. The relationship between these two parameters is strong as the CDOM absorption dominates the blue part of the spectrum. 87

Fig. 5.1. Phytoplankton, CDOM and NAP absorptions used in this chapter to predict the absorption of these three components at other wavelengths. All functions are normalized at 442 nm (in conformity with the outputs of the NN algorithm; Chapter 3 Section 3.3). 90

Fig. 5.2. Inverted IOP's (x-axis) plotted against the in situ values from the NOMAD dataset for $a_{dm}(412)$ m^{-1}, a_{ph} (412) m^{-1}, a_g (412) m^{-1} and $a(412)$ m^{-1}. The parameters are extrapolated to 412 nm from the neural network retrieved parameters at 442 nm and the empirical functional shapes discussed in this chapter. 93

Fig. 5.3. Inverted IOP's (x-axis) plotted against the in situ values from the NOMAD dataset for $a_{dm}(488)$ m^{-1}, a_{ph} (488) m^{-1}, a_g (488) m^{-1} and $a(488)$ m^{-1}. The parameters are extrapolated to 488nm from the neural network retrieved parameters at 442nm and the empirical functional shapes described in this chapter. 94

Fig. 5.4. Inverted IOP's (x-axis) plotted against the in situ values from the NOMAD dataset for $a_{dm}(547)$ m^{-1}, a_{ph} (547) m^{-1}, a_g (547) m^{-1} and $a(547)$ m^{-1}. The parameters are extrapolated to 547nm from the neural network retrieved parameters at 442nm and the empirical shapes described in this chapter. Evidently there is a considerable

difference in the estimates of the algal absorption at this wavelength for the two functional shapes. Clearly the optimum functional shape lies between that for each of the species. 95

Fig. 5.5. Inverted IOP's (x-axis) plotted against the in situ values from the NOMAD dataset for $a_{dm}(667)$ m^{-1}, a_{ph} (667) m^{-1}, a_g (667) m^{-1} and $a(667)$ m^{-1}. The parameters are extrapolated to 667nm from the neural network retrieved parameters at 442nm and the empirical functional shapes described in this chapter. Evidently there is a considerable difference in estimates of the algal absorption at this wavelength between the functional two shapes. 96

Fig. 5.6. Algal absorption normalized at 442 nm (normalized specific absorption) as a function of wavelength for all available NOMAD data. The normalized at 442nm absorption of micro- and pico- plankton are also shown. This is the expected range of change of the normalized specific algal absorption. The black lines represent the NOMAD dataset measurement at 442nm and are extrapolated to the other wavelengths using the parameterization from Eqs. (5.3)-(5.7). Also see Figure 5.7.. 99

Fig. 5.7. Specific absorption of algae normalized at 442nm (y-axis) as a function of $a_{ph}(442)$ m^{-1} , Eqs. (5.3) - (5.7). The $a_{ph}(442)$ m^{-1} is the measurement from the NOMAD dataset. 100

Fig. 5.8. Predicted algal absorption at 412, 488, 547 and 667 nm using the modeling of $a_{ph}(442)$ m^{-1} described in Eq. (5.3), Eq. (5.5), Eq. (5.6) and Eq. (5.7) and the retrieved $a_{ph}(442)$ m^{-1} from the neural network algorithm. 101

Fig. 5.9. Predicted total absorption at 412, 488, 547 and 667 nm using the modeling of $a_{ph}(442)$ m^{-1} described in Eq. (5.3), Eq. (5.5), Eq. (5.6) and Eq. (5.7) and the non-algal shapes described in Eq. (5.1) and Eq. (5.2) and the retrieved parameters of $a_g(442)$ m^{-1}, $a_{dm}(442)$ m^{-1} and $a_{ph}(442)$ m^{-1} from the neural network algorithm. 102

Fig. 5.10. Relationship of the size parameter, S_f (Eq. 5.9), and [*Chl*] mg m^{-3} (Eq 5.11) (upper figures) and $a_{ph}(442)$ m^{-1} (lower figures) in both the linear (left) and logarithmic domain (right). The size parameter is reduced as a function of these two parameters in agreement with previous studies [*Morel,* 1991; *Bricaud et al.*, 1995]. 106

Fig. 5.11. Predicted algal absorption at 412, 488, 547 and 667 nm from Eq. (5.9) and the retrieved $a_{ph}(442)$ m^{-1} from the neural network algorithm. 107

Fig. 5.12. Predicted total absorption at 412, 488, 547 and 667 nm using the modeling of $a_{ph}(442)$ m^{-1} described in Eq. (5.9) and the non-algal shapes described in Eq. (5.1) and Eq. (5.2) and the retrieved parameters of $a_g(442)$ m^{-1}, $a_{dm}(442)$ m^{-1} and $a_{ph}(442)$ m^{-1} from the neural network algorithm. 108

Fig. 5.13. Image of the [*Chl*] mg m^{-3} based on the size parameter, S_f, parameterization as described Eq. (5.11) and Eq.(5.12). The color bars next to each map indicate the range of [*Chl*] mg m^{-3}. 110

Fig. 5.14. Image of the MODIS [*Chl*] mg m^{-3} product [*O'Reilly et al.*, 1998]. The color bars next to each map indicate the range of [*Chl*] mg m^{-3}..... 111

Fig. 5.15. The [*Chl*] mg m^{-3} based on the size parameter, S_f, parameterization as described in Eq. (5.11) and Eq. (5.12) vs. the MODIS [*Chl*] mg m^{-3} product (y-axis). 112

Fig. 5.16. Percent Difference Eq. (5.13) of the derived [*Chl*] mg m^{-3} using the size parameter, S_f and the MODIS [*Chl*] mg m^{-3} product as shown in Eq. (5.12). 113

Fig. 5.17. Percent Difference Eq. 5.13 as a function of the log(a_{dm}(442) /a_g(442)). Clearly the underestimation/overestimation is a function of the contribution of the constituents other than phytoplankton. 115

Fig. 5.18. Percent Difference Eq. 5.13 as a function of the log (a_{ph}(442) /a_g(442)). Clearly the underestimation/overestimation depends on the presence of CDOM.... 116

Fig. 5.19. Percent Difference Eq. 5.13 as a function of the log (a_{ph}(442) /a_{dm}(442)). There is no clear relationship that can explain the difference of the two algorithms by the non algal particulate absorptions..... 117

Chapter 1 Introduction

A main goal of ocean color remote sensing is to relate remote sensing reflectance [*Gordon and Morel*, 1983], R_{rs} sr^{-1}, an apparent optical property (AOP) [*Tyler and Preisendorfer*, 1962; *Preisendorfer*, 1976], directly to inherent optical properties (IOP's) [*Tyler and Preisendorfer*, 1962; *Preisendorfer*, 1976], (e.g. absorptions, scattering coefficients, etc) of interest, leading to the meaningful estimation of physical components, including color dissolved organic matter, CDOM (often referred to as gelbstoff), phytoplankton, and non-algal particulates, NAP, such as dead algal cells (detritus) and inorganic particles, typically originating from rivers and run-offs from land.

According to the optical classification *Morel and Prieur* [1977], oceanic waters may be characterized as case 1, where the optical properties are influenced by substances that co-vary with chlorophyll concentration, [*Chl*], or as case 2, by substances which do not co-vary with [*Chl*], but also affect optical properties. In case 1 waters adequate retrievals of the desired properties can be achieved using empirical algorithms [*Austin and Petzold*, 1981; *Gordon et al.*, 1983; *Sathyendranath et al.*, 1994; *Lee et al.*, 1998; *O'Reilly et al.*,1998; *Sydor et al.*, 1998*; Loisel et al.*, 2001]. These algorithms are generally structurally similar, whereby AOP's, usually R_{rs} sr^{-1}, are related to the desired water constituents through simple or multiple regressions. Pigment retrievals with empirical algorithms in case 1 waters have achieved reasonable results [*Gordon et al.*, 1983b]. However, substances not co-varying with chlorophyll in

case 2 waters have caused the retrieval of pigment concentrations to have inaccuracies as high as 133% [*Carder et al*., 1991].

To address the complexity of case 2 waters, Semi-analytical ocean-color inversion algorithms (SAA) [*Roesler and Perry*, 1995; *Hoge and Lyon* 1996; *Garver and Siegel*, 1997; *Carder et al.*, 1999; *Wang et al.*, 2005], are often used and based on approximate solutions to the radiative transfer Equation, (RTE), (the analytical part) and assumptions regarding the spectral shapes of IOPs (the empirical part). Unlike purely empirical algorithms, SAA's are generally less sensitive to disparate geographical regions or water type. The performance of these algorithms, however, relies on the correct modeling of the RTE and on accurate spectral models for the absorption coefficients of each individual constituent present in the water. Because these are not necessarily known accurately, retrievals are not always successful.

The Linear Matrix Inversion (LMI) algorithm [*Hoge and Lyon*, 1996], a SAA, uses remote-sensing reflectance at three wavelengths to simultaneously derive three major unknowns algebraically. Due to its linear matrix nature, it is efficient in processing satellite images. The algorithm uses the remotely sensed reflectance, R_{rs}, propagated through the air / water interface, into a semi-analytic reflectance model developed by *Gordon et al.* [1988]. The present version of the algorithm that is optimized for use with satellite data uses only three inputs, $R_{rs}(412)$, $R_{rs}(490)$ and $R_{rs}(555)$. The algorithm also has four empirical parameters that determine the spectral shapes of the individual IOP spectrum. Using these empirical relationships we can construct a set of three equations and by inverting the related matrix solve for the amplitude of three parameters, $a_{ph}(\lambda_0)$, $a_{dg}(\lambda_0)$, $b_b(\lambda_0)$. The empirical shapes already

assumed can thereafter be used to estimate the absorption at different wavelengths. The drawbacks of this method are: 1) a real solution is not always possible; 2) it is sensitive to the exact bands chosen for retrieval and 3) sensitive to noise.

The over constrained linear matrix inversion algorithm [*Wang et al.*, 2005] operates in a similar manner and the basic difference between this method compared with that of [*Hoge and Lyon*, 1996] is that the *Gordon et al.* [1988] RTE approximation is solved using more wavelengths than unknowns, with the number of wavelengths not being fixed. This makes the system of equations an over constrained system for which the solution is the best solution in a least-squares sense [*Press et al*., 1992]. The drawback of this inversion, like any other SAA, is that a real solution is not always possible.

Recently, a quasi-analytical algorithm (QAA) [*Lee et al.*, 2002], currently at version 5 [*Lee et al.*, 2009], was presented to address these disadvantages. The QAA does not need *a priori* knowledge of the spectral shape of phytoplankton absorption; instead, it first estimates empirically the total absorption coefficient (a m^{-1}) at a reference wavelength (λ_0) and then analytically calculates the backscattering coefficient (b_b m^{-1}) at the same wavelength based on a combined model of the RTE of *Gordon et al.* [1988] and *Lee et al*. [1999]. Second, the amplitude of these coefficients at other wavelengths is obtained using an empirical estimate of the particulate backscattering spectral shape and the measured remote sensing reflectance. The total absorption coefficient can be further decomposed into the algal and non-algal components. Although robust and continuous in case 1 and case 2 waters, this algorithm is sensitive to noise when applied to satellite imagery.

Another promising method that is widely used in the remote sensing field is the application of neural networks (NN) [*Aires et al.*, 2001; *Aires et al.*, 2004; *Gross et al.*, 1999; *Tanaka et al.*, 2004; *Doerffer and Schiller*, 1999; *Doerffer and Schiller*, 2000; *Doerffer et al.*, 2002; *Schiller and Doerffer*, 2005; *Doerffer and Schiller*, 2006]. The operational MERIS Case 2 water algorithm is a neural network (NN) inversion procedure [*Doerffer and Schiller*, 1999; *Doerffer and Schiller*, 2000; *Doerffer et al.*, 2002; *Schiller and Doerffer*, 2005; *Doerffer and Schiller*, 2006]. This multi layer NN algorithm is capable of inverting the directional above-surface remote-sensing reflectance, R_{rs} sr^{-1}, directly into absorption and scattering coefficients thereafter converting them to concentrations of different constituents present in Case 2 waters. The algorithm accepts the log of the above-surface remote-sensing reflectance at MERIS BANDS 1-7 and 9 (412, 442, 490, 510, 560, 617, 665 and 708 nm), as well as three angles (solar zenith, viewing zenith and azimuth difference) as inputs and provides the log of the pigment absorption (a_{ph} m^{-1}), absorption of gelbstoff and bleached suspended matter (a_{dg}), and scattering coefficient of all particles (b_p), all at 442 nm. The pigment absorption is thereafter transformed into concentration of chlorophyll-*a* and the particulate scattering into total suspended matter dry weight. Together with the gelbstoff absorption, these are the three Case 2 water products of MERIS. In order to detect and flag the erroneous retrievals another neural network is used to reconstruct the R_{rs} sr^{-1} for these retrieved parameters and compare it with the measured R_{rs} sr^{-1}.

To examine the potential for new NNs, in this work we first generate a large diverse simulated dataset that describes both case 1 and case 2 waters [*Ioannou et.al*,

2011] using Hydrolight5^{TM}. Our primary goal in using this simulated representative dataset, is to first relate the nadir-viewing spectral remote-sensing reflectance just above the surface, $R_{rs}(\lambda)$ (at the six visible MODIS bands), to two outputs: the combined particulate/dissolved matter absorption coefficient, a_{pg}, and the particulate backscattering coefficient, $b_{b\text{-}p}$, both at 442 nm. We model this inverse relationship using neural networks. The particulate and dissolved absorption coefficient a_{pg}, and particulate backscattering coefficient, $b_{b\text{-}p}$ are the bulk water properties that are the easiest to obtain, since they are directly related to the radiances measured by any remote sensor. Second, following the multiple steps of QAA, we design two more neural networks: these both relate the same $R_{rs}(\lambda)$ measurement to an estimate of the ratio of algal to non-algal absorption, $R_{a_{dg}}^{a_{ph}}$, and an estimate of the non-algal particulate to dissolved absorption, $R_{a_g}^{a_{dm}}$, both also at 442nm. The outputs of the two latter networks are used, along with the a_{pg} estimate from the first network, to provide us with the capability to analytically solve and obtain a solution for absorption magnitudes of each of the three major constituents a_{ph} , a_g and a_{dm} at 442nm. To our knowledge no previous work attempts to separate the non-algal absorption coefficient a_{dg} into its independent components of a_g and $a_{dm.}$ The resulting synthetically trained algorithm is then tested and retrievals evaluated using both the NASA Bio-Optical Marine Algorithm Data set (NOMAD) [*Werdell and Bailey*, 2005], as well as our own field data sets from the Chesapeake Bay [*Gitelson et al.*, 2007] and Long Island Sound New York [*Zhou et al.*, 2008].

After the successful training and validation of the neural network we are left with 3 absorption amplitudes, the a_{ph}, a_g and a_{dm} at 442nm. These values can then be

used to extrapolate to the other MODIS visible bands based on average shapes as shown in *Babin et al.* [2003] and two phytoplankton shapes (micro- / pico- plankton), *Ciotti et al.* [2002] or by modeling [*Bricaud et al.*,1995]. We then introduce a normalized (at 442 nm) phytoplankton absorption spectral shape at 412, 442, 488, 550 and 667nm. This empirical modeling is based on parameterization of the NASA Bio-Optical Marine Algorithm Data set (NOMAD) [*Werdell and Bailey*, 2005], and provides the phytoplankton absorption, a_{ph}, at each wavelength as a function of the phytoplankton absorption at 442nm. Finally we use the derived empirical relationship between the 442 and 547nm phytoplankton absorption relationship to solve for the size parameter, S_f [*Ciotti et al.*, 2002], and finally using the same formulation obtain an estimate of the [*Chl*] mg m^{-3}.

Chapter 2 discusses the bio-optical modeling of each independent constituent and gives a detailed description of the accumulation of the dataset used to train the neural networks. Chapter 3 performs a brief introduction to the two methods of inversion, localized and global [*Aires et al.*, 2001] and describes in detail the training of each network. Also in Chapter 3, we explain the algorithm that combines the outputs of the three networks to extract useful information about the absorption of each constituent. Chapter 4 validates the neural network algorithm on part of the synthetic dataset and on two *in situ* datasets: the NASA Bio-Optical Marine Algorithm Data set (NOMAD) [*Werdell and Bailey*, 2005] and our own field data sets from the Chesapeake Bay [*Gitelson et al.*, 2007] and Long Island Sound New York [*Zhou et al.*, 2008]. Also in Chapter 4 we use the NASA Bio-Optical Marine Algorithm Data set (NOMAD) [*Werdell and Bailey*, 2005] and satellite imagery to compare the

performance of our algorithm with the quasi-analytical algorithm (QAA) [*Lee et al.*, 2002] and the over constrained linear matrix inversion algorithm [*Wang et al.*, 2005]. Chapter 5 explores the applicability of the empirical relationships that describe each of the IOPs and proposes a parameterization for the algal absorption coefficient that can be used to provide a solution for the size parameter, S_f [*Ciotti et al.*, 2002], and the [*Chl*].

Chapter 2 Water Optical Properties

The optical properties of water can be separated into two categories: inherent and apparent. Inherent optical properties (IOPs), absorption and scattering coefficients, depend only upon the medium while the apparent optical properties (AOPs) such as reflectance are determined by the medium and the geometric structure of the surrounding light field. The overall optical properties of natural waters are determined, in part, by the optically active constituents in water. The AOP's can be computed through the Radiative Transfer Equation (RTE) or approximations of the RTE from empirical models, using the combined IOPs as inputs. These IOPs are obtained from the independent IOPs modeling for each constituent of the water body [*Mobley*, 1994]. These optical properties of the physical constituents forms the basis of retrieving the concentration of the water component of interest such as [*Chl*] mg m^{-3} dissolved substance and mineral particle concentrations, [*NAP*] g m^{-3}, from both surface and satellite based optical remote sensing data [*Morel and Prieur,* 1977*; Roesler and Perry,* 1995].

In-situ field measurements of water optical properties can provide not only the necessary input for light field calculation based on radiative transfer scheme but can also create a valuable database for validation of different bio-optical models and inversion algorithms [*Hamre et al.,* 2004]. Calibration and correction of satellite data also rely on the accurate ground based measurements data obtained for different seasons and locations. Such a database is even more important for coastal waters, where human activities and terrestrial run-offs have a larger impact than the global

nutrition balance on water constituents making it more difficult to predict and depict by traditional simple models. Furthermore, the water constituents and hence water optical properties can vary from oligotrophic, mesotrophic to eutrophic sometimes on scales of meters, which is difficult to resolve with typical 1-km satellite pixels [*Chang et al.,* 2005].

Next, we reproduce here the definitions of the IOPs and AOPs used in this study. Then we describe the bio-optical modeling used in our simulations. We also briefly present the variability our measurements of both absorption and scattering coefficients as well as reflectance as a function of wavelength from 400 nm to 750 nm for the Chesapeake Bay and Long Island Sound area during the 2005 and 2007 summer cruise campaigns respectively.

2.1 Theoretical Background

2.1.1 Absorption and scattering coefficient

Two of the fundamental IOP's are the absorption coefficient and the volume scattering function. Consider a small volume ΔV of water with thickness Δr, illuminated by a narrow collimated beam of monochromatic light with spectral radiant power $P_i(\lambda)$, W nm^{-1}, as schematically illustrated in Fig. 2.1. Some part of incident power is absorbed within the volume of water $P_a(\lambda)$; some part is scattered out of the beam at an angle θ, $P_s(\theta, \lambda)$; and the remaining light, $P_t(\lambda)$, propagates in the same direction as the insistent light and transmitted through the volume. The spectral absorption coefficient is defined as the fraction of incident power that has been absorbed per unit length:

$$a(\lambda) = \lim_{\Delta r \to 0} \frac{P_a(\lambda)}{P_i(\lambda)\Delta r} \qquad m^{-1} \tag{2.1}$$

The angular scattered power per unit length and unit solid angle when normalized to the incident power is defined as volume scattering coefficient $\beta(\theta;\lambda)$ $(m^{-1}sr^{-1})$ which is a function of the angle between the directions of incident and scattered light, θ (θ varies from 0 to π):

$$\beta(\theta;\lambda) = \lim_{\Delta r, \Delta\Omega \to 0} \frac{P_s(\theta;\lambda)}{P_i(\lambda)\Delta r \Delta\Omega} \qquad m^{-1}sr^{-1} \tag{2.2}$$

Integration of $\beta(\theta;\lambda)$ over the 4π space is the total fraction of incident power per unit distance that has been scattered, and is defined as the scattering coefficient b(λ):

$$b(\lambda) = \lim_{\Delta r \to 0} \frac{P_s(\theta;\lambda)}{P_i(\lambda)\Delta r} = \int_{4\pi} \beta(\theta;\lambda) d\Omega \qquad m^{-1} \tag{2.3}$$

The attenuation coefficient c(λ) is defined as:

$$c(\lambda) = a(\lambda) + b(\lambda) \qquad m^{-1} \tag{2.4}$$

which describes the fraction of incident power loss per unit distance, either absorbed or scattered.

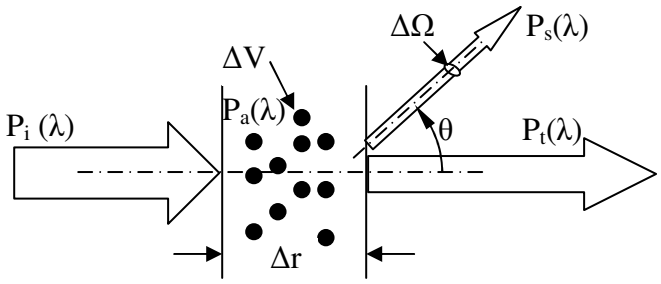

Fig. 2.1. Geometry used to define IOP's

If a water body contains several different substances which have scattering or absorption coefficient a_i, b_i for the i^{th} substances, then a or b of the whole water body is simply the addition of all of a_i or b_i:

$$a = \sum_i a_i \text{ and } b = \sum_i b_i \tag{2.5}$$

Similar approaches can be also applied to the attenuation coefficient c.

2.1.2 Reflectance

The spectral irradiance reflectance $R(z; \lambda)$ sr^{-1} and remote-sensing reflectance $R_{rs}(z; \theta_{sun}, \theta_{sensor}, \varphi_{azimuth}, \lambda)$ sr^{-1} are defined as fraction of the spectral upwelling irradiance $E_u(z; \lambda)$ ($\mu mol\ m^{-2}s^{-1}nm^{-1}$) or radiance $L_u(z; \theta_{sun}, \theta_{sensor}, \varphi_{azimuth}, \lambda)$ ($\mu mol\ m^{-2}s^{-1}nm^{-1}sr^{-1}$) respectively when normalized to the down welling plane irradiance $E_d(z; \lambda)$ ($\mu mol\ m^{-2}s^{-1}nm^{-1}$),

$$R(z;\lambda) = \frac{E_u(z;\lambda)}{E_d(z;\lambda)} \tag{2.6}$$

$$R_{rs}(z;\theta_{sun},\theta_{sensor},\phi_{azimuth},\lambda) = \frac{L_u(z;\theta_{sun},\theta_{sensor},\phi_{azimuth},\lambda)}{E_d(z;\lambda)} \quad sr^{-1} \tag{2.7}$$

where z is the depth measured from the sea surface, θ_{sun} the subsurface solar zenith angle, θ_{sensor} subsurface viewing angle from nadir, $\varphi_{azimuth}$ the viewing azimuth angle from the solar plane and λ the wavelength (nm). The remote sensing reflectance is most commonly associated with the IOP's in the water and is therefore of great significance, especially due to the fact that it can be estimated remotely from a space born sensor.

2.2 Optically significant water constituents and their bio-optical modeling

2.2.1 Optically significant constituents

The physical constituents in water can be divided into dissolved matter and particulate matter according to their sizes. A general diagram of their categorization is displayed in Figure 2.2.

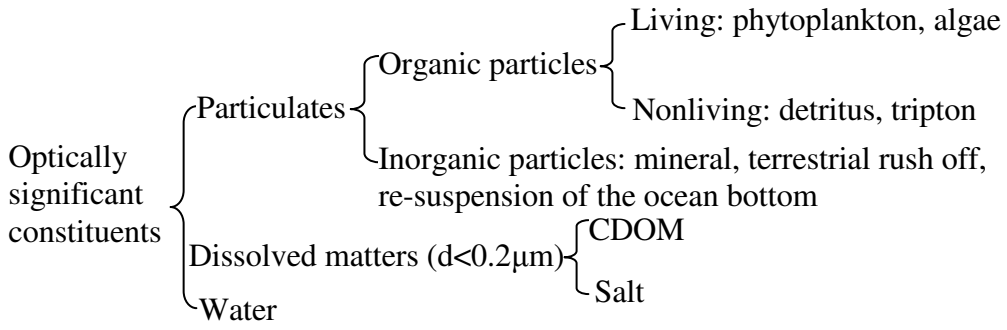

Fig. 2.2. Diagram of optically significant constituents

Particles with diameter less than 0.2μm are considered to be dissolved in water. For these particles, absorption is significant and scattering effects are negligible. Within this category, colored dissolved organic matters (CDOM) is one of the most commonly occurring substances in natural waters and results from the decomposition of vegetation and phytoplankton detritus. CDOM is also called yellow substance (gelbstoff) since it absorbs strongly in the blue region thus appears yellowish. One of the most important living organisms in the ocean is phytoplankton, wherein the major absorbing pigment is Chlorophyll-a. Phytoplankton has strong absorption bands in both the blue and red (i.e. 440 nm and 675 nm) with significantly reduced absorption in the

green region. In addition to the organic phytoplankton, nonliving organic particles (detritus or tripton) are a product of dead phytoplankton cells. Other particulates mainly clay minerals, can enter the ocean system through terrestrial rush off or from re-suspension of the ocean bottom.

2.2.2 Relationship between R_{rs} and IOP's

Remote-sensing reflectance, R_{rs} (see section 2.1.2), for optically deep waters is primarily controlled by the absorption and the scattering properties of the constituents in the water, and the sun/sensor geometries [*Lee et al.,* 1999],

$$R_{rs}\left(0^{+},\theta_{sun},\theta_{sensor},\phi_{azimuth},\lambda\right)=g\left[a(\lambda),\beta(\lambda),\theta_{sun},\theta_{sensor},\phi_{azimuth}\right]\ \ m^{-1} \tag{2.8}$$

where $a(\lambda)$ m^{-1} is the absorption coefficient, $\beta(\lambda)$ $m^{-1}sr^{-1}$ is the volume scattering function, θ_{sun} is the subsurface solar zenith angle, θ_{sensor} is the subsurface viewing angle from nadir, and $\varphi_{azimuth}$ is the viewing azimuth angle from the solar plane. To accurately model the function, g, we used Hydrolight5^{TM}, assuming both the sun and the sensor at nadir, which represents the MODIS R_{rs} product after atmospheric [*Gordon and Wang*, 1994] and bidirectional correction [*Morel et al.*, 2002].

Fortunately, the absorption and backscattering coefficient, a and b_b, as a function of wavelength, λ nm, can be separated into the contributions of each component,

$$a(\lambda)=a_w(\lambda)+a_{ph}(\lambda)+a_{dm}(\lambda)+a_g(\lambda)\ \ m^{-1} \tag{2.9}$$

$$b_b(\lambda)=b_{bw}(\lambda)+b_{ph}(\lambda)+b_{dm}(\lambda)\ \ m^{-1} \tag{2.10}$$

where the subscripts *w*, *ph*, *dm*, *g* stand for water, phytoplankton, detritus-mineral (the NAP) and gelbstoff (yellow matter or CDOM) components, respectively. The modeling for each component is described in the following sections.

2.2.3 Water contribution

The pure water absorption and scattering coefficient spectra, $a_w(\lambda)$ and $b_w(\lambda)$, where taken from *Pope and Fry* [1997] and *Morel* [1974] respectively. The backscattering coefficient, $b_{bw}(\lambda)$, is assumed to be half of $b_w(\lambda)$, due to the symmetry of its phase function. Both parameters, $a_w(\lambda)$ and $b_{bw}(\lambda)$, were furthermore corrected in this paper for average temperature and salinity as discussed in Hydrolight5^{TM}.

2.2.4 Algal component

To model the chlorophyll contribution to the total absorption, $a_{ph}(\lambda)$, we used a combination of micro- and pico-plankton weighted by the size parameter $\left(S_f\right)$ to initially model the specific absorption, $a_{ph}(\lambda)$ as follows:

$$a^*_{ph}(\lambda) = S_f \times a^*_{pico}(\lambda) + (1 - S_f) \times a^*_{micro}(\lambda) \quad m^2 \cdot mg^{-1} \tag{2.11}$$

with S_f uniformly distributed between 0 and 1 [*Ciotti et al.*, 2002]. The specific absorptions of micro- and pico- plankton are shown in Figure 2.3. Then we can analytically calculate $a_{ph}(\lambda)$ as

$$a_{ph}(\lambda) = a^*_{ph}(\lambda) \times \left[Chl\right]^P \quad m^{-1} \tag{2.12}$$

with the exponent P taken as 0.626 [*IOCCG Dataset*, 2003] for chlorophyll concentrations less than 1 mg/m^3, and 1 for [*Chl*] greater than 1 mg m^{-3}, which leads to

the statement that the relationship between [*Chl*] and $a_{ph}^{*}(\lambda)$ is linear for higher concentrations and depend on the species type.

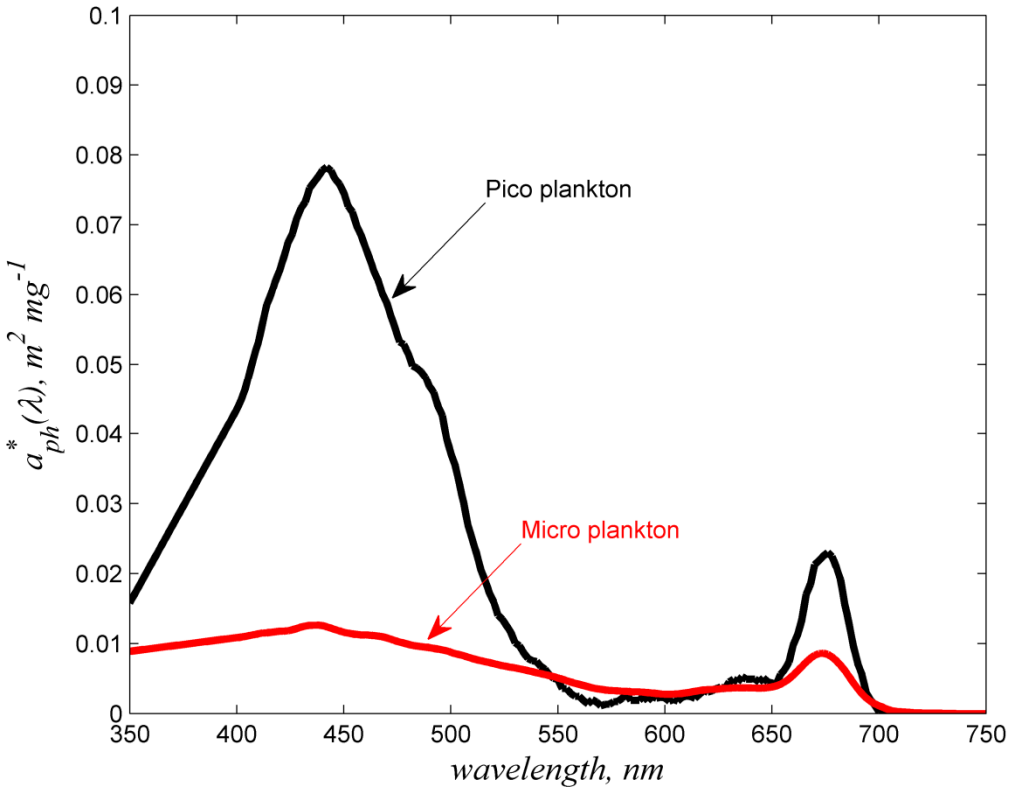

Fig. 2.3. The specific absorption of two phytoplankton species, the pico-plankton absorption (black) and the micro-plankton absorption (red). A combination of these two absorptions is used in the construction of the simulated dataset.

The scattering spectrum of algal cells based mainly on field observations can be modeled as the difference of their attenuation and the absorption spectra, as discussed in [*IOCCG Dataset,* 2003; *Bukata et al.*, 1995; *Stramski et al.*, 2001; *Gilerson et al.,* 2007], by

$$b_{ph}(\lambda) = c_{ph}(\lambda) - a_{ph}(\lambda) \quad m^{-1} \tag{2.13}$$

To model the attenuation spectrum of the algal cells, *c*, we used a commonly used power law function as in *IOCCG dataset* [2003] and *Gilerson et al.,* 2007,

$$c_{ph}(\lambda) = c_{ph}(550) \times \left(\frac{550}{\lambda} \right)^{Y_{ph}} \quad m^{-1} \tag{2.14}$$

where $c_{ph}(550)$ is modeled as

$$c_{ph}(550) = \rho \times [Chl]^{P} \quad m^{-1} \tag{2.15}$$

and ρ varies randomly between 0.1 and 0.4 m^2 mg^{-1}. *P* is the same as in Eq. 2.12 since algal cells are more effective scatterers in low absorbing, usually case 1 waters. For higher concentrations, usually case 2 waters, we assume that the relationship between the specific scattering of algal cells and [*Chl*] is linear.

The slope, Y_{ph}, is *0.1+1.6 Ψ+0.5/(1+[Chl])*; the last term is added as a trade off such that the slope of the algal cells attenuation appears consistently higher for lower [*Chl*] waters [*Carder et al.,* 1999]. Ψ is a uniformly distributed random variable between 0 and 1. Scattering can be transformed to the backward direction by assuming a constant backscattering ratio, $\tilde{b}_{ph}$ (dimensionless), such that:

$$b_{b-ph}(\lambda) = \tilde{b}_{ph} b_{ph}(\lambda) \quad m^{-1} \tag{2.16}$$

where $\tilde{b}_{ph}$= *0.006+0.005Ψ* ; and Ψ is a random variable between 0 and 1 [*Oishi et al.*, 2002].

2.2.5 Non-algal Particulates

In this study we assume that all the non-algal particles (detritus, mineral and others; NAP) behave similarly. The absorption of these particles was modeled as an exponential decaying function [*Babin et al.*, 2003a],

$$a_{dm}(\lambda) = a_{dm}(412) \times \exp[S_{dm} \times (412 - \lambda)] \quad m^{-1} \tag{2.17}$$

where the absorption of NAP at 412nm, $a_{dm}(412)$, is just the product of the specific absorption and the NAP concentration, [*NAP*] g m^{-3},

$$a_{dm}(412) = a^{*}_{dm}(412) \times [NAP] \quad m^{-1} \tag{2.18}$$

The specific absorption, $a^{*}_{dm}(412)$, and the slope of exponential decay function, S_{dm} for the NAP, are random values between 0.02 ~ 0.08 m^2 g^{-1} and 0.007 ~ 0.015 nm^{-1} respectively [*Babin et al.*, 2003a]. The minimum and maximum spectral variation of the NAP absorption is shown in Figure 2.4.

The scattering of these particulates was also modeled, like the attenuation of the algal particles, as a power law function [*Babin et al.*, 2003b]

$$b_{dm}(\lambda) = b_{dm}(550)\left(\frac{550}{\lambda}\right)^{Y_{dm}} \quad m^{-1} \tag{2.19}$$

and to convert it to the backward direction, we also assumed a constant backscattering ratio

$$b_{b-dm}(\lambda) = \tilde{b}_{dm} \times b_{dm}(\lambda) \quad m^{-1} \tag{2.20}$$

where $\tilde{b}_{dm}$= *0.01+0.01Ψ*, and Ψ is a random variable between 0 and 1, which covers the range for the coastal ocean and turbid harbor [*Mobley* ,1994]. The scattering of the non-algal particulate, $b_{dm}(550)$, was calculated as the product of the NAP specific scattering and [*NAP*] g m^{-3}, or,

$$b_{dm}(550) = b^{*}_{dm}(550) \times [NAP] \quad m^{-1} \tag{2.21}$$

where the specific scattering varies randomly between 0.2 and 1 m^2/g [*Babin et al.*, 2003b], and the slope, Y_{dm}=*0.5+1.5Ψ+0.2/(1+[NAP])*; where Ψ is also a random variable between 0 and 1.

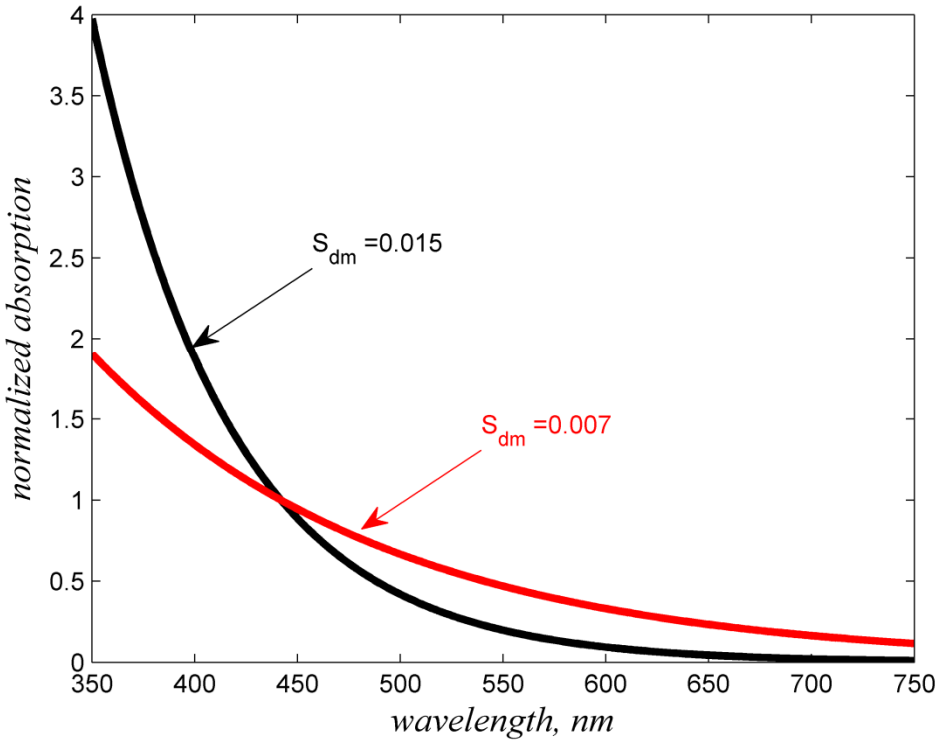

Fig. 2.4. The spectral variation of the NAP absorption coefficient with the minimum and maximum spectral slopes, S_{dm} (nm^{-1}). Both absorption spectra are normalized at 440 nm.

2.2.6 Colored dissolved organic matter

Colored dissolved organic matter, CDOM, often referred to as yellow substance or gelbstoff, includes all the dissolved substance as well as particles with a size of 0.2 μm or less, and thus doesn't contribute significantly to the scattering. Therefore in this study the scattering of CDOM is ignored.

The absorption of CDOM was also modeled as an exponential decaying function [*Carder et al.,* 1999; *Babin et al.*, 2003a; *Lee et al.,* 2002; *IOCCG Report 5,* 2006]

$$a_g(\lambda) = a_g(412) \times \exp[S_g \times (412 - \lambda)] \quad m^{-1} \tag{2.22}$$

where S_g=(0.01+0.01Ψ) (nm^{-1}); where Ψ is also a random variable between 0 and 1 [*Babin et al.*, 2003a]. The spectral range of the CDOM absorption is shown in Figure 2.5.

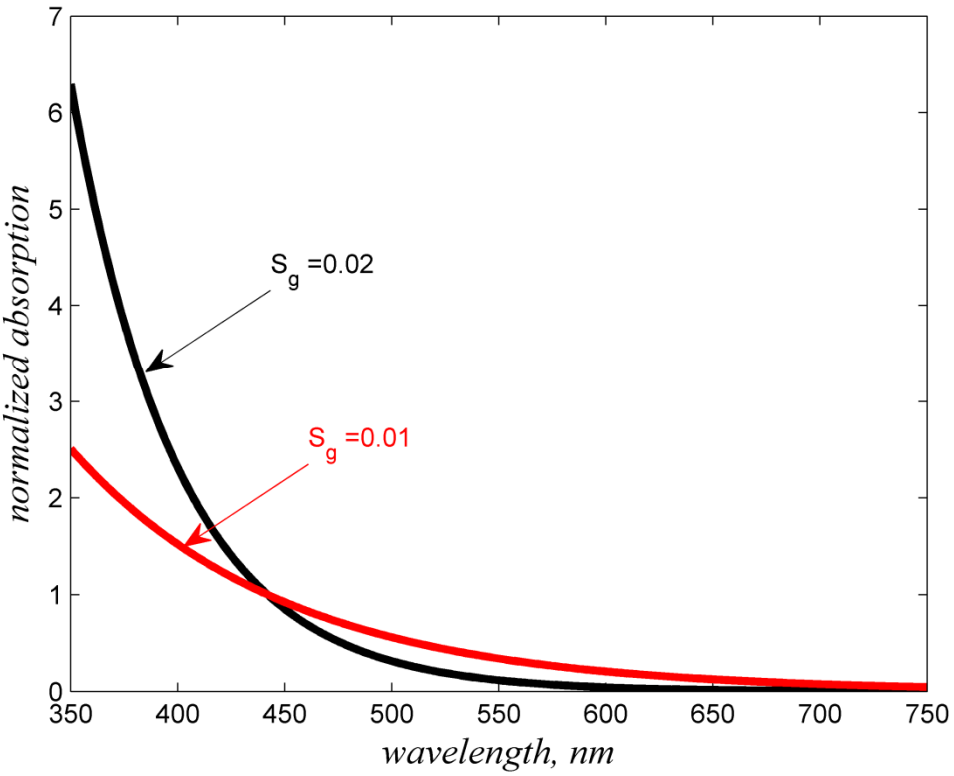

Fig. 2.5. The spectral variation of the CDOM absorption coefficient with the minimum and maximum spectral slopes, S_g (nm^{-1}). Both absorption spectra are normalized at 440 nm.

2.2.7 Accumulation of the Dataset

Assuming the models summarized in the previous section, we now generate a large enough dataset to train the NNs. To determine the range of each parameter, we used three (one for each parameter) exponential decaying functions with a common scaling variable χ ranging between 0.0005 and 4.5. The increment was chosen to be 0.0005 for a total of 9000 reflectances. With this common variable the distribution of each of the [*Chl*] (mg m^{-3}), [*NAP*] (g m^{-3}) and $\alpha_g(412)$] (m^{-1}) components can be obtained as,

$$[Chl] = 0.02 + 70 \times \exp(-\chi^{1.3}) \times \Psi_1 \quad mg\ m^{-3} \tag{2.23}$$

$$[NAP] = 0.02 + 50 \times \exp(-\chi^{1.4}) \times \Psi_2 \quad g\ m^{-3} \tag{2.24}$$

$$a_g(412) = 0.001 + 6 \times \exp(-\chi^{1.2}) \times \Psi_3 \quad m^{-1} \tag{2.25}$$

where $\Psi_{1,2,3}$ are uniformly distributed uncorrelated Random Variables between 0 and 1. In this way, all parameters vary independently of each other, allowing us to model different types of waters ranging from turbid coastal to clear open ocean waters. The distributions were obtained by describing each parameter in the NOMAD dataset as an exponential decay function with the same variable χ. The exponential function was chosen to equally represent clear Open Ocean, Coastal Ocean and Turbid coastal water types. The amplitudes of the exponential functions were set to the maximum value desired for each parameter, which are 70 mg m^{-3}, 50 g m^{-3} and 6 m^{-1} for [*Chl*], [*NAP*] and $a_g(412)$ respectively and are based on field observations. The power of the variable χ was empirically adjusted so that the NOMAD dataset absorption measurements fall within our simulations, Figure 2.6 and Figure 2.7, when we use the range of specific absorption for [*Chl*] mg m^{-3} and [*NAP*] g m^{-3} discussed in the modeling. The constant (0.02 mg m^{-3}) was added to the [*Chl*] mg m^{-3} as representing the lowest value that can be observed [*Morel et al.*, 2007]. The other parameters were adjusted in similar fashion. As we can observe in Figure 2.8, applying the tests described in IOCCG report 5 [2006] to our simulated dataset, the field measurements fall within our simulation values. In the next section we used these generated R_{rs} and the modeled IOP's to train both NN's.

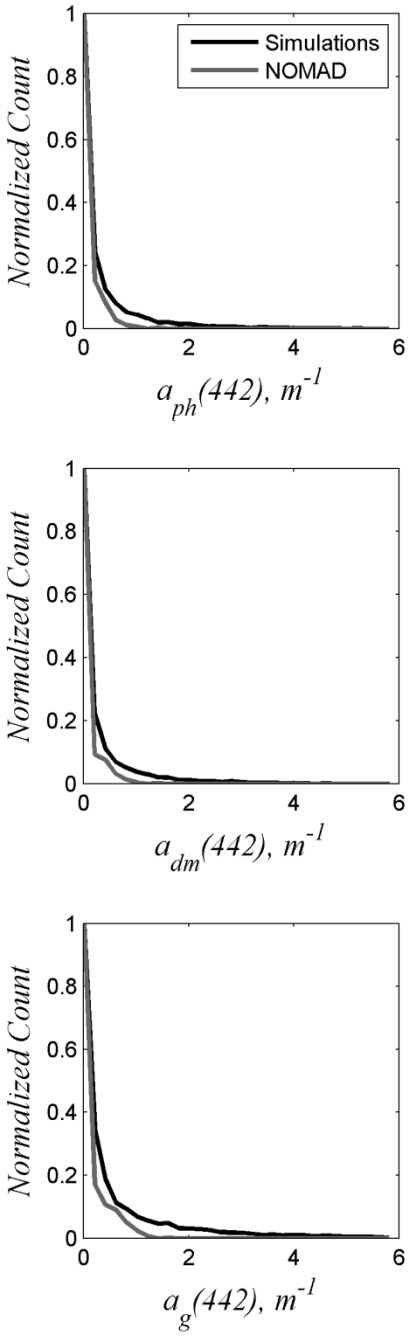

Fig. 2.6. Normalized distributions of the simulated dataset parameters (black line) and the NOMAD dataset (grey). Noticeably the measurements fall within the range of our simulations.

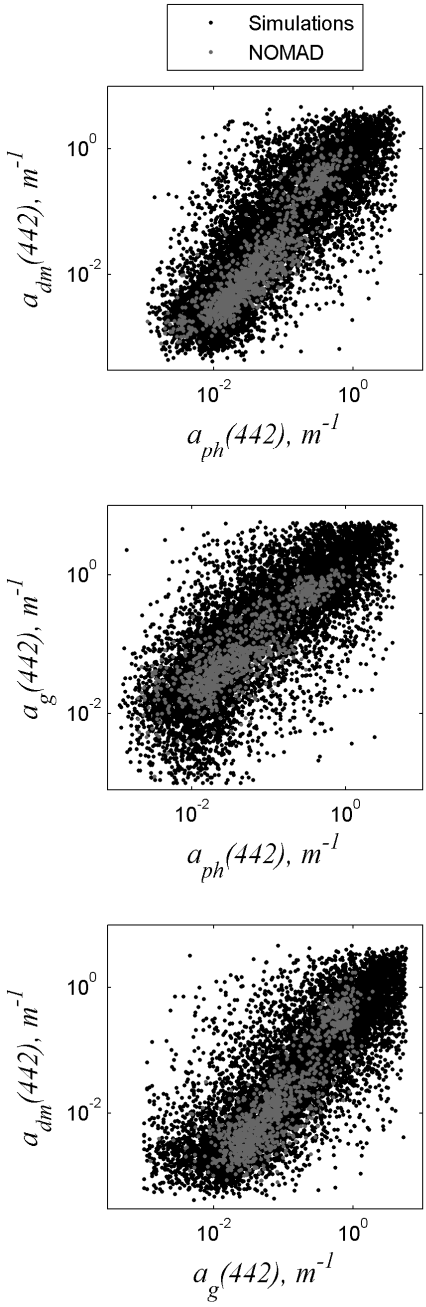

Fig. 2.7. Relationships of the three components at the reference wavelength used in the simulations according to the distribution functions used in our dataset. The black dots indicate the simulated datasets while the grey points indicate the measurements of the NOMAD dataset.

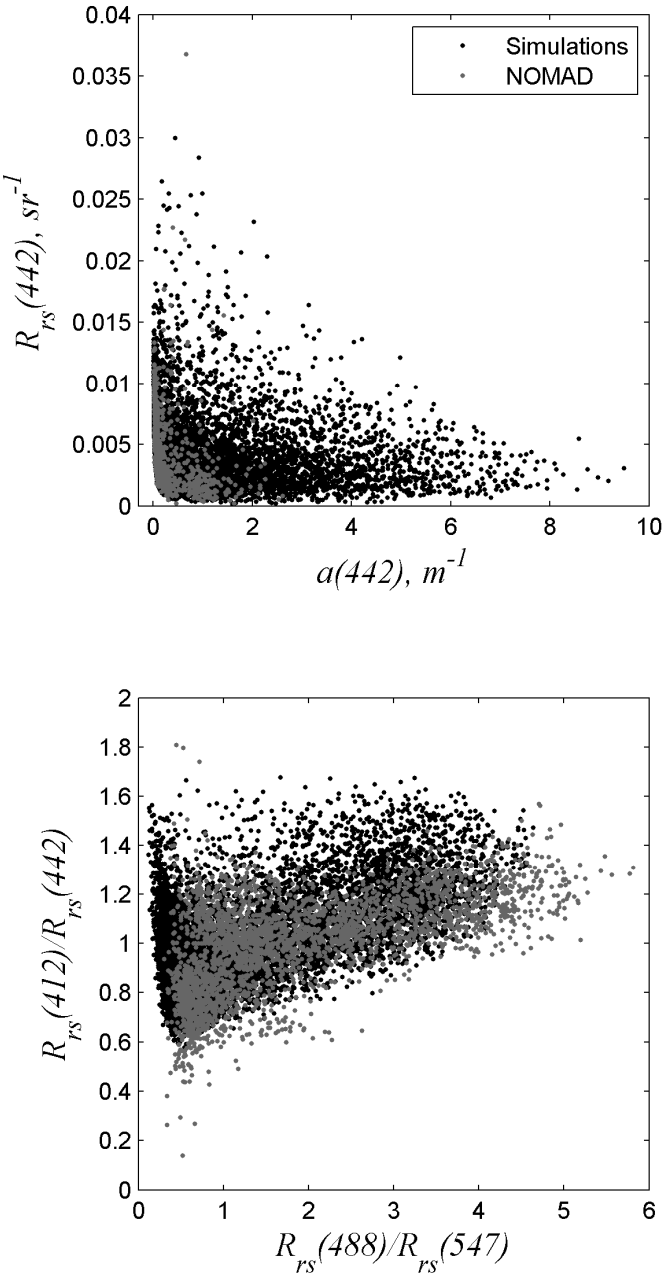

Fig. 2.8. Comparison between in situ and simulated dataset as indicated in IOCCG report 5 [2006]. The field data generally fall within our simulations.

2.3 Field measurements in Chesapeake Bay and Long Island

2.3.1 Optical instruments

In-situ measurements were conducted at 85 stations shown in Figure 2.9 in Chesapeake Bay area from July 11th to 20th 2005 and Long Island from June 25th to October 22th 2007 using a ship-deployed profiling package assembled by WET Labs (Philomath, Oregon).

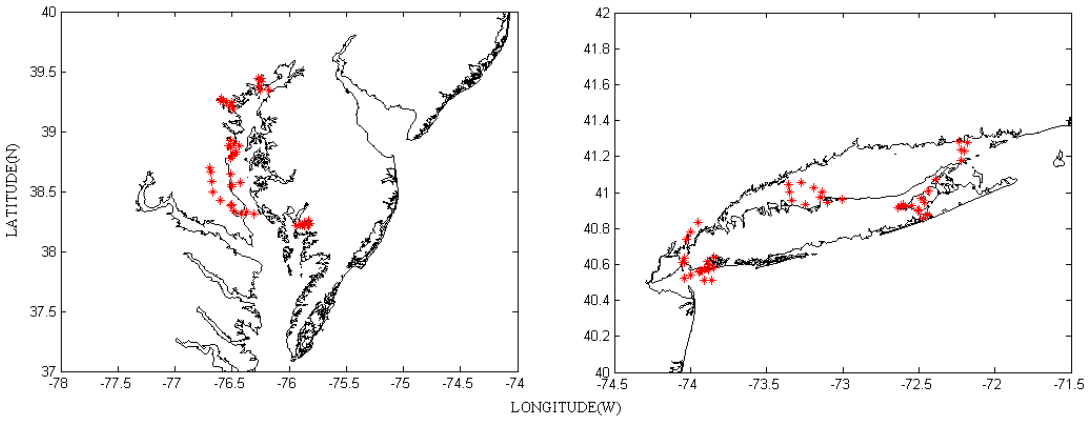

Fig. 2.9. Map of Chesapeake Bay (left) and Long Island (Right) representing the locations of the 85 stations sampled.

This package consists of three instruments: a hyperspectral absorption attenuation meter (AC-S), an Environmental Characterization Optics (ECO BB-9) scattering meter and a Conductivity, temperature and depth (CTD) meter. The AC-S has dual 25cm flow cells in which spectral absorption and attenuation are measured every 250ms at 82 wavelengths from 400nm to 750nm. To obtain accurate absorption measurements, the inner side of the tube is coated with quartz which can reflect the scattered light back into the chamber and finally collected by the detector. In order to

increase the field of view, the tube has a larger inner radius with large effective detection area. Internally the attenuation tube consists of a non-reflective material that absorbs most of the light hitting the wall and only allows the signal along the light path to reach the very narrow field of view detector. The water sample is pumped into the chambers through one of the intakes and a filter is installed at another intake to prevent large objects from entering and damaging the tubes. The ECO BB-9 scattering meter has 9 wavelength channels from 9 LEDs modulated at 1Hz to eliminate vibration noise. Seven channels measure the volume scattering at one nominal angle of 117˚ and the total backscattering coefficient is estimated assuming a constant proportionality between β (117˚) and b_b. The remaining two channels are for chlorophyll and CDOM measurement through fluorescence excitation. Conductivity, temperature and depth parameters were recorded every 1.25s with the CTD sensor (SBE37-SI) from SeaBird Inc. A data logger was used to power all the instruments, acquire data, coordinate different timing schemes and transmit the data to the computer. The depth of the profiler was raised and lowered either manually or by automatic winch in order to sample the depth profile of the ocean at a rate of about 0.5 m/s. The Wetlabs package was washed and the optical parts were cleaned with pure water at the end of each day.

The upwelling and downwelling radiance from the water was collected (simultaneously with the Wetlabs measurement) and delivered by fiber bundles to the spectroradiometers (GER). The fiber probe for upwelling measurements was placed just beneath the surface so that reflectance from the ocean surface can be obtained from normalizing the upwelling radiance to the down-welling radiance.

2.3.2 Variability of the measurements

The diversity of the measured spectral data of absorption and attenuation coefficients at the surface is shown in Figure 2.10 as well as the spectral reflectance just below the surface in Figure 2.11 for all stations. Cleary, the measured IOP and AOP data exhibits large variability in both regions. The absorption usually decreases exponentially with increasing wavelength as CDOM absorption is usually dominant in the blue region and the absorption exhibits a pronounced peak around 675nm due to phytoplankton absorption. The spectral dependence of the total water absorption changes from cases which CDOM is dominant with a minimal indication of phytoplankton absorption to cases where chlorophyll is the dominant mechanism. The value of $a(400)$ varies from less than 0.5 to 10 m^{-1} while the attenuation coefficients range from about 1 m^{-1} to more than 30 m^{-1}, indicating the high variability of non-algal particles. On the other hand, in some of the other stations, the large amount of inorganic particles raises the upwelling radiance signal greatly which masks the features in the NIR region.

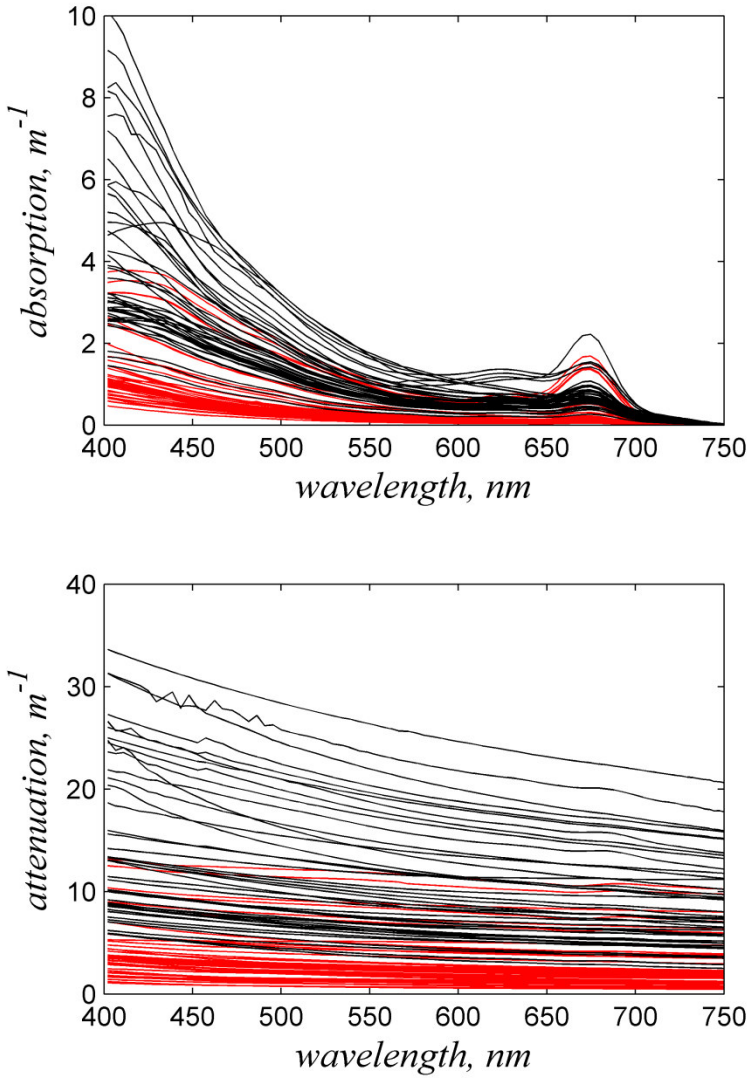

Fig. 2.10. Near surface measured absorption coefficient (upper) and attenuation coefficients (lower) as a function of wavelength for all the 85 stations. The Red lines represent the Long Island measurements while the Black lines represent the Chesapeake Bay Stations.

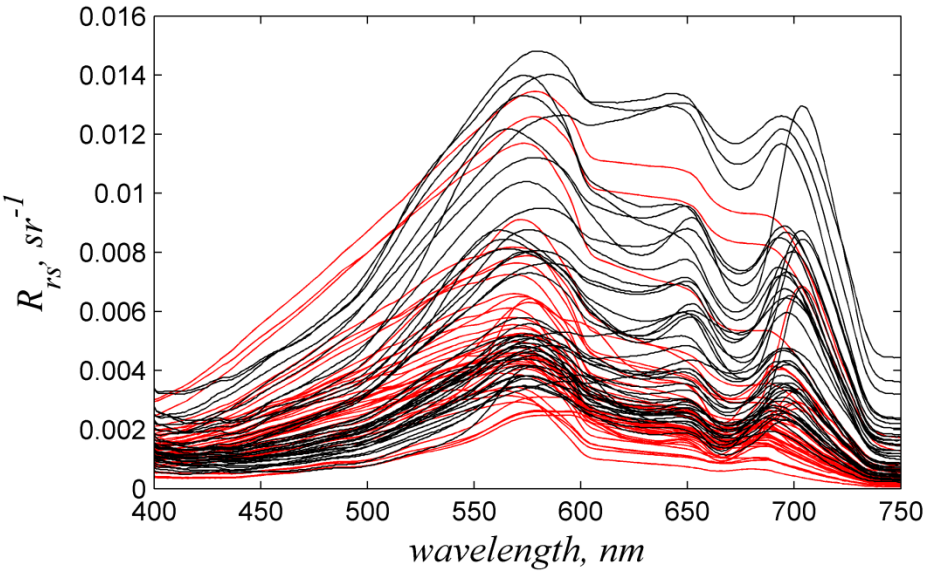

Fig. 2.11. Measured spectral reflectance just below the surface for all the 85 stations. The Red lines represent the Long Island Sound measurements while the Black lines represent the Chesapeake Bay Stations.

2.4 Summary

A comprehensive database of simulated data when combined with our in situ dataset of IOP and AOP from the Chesapeake Bay and Long Island regions is an excellent tool for the construction and validation of inversion algorithms. The Simulated dataset was generated using Hydrolight5^{TM} and the field dataset that was collected by *in-situ* optical measurements during the summer cruises of Chesapeake Bay and Long Island in 2005 and 2007 respectively. This includes the spectral absorption and attenuation coefficient at 82 wavelengths from 400nm to 750nm, volume scattering at 117˚ at 7 visible wavelength channels as well as CDOM and

chlorophyll concentration by excited fluorescence and spectral reflectance measurements.

Chapter 3 Inversion Techniques

3.1 Inverse Problems

If y^m represents the measurements (i.e R_{rs}), we can relate these to x, the physical variables (IOP's), through y, the physical forward model output (i.e. the radiative transfer function in the water), and ε, the measurement (or model) uncertainties (instrumental noise) as shown below in Eq. (3.1) [*Aires et al.*, 2001]:

$$y^m = y(x) + \varepsilon. \tag{3.1}$$

Both y and x are vectors representing multivariate observations and multi-parameter data. The inverse problem then consists in retrieving the physical variables x, given that measurement y^m. The solution of this problem consists of two main approaches.

In the first approach, called "localized" inversion [*Aires et al.*, 2001], an inverse process is used for each observation to find an estimate $\hat{x}$ of the physical variables x by minimizing the distance

$$D(y(\hat{x}), y^m). \tag{3.2}$$

The distance D (i.e Euclidean, relative difference) depends on the *a priori* information available for the variables involved. The over constrained linear matrix inversion algorithm [*Wang et al.*, 2005] falls within this category; therefore we will consider it as a "localized" algorithm in this study.

The second approach to this problem consists of estimating a transfer function G_W, with weighting parameters W, which is effectively a globally applicable model for y^{-1}. The parameters W are the results of the minimization of a cost function

$$\int D(\hat{x}, x) P(x, \varepsilon), \tag{3.3}$$

where $\hat{x} = G_W(y^m) = G_W(y(x) + \varepsilon)$, P is the probability distribution of the physical variables x and the noise ε. The Euclidian distance $D(\hat{x}, x)$ is integrated over the physical states and the noise, so that the transfer function is optimized globally over the range of both x and ε. In practice, to minimize the previous criterion of Eq. (3.3), a database is created, composed of a statistically representative sample of coincident variables x and measurements y^m and the estimation of the parameters, W, is made using this dataset. After this preliminary step for the estimation of G_W, the inversion of an observation is very fast since it involves only the direct use of G_W.

3.2 Established algorithms

3.2.1 Semi analytical linear matrix inversion

Semianalytical IOP inversion models [*Roesler and Perry*, 1995; *Hoge and Lyon*, 1996; *Wang et al.*, 2005] are based on three assumptions. The relation between r_{rs} and the absorption and backscattering coefficients is known. The absorption and backscattering coefficients for pure seawater are known. The spectral shapes of the absorption and backscattering coefficients for in-water constituents are known. These models often vary in their choice of the r_{rs} – IOPs relation, the assumed spectral shape of the component IOPs, the wavelength range used in the inversion, and the specifics of the mathematical method of inversion. In this study we compare our results with the results obtained by the over constrained linear matrix inversion algorithm as described [*Wang et al.*, 2005] and in [IOCCG report 5, 2006]. This is a localized algorithm as described in section 3.1.

3.2.2 Quasi Analytical Algorithm (QAA)

The Quasi-Analytical Algorithm (QAA) derives the absorption and backscattering coefficients by analytically inverting the spectral remote-sensing reflectance, $R_{rs}(\lambda)$ m^{-1}. QAA starts with the empirical calculation of the total absorption coefficient (a m^{-1}) at a reference wavelength (λ_0 nm), and then propagates the calculation to the other wavelengths. Component absorption coefficients (contributions by detritus/gelbstoff and phytoplankton pigments) are further algebraically decomposed from the total absorption spectrum. For a detailed explanation refer to [*Lee et al.*, 2002] and for the latest update that was used in this study in [*Lee et al.*, 2009]. This is a global retrieval algorithm as described in section 3.1.

3.3 Neural network Inversion scheme

3.3.1 Nonlinear model: the multilayer perceptron neural network

The multilayer perceptron neural network (MLP) is a nonlinear mapping model composed of parallel processors called "neurons." These processors are organized in distinct layers: The first layer, S_0, represents the input $Y = (y_i; i \in S_0)$ of the mapping. The last layer, S_L, represents the output mapping $X = (x_k; k \in S_L)$. The intermediate layers $S_m (0<m<L)$ are called the "hidden layers." These layers are connected via neural links (Figure 3.1). Any neurons, i and j, in two consecutive layers are connected with a synaptic weight $w_{i,j}$. Each neuron j executes two simple operations. First, it makes a weighted sum of all of its inputs z_i: this signal is called the activity of the neuron.

$$\alpha_j = \sum_{i \in Inputs(j)} w_{i,j} \cdot z_i \tag{3.4}$$

Then it transfers this signal to its output through a so called "activation function," often a sigmoid function; in this study we use the hyperbolic sigmoid transfer function $\sigma(\alpha) = 2/\left(1+e^{-2\alpha}\right) - 1$. The output z_j of the neuron j in the hidden layer is then given by

$$z_j = \sigma(\alpha_j) = \sigma\left(\sum_{i \in Inputs(j)} w_{i,j} \cdot z_i\right). \tag{3.5}$$

Usually for regression problems, the output units have no activation function. For example, in a one hidden-layer MLP, the k^{th} output x_k of the network is defined as

$$x_k(Y) = \sum_{j \in S_1} w_{j,k} \cdot \sigma(\alpha_j) = \sum_{j \in S_1} w_{j,k} \cdot \sigma\left(\sum_{i \in S_0} w_{i,j} \cdot y_i\right). \tag{3.6}$$

This Eq. is the only calculation necessary in the operational mode (once the synaptic weights have been determined by the training process). A bias term for each neuron has been deliberately omitted to simplify the notation, although it is used in the neural network. It has been demonstrated that any continuous function can be represented by a one-hidden-layer MLP with sigmoid functions, σ [*Horrnik et al.*, 1989; *Cybenko*, 1989; *Crone and Crosby*, 1995].

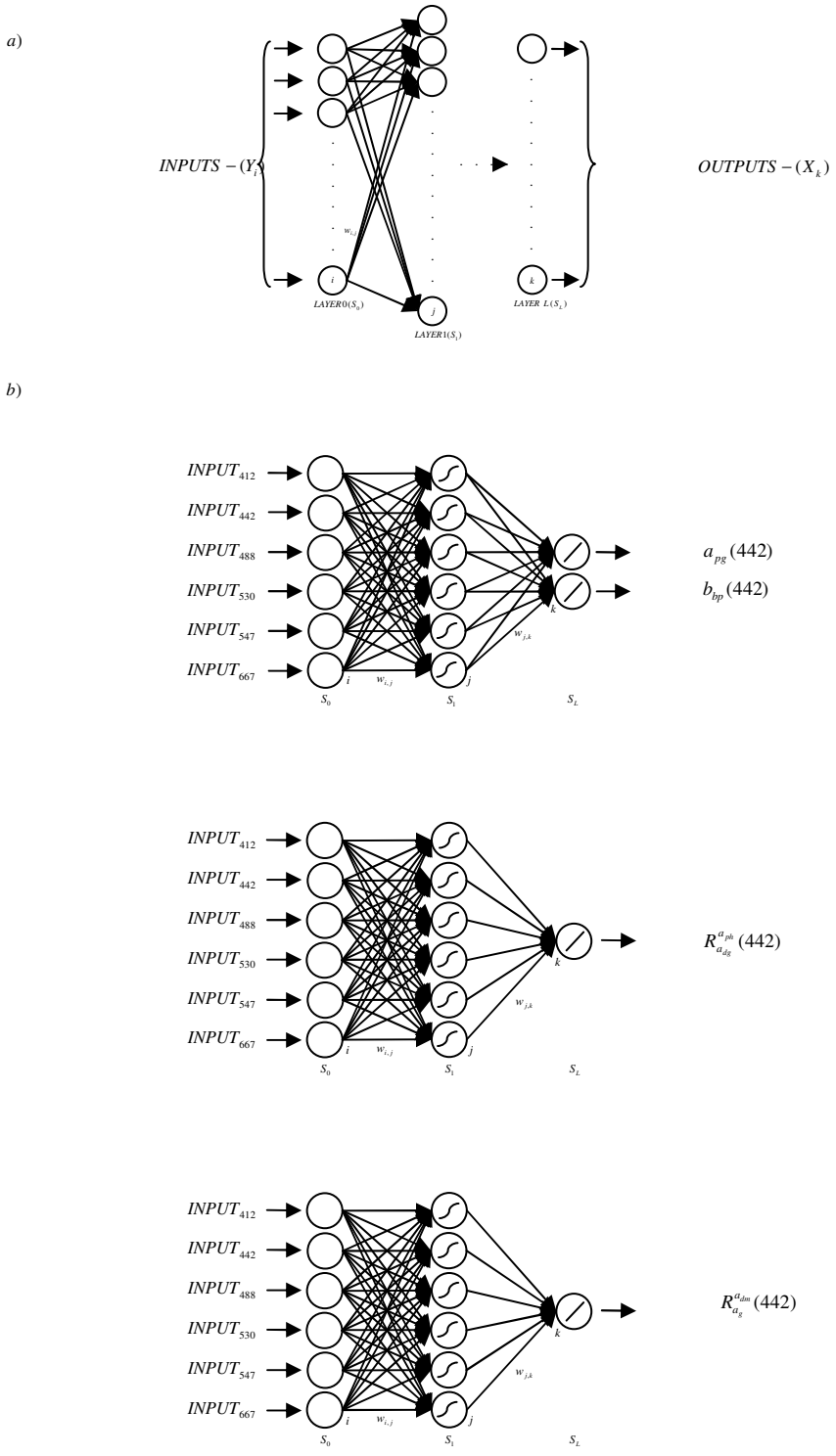

Fig. 3.1 General architecture of the MLP (a). Exact architecture of the three one layer MLPs that are used model the inverse problem of Ocean color for MODIS(b).

3.3.2 Optimization algorithm: Bayesian Regularization

Given the neural network architecture (activation functions, σ, number of layers, neurons), all the information of the network is enclosed in the set of all synaptic weights $W=\{w_{ij}\}$. The learning algorithm is an optimization technique that estimates the optimal network parameters W by minimizing a cost function $C(W)$, approaching as closely as possible the desired function. The criterion usually used to derive W (also adapted in the study) is the minimization of sum square error in network outputs

$$C(W) = \sum_{k \in S_2} \iint D_E(\hat{x}_k(Y;W), x_k)^2 \cdot P(Y, x_k) dx_k dY, \tag{3.7}$$

Where D_E is the Euclidian distance between x_k, the k^{th} desired output component, and $\hat{x}_k$, the k^{th} neural network output component, and S_2 is the output layer of the neural network. $P(Y,x_k)$ is the joint probability distribution function of Y and x_k. In practice, the probability distribution function $P(Y,x_k)$ is sampled in a dataset $B=\{(Y^\eta,x_k^\eta), \eta=1,..,N\}$ of N input/output couples, $C(W)$ is then approximated by the sum squares criterion:

$$\tilde{C}(W) = \sum_{\eta=1}^{N} \sum_{k \in S} D_E(\hat{x}_k(Y^\eta;W), x_k^\eta)^2. \tag{3.8}$$

The Levenberg-Marquardt optimization with Bayesian Regularization algorithm was used to minimize $C(W)$ [*Levenberg*, 1944; *Marquardt*, 1963; *MacKay*, 1992; *Foresee and Hagan*, 1997]. The algorithm *Foresee and Hagan* [1997], combines Levenberg-Marquardt, a combination of steepest descent and Gauss-Newton method, and regulates the network with the probabilistic approach of Bayes' rule in order to minimize the combination of squared errors and weights and determine the correct combination so as to create a network which generalizes well.

Bayesian Regularized neural networks are more robust than standard back-propagation nets and can reduce or eliminate the need of lengthy cross validation. They are hard to overtrain, as a verification procedure provides an objective criterion for ending the training and removes the need for a separate validation set to detect the onset of overtraining. They are also difficult to over-fit, because they calculate and train on the effective number of parameters (essentially the number of non-trivial weights in the trained neural network). This is considerably smaller than the number of weights in a standard fully connected back-propagation net. These more cost-conscious nets are much less likely to be over-fitted. Bayesian networks basically integrate Occam's razor [*MacKay*, 1992], routinely and optimally penalizing extremely complex models. In addition Bayesian nets are also insensitive to the architecture of the network as long as a minimal architecture has been provided [*Livingstone*, 2009].

3.3.3 Algorithm Description

As mentioned earlier, we choose to use three different NNs to model the inverse problem, since the retrieval of the bulk absorption and backscattering are level 1 products [*Lee et al.*, 2002] and their retrievals should be the most simple and accurate. The first neural network considered, is designed to generate two outputs: the particulate and dissolved absorption coefficients and particulate backscattering coefficients at 442nm from the appropriate R_{rs} spectral measurements. The second neural network considered, generates, from the same input, the ratio of algal to non-algal absorption at 442nm and the third the ratio of non-algal particulate to dissolved absorption at 442nm. Although the output of the later two networks should be seen as a less accurate estimate, since the available R_{rs} measurements are probably not enough

for this task, good retrievals are observed in both the simulated and the field data when we use the output of both networks to algebraically separate the particulate and dissolved absorption, $a_{pg}(442)$, into two independent algal and non-algal absorption components at this wavelength, a_{dg} and a_{ph}, where:

$$a_{pg}(442) = a_{dg}(442) + a_{ph}(442) \tag{3.9}$$

Knowing the ratio of $R_{a_{dg}}^{a_{ph}}(442)$, from the second network, we can solve for $a_{ph}(442)$ as follows,

$$a_{ph}(442) = \frac{a_{pg}(442)}{1 + \frac{1}{R_{a_{dg}}^{a_{ph}}(442)}} \tag{3.10}$$

Then $a_{dg}(442)$ is just the difference

$$a_{dg}(442) = a_{pg}(442) - a_{ph}(442) \tag{3.11}$$

Clearly, a_{ph} and a_{dg} are level 2 products [*Lee et al.*, 2002], and as such, retrievals of these parameters will give higher errors since they depend on the previous retrievals. In a similar manner if we know the ratio of $R_{a_g}^{a_{dm}}(442)$ (from the third network) we can decompose a_{dg} into the dissolved, a_g, and non-algal particulate, a_{dm}, absorption coefficient at this wavelength. These are clearly level three products as they depend on a_{dg}, a level 2 product. Refer to Figure 3.2 for and illustration of the algorithm and different levels of products.

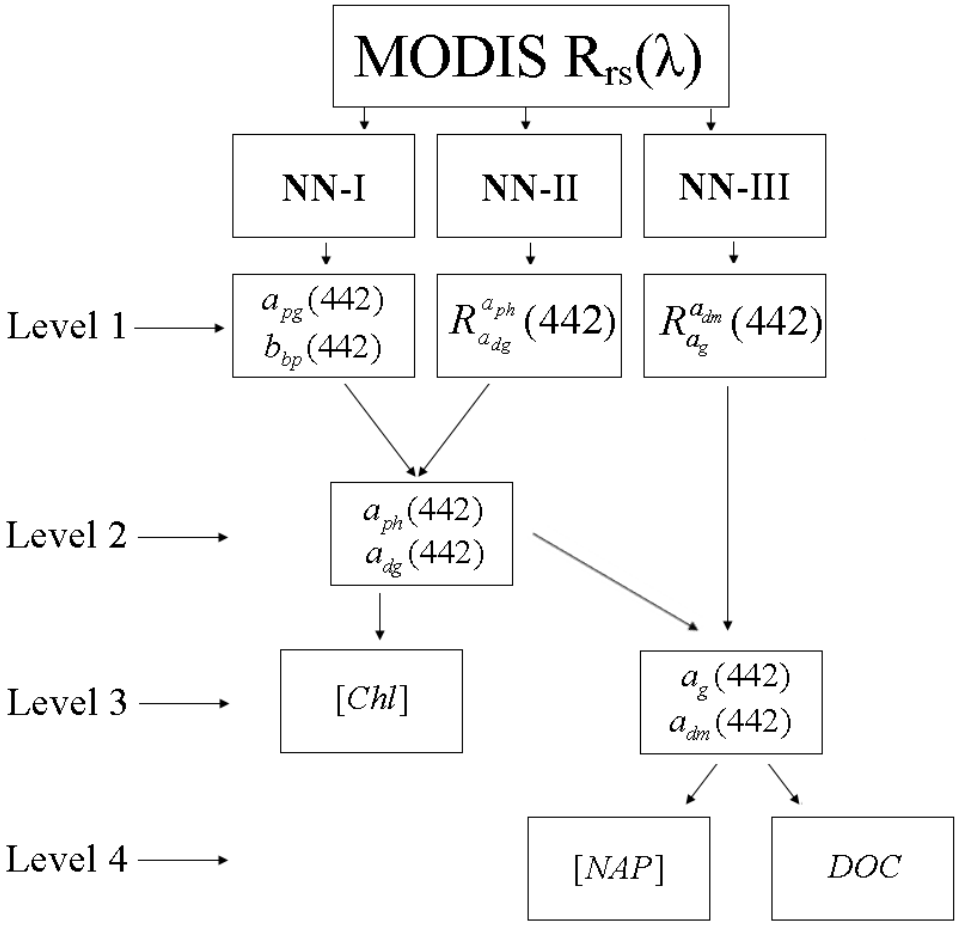

Fig. 3.2 Algorithm description and levels of products as explained in section 3.3.3.

3.3.4 Normalizing the Data

To make the NN equally sensitive to all inputs and avoid conditioning problems, the neural network inputs are normalized by removing the mean and scaling the variances before the training stage ($\log_{10}(R_{rs})$) at each wavelength; so the inputs of the NN are :

$$Input(i) = \frac{\log_{10}\left(R\mathrm{rs}(i)\right) - \mu_{input}(i)}{\sigma_{input}(i)} \tag{3.12}$$

where, i, is the index that represents the MODIS six visible channels from 411nm through the 667nm and the mean μ_{input} and the standard deviation σ_{input} at each R_{rs} (expressed as $\log_{10}$) were obtained from our simulated datasets. To simulate MODIS R_{rs}, the model based R_{rs} was first simulated at 1nm resolution, and thereafter convolved with the Spectral Response Functions (SRF's) of the MODIS Aqua sensor [*MODIS Aqua SRF*]. Normalization is also required for the outputs of the NN because of the activation function we used. The hyperbolic tangent sigmoid transfer function ($\sigma(\alpha) = 2/(1+e^{-2\alpha}) - 1$) we used in this study takes values between -1 and 1, therefore the outputs, after normalization, have to be further adjusted to fall within this range. To force the output data into the range of -1 and 1, we follow the constraints by dividing the outputs of the first network by 2σ, the second by 3σ and the third by 4σ. Thereafter the standard deviations are referred to as σ_o for all networks. Explicitly, the two output targets for the first network are,

$$output(1) = \frac{\log_{10}(a_{pg}) - \mu_o(1)}{\sigma_o(1)}, \tag{3.13}$$

$$output(2) = \frac{\log_{10}(b_{bp}) - \mu_o(2)}{\sigma_o(2)}, \tag{3.14}$$

for the second network,

$$output = \frac{\log_{10}\left(\frac{a_{ph}}{a_{dg}}\right) - \mu_o(3)}{\sigma_o(3)}. \tag{3.15}$$

and for the third

$$output = \frac{\log_{10}\left(\frac{a_{dm}}{a_g}\right) - \mu_o(4)}{\sigma_o(4)}. \qquad (3.16)$$

Of course, the outputs of all three neural networks have to be de-normalized with these mean and standard deviations.

3.3.5 Architecture

Since it has been demonstrated that any continuous function can be represented by one-hidden-layer multilayer perceptron, MLP, neural network with sigmoid functions [*Horrnik et al.*, 1989; *Cybenko*, 1989; *Crone and Crosby*, 1995] we used here one-hidden-layer with six neurons to train all three networks. We choose six neurons since we have six inputs. All networks were trained using a randomly selected 35% of the total data set. To make each network more robust and insensitive to noise, we choose to train the first network with 10% noise the second with 20% and the third with 30%. The increased noise imparted to the second and third networks was chosen since the NN did not perform well, on the field data, at lower noise levels (indicating that it was still sensitive to the noise) and only became very robust and consistent when 20% and 30% noise levels were added respectively to each network. Even so, no significant difference between 10% and 20% was observed when applied to the simulated data. When training the second and third networks, we also restricted the training data so that the algal absorption is at least 10% of the non-algal for the second and non-algal particulate absorption is at least 10% of the dissolved absorption and vice versa for the third network, ensuring that sufficient signal features will occur to permit inversion of these parameters. The final neural network coefficients for the

weights and biases for both networks, as well as a mathematical implementation of the algorithm, are given next.

3.3.6 Algorithm Implementation

The detailed implementation of the NN algorithm developed is presented in this section. The first step of the algorithm, as discussed in the training stage, requires that R_{rs} is normalized at different wavelengths, as shown in Eq. (3.12). The mean values μ_{input}, and standard deviations, σ_{input}, for each network are given in Tables 3.1-3.3.

Table 3.1. Mean and standard deviation of the inputs for the α_{pg} and $b_{b\text{-}p}$ network.

	$log\{R_{rs}^{412}\}$	$log\{R_{rs}^{443}\}$	$log\{R_{rs}^{488}\}$	$log\{R_{rs}^{531}\}$	$log\{R_{rs}^{547}\}$	$log\{R_{rs}^{667}\}$
μ_{input}	-2.4238	-2.4172	-2.3282	-2.3038	-2.3039	-3.0357
σ_{input}	0.3084	0.2777	0.2430	0.3577	0.4230	0.7375

Table 3.2. Mean and standard deviation of the inputs for the network $R_{a_{dg}}^{a_{ph}}(442)$.

	$log\{R_{rs}^{412}\}$	$log\{R_{rs}^{443}\}$	$log\{R_{rs}^{488}\}$	$log\{R_{rs}^{531}\}$	$log\{R_{rs}^{547}\}$	$log\{R_{rs}^{667}\}$
μ_{input}	-2.4137	-2.4150	-2.3308	-2.3081	-2.3113	-3.0601
σ_{input}	0.3072	0.2789	0.2447	0.3620	0.4289	0.7389

Table 3.3. Mean and standard deviation of the inputs for the network $R_{a_g}^{a_{dm}}(442)$.

	$log\{R_{rs}^{412}\}$	$log\{R_{rs}^{443}\}$	$log\{R_{rs}^{488}\}$	$log\{R_{rs}^{531}\}$	$log\{R_{rs}^{547}\}$	$log\{R_{rs}^{667}\}$
μ_{input}	-2.3962	-2.3877	-2.2942	-2.2587	-2.2549	-2.9647
σ_{input}	0.2964	0.2643	0.2377	0.3615	0.4287	0.7488

The second step requires the calculation of the activation function, $\sigma(\alpha)$, where

$$\sigma(\alpha)=\frac{2}{1+e^{-2\alpha}}-1 \tag{3.17}$$

where α is given by,

$$\alpha=\begin{bmatrix} 0.0263 & -0.0974 & 0.0732 & 0.1207 & 0.0559 & -0.1136 \\ 0.2866 & -0.3382 & 0.0898 & 0.4422 & 0.0188 & 1.0006 \\ -0.7189 & -0.0737 & 0.7047 & 0.6362 & 0.1679 & -1.9526 \\ 0.1271 & -0.3980 & 0.2976 & 0.3444 & 0.0955 & -1.1113 \\ 0.0797 & -0.1104 & 0.0283 & 0.2284 & 0.1133 & 0.7287 \\ 0.0070 & 0.1419 & -0.0126 & -0.1071 & -0.0784 & 0.0616 \end{bmatrix} \times Input + \begin{bmatrix} 0.0618 \\ 1.9081 \\ 1.6717 \\ 0.1662 \\ 1.9662 \\ -0.7745 \end{bmatrix} \tag{3.18}$$

for the first network(for a_{pg} and $b_{b\text{-}p}$) and

$$\alpha=\begin{bmatrix} 0.0625 & 0.1401 & -0.1135 & -0.204 & 0.0172 & -0.6069 \\ 1.1289 & -0.2884 & -0.2429 & -0.1419 & -0.4505 & -0.0433 \\ -0.4030 & -0.0423 & 0.155 & 0.0097 & 0.1402 & 0.8283 \\ 0.6160 & -0.3984 & -0.4717 & 0.2444 & 0.4624 & -0.1867 \\ -0.2288 & -0.1289 & 0.6219 & 0.2947 & 0.2731 & -1.0645 \\ -0.2884 & 0.3029 & -0.4365 & -0.1793 & -0.2644 & 1.0189 \end{bmatrix} \times Input + \begin{bmatrix} -0.9316 \\ 0.2837 \\ 0.3768 \\ -0.5398 \\ -1.0015 \\ 0.5281 \end{bmatrix} \tag{3.19}$$

for the second network($R_{a_{dg}}^{a_{ph}}(442)$)and

$$\alpha=\begin{bmatrix} 0.2522 & -0.2023 & 0.0510 & 0.2885 & 0.1762 & 0.1864 \\ 0.4118 & 0.1002 & 0.0425 & -0.2135 & -0.1297 & -0.0387 \\ -0.1259 & -0.2329 & 0.0017 & 0.1671 & 0.2915 & 0.2001 \\ 0.6045 & -0.0403 & -0.1092 & 0.1775 & 0.0286 & -0.0348 \\ -0.2722 & 0.4400 & 0.1622 & -0.0280 & -0.2323 & -0.1399 \\ 0.5758 & -0.5293 & -0.1517 & 0.3812 & 0.1730 & -0.2172 \end{bmatrix} \times Input + \begin{bmatrix} 0.3828 \\ -0.2366 \\ -0.2431 \\ -0.5902 \\ 0.2255 \\ 0.2533 \end{bmatrix} \tag{3.20}$$

for the third network for $R_{a_g}^{a_{dm}}(442)$.

The outputs of the networks are then given by,

$$y_1 = \begin{bmatrix} 0.2411 & -0.1989 & -0.2459 & -0.4511 & 0.2136 & -2.4228 \\ 1.3594 & -0.6151 & -0.2335 & -0.4726 & 1.9273 & 0.0266 \end{bmatrix} \times \sigma(\alpha) + \begin{bmatrix} -1.3425 \\ -1.0179 \end{bmatrix} \quad (3.21)$$

for the first network (for a_{pg} and $b_{b\text{-}p}$), and

$$y_2 = \begin{bmatrix} -0.5533 & -0.3642 & -0.6332 & 0.9063 & -0.8372 & -0.7898 \end{bmatrix} \times \sigma(\alpha) + \begin{bmatrix} -0.3642 \end{bmatrix} \quad (3.22)$$

for the second (for $R_{a_{dg}}^{a_{ph}}(442)$) and

$$y_3 = \begin{bmatrix} 0.4523 & -0.2622 & -0.4753 & 0.5005 & -0.4000 & -0.4002 \end{bmatrix} \times \sigma(\alpha) + \begin{bmatrix} 0.1568 \end{bmatrix} \quad (3.23)$$

for the third (for $R_{a_g}^{a_{dm}}(442)$).

In the final step we de-normalize the neural network output(s) producing meaningful results of $a_{pg}(442)$, $b_{b\text{-}p}(442)$, $R_{a_{dg}}^{a_{ph}}(442)$ and $R_{a_g}^{a_{dm}}(442)$. Analytically,

$$\left\{ \begin{array}{l} a_{pg}(442) = 10^{\{\sigma_O(1) \times y_1(1) - \mu_O(1)\}} \\ b_{bp}(442) = 10^{\{\sigma_O(2) \times y_1(2) - \mu_O(2)\}} \end{array} \right\} \quad (3.24)$$

for the first network,

$$R_{a_{dg}}^{a_{ph}}(442) = 10^{\{\sigma_O(3) \times y_2 - \mu_O(3)\}} \quad (3.25)$$

for the second network, and

$$R_{a_g}^{a_{dm}}(442) = 10^{\{\sigma_O(4) \times y_2 - \mu_O(4)\}} \quad (3.26)$$

for the third. The means, μ_o, and standard deviations, σ_o, for each parameter are given in Table 3.4. We recommend that the values in the parenthesis, in Table 3.4, for $R_{a_{dg}}^{a_{ph}}(442)$ (the product of the fitting to the field data; discussed in detail in Chapter 4 section 4.1.2) should be used when applying the algorithm to field and satellite data. The Matlab program for the NN inversion algorithm described in this paper can be downloaded from the algorithm section of the Optical Remote Sensing Laboratory website (http://sky.ccny.cuny.edu/cw/algorithms2.php).

Table 3.4. Mean and standard deviation of the outputs in the simulated dataset. The values in the parenthesis are the product of the fitting to the field data (refer to section 4.1.2).

	$log_{10}\{\alpha_{pg}(442)\}$	$log_{10}\{b_{b\text{-}p}(442)\}$	$log_{10}\{ R_{a_{dg}}^{a_{ph}}(442) \}$	$log_{10}\{ R_{a_g}^{a_{dm}}(442) \}$
μ_o	-0.6209	-1.8505	-0.2205(0.1441)	-0.3418
σ_o	1.6355	1.8108	1.1600(1.5206)	1.6993

3.4 Summary

In this chapter we summarized two methods of inversion, a "localized" inversion algorithm *Wang et al.* [2005] and a "Global" *Lee et al.* [2002] and introduced our neural network based algorithm, also a "Global" algorithm. In the "localized" algorithm the inversion takes place on a pixel by pixel basis minimizing the error between the theoretical solution and the measurement. This process main disadvantage is that is long and cannot be applied to satellite measurements in large scales. The

second approach, “Global” inversion, consists of a transfer function that is effectively a globally applicable model for the inverse of the theoretical forward model. This method is very fast and relatively insensitive to reasonable noise, therefore excellent for large datasets inversion such as satellite images.

The neural network algorithm introduced here inverts in steps the multispectral remote sensing reflectance, R_{rs}, and estimates four water components. These include the algal, dissolved and non-algal particulate absorption coefficients and the particulate backscattering coefficient at 442nm. The separation of the non-algal absorption coefficient into its independent components of dissolved and non-algal particulate, introduced in this chapter, generates two new products and to our knowledge there is no other algorithm that can isolate these absorption coefficients. The validation of the neural network algorithm, on the simulated and field data, as well as the comparison with current algorithms both “localized,” SAA, and “Global,” QAA, are discussed in the next chapter.

Chapter 4 Application of the IOP Inversion Algorithms

In this chapter we validate the neural network algorithm on the part of the simulated data that was not used in the training stage and on field measurements. Then we compare the neural network retrievals with the available retrievals of the QAA and SAA on the NOMAD dataset and satellite imagery.

4.1 Validating the neural network

4.1.1 Simulated Data

We first test the NN on noiseless testing data after eliminating all the points used in the training phase of both networks. This leaves a total of 3965 total points for testing, of which 3686 points, have an algal absorption equal to at least 10% of the non-algal absorption components at 442nm as discussed Chapter 3 (section 3.3.5). For the third network we have a total of 2439 total points for testing, of which 1962 points where the non-algal particulate absorption is at least 10% of the dissolved absorption at 442nm and vice versa (also see section 3.3.5). The retrieval performance of the NN's for the simulated dataset with different noise levels are shown in detail in Tables 4.1 – 4.5 and Figures 4.1 – 4.3 below. Biasing the noise to positive and negative values mostly effects the backscattering retrieval as it heavily depends on the reflectance intensity. The retrieval of the absorption values is also effected but in a less significant way. This effect is not further presented or discussed in this study.

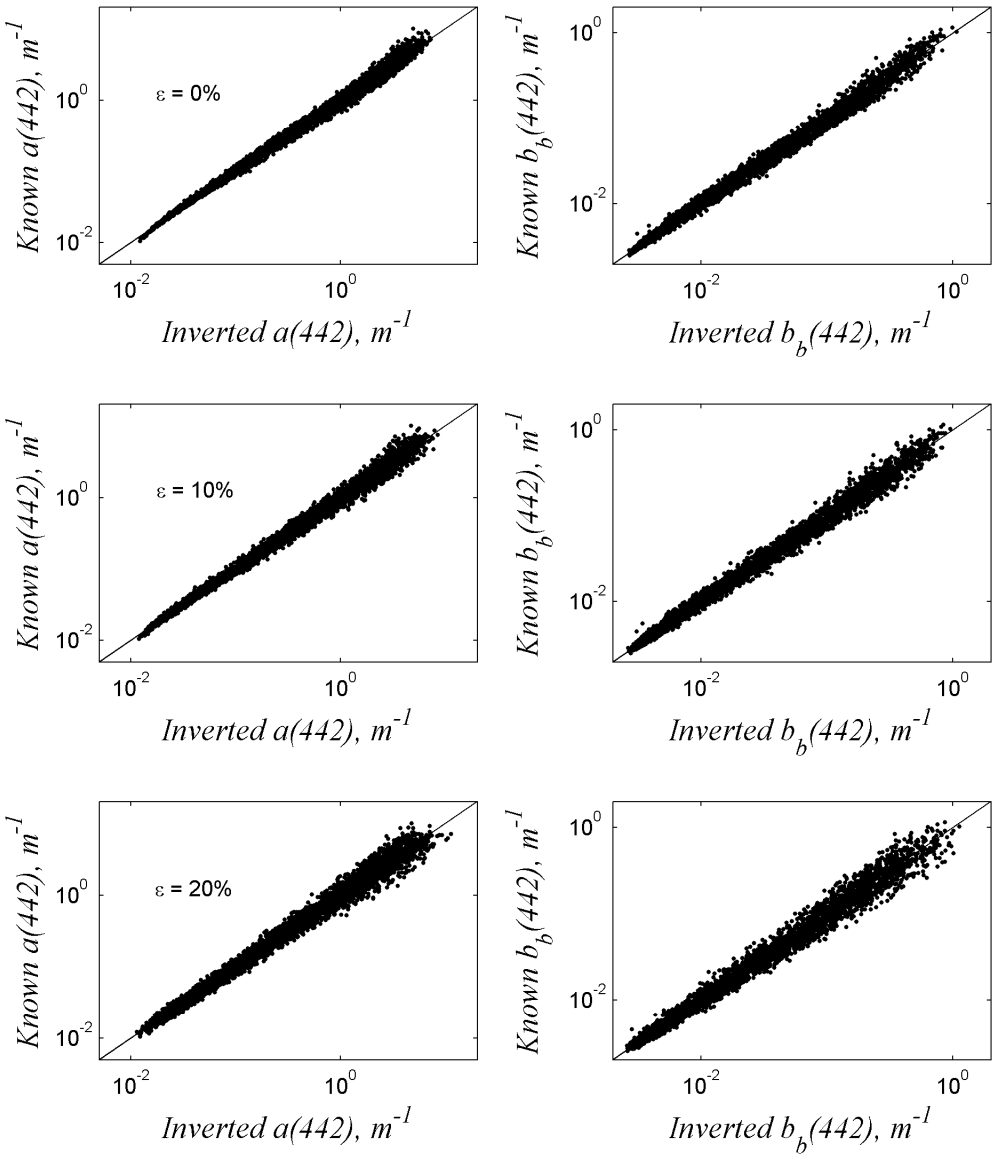

Fig. 4.1. Performance of the neural network on the part of our simulated dataset that was not used in the training stage. Inverted $a(442)$ m^{-1} (left columns) and $b_b(442)$ m^{-1} (right) (x-axis) plotted against the "known" values from our simulated dataset. Noise levels, ε, up to 20% (the top row is ε=0%) were added at each R_{rs}. The corresponding statistics are shown in Tables 4.1 – 4.3 below.

The total absorption coefficient and backscattering coefficient at 442 nm are retrieved with R^2 of 99.46% and 99.32% respectively, a root mean square error ($\log_{10}$ domain), $\mathrm{RSME}_{\log 10}$, of 0.0556 and 0.0583, and an error, e, of 0.1367 and 0.1438 where,

$$RMSE_{log10} = \left\{ \frac{1}{N} \sum_{i=1}^{N} \left[\log_{10}\left(\hat{x}_i\right) - \log_{10}\left(x_i\right) \right]^2 \right\}^{\frac{1}{2}} \tag{4.1}$$

and the linear percentage error, e, is

$$e = 10^{RMSE_{\log 10}} - 1. \tag{4.2}$$

The output of the second network, with the use of the retrieved particulate and dissolved absorption from the first, retrieves the algal absorption and non-algal absorption with R^2 of 92.74% and 98.5%, a $\mathrm{RSME}_{\log 10}$ of 0.2267 and 0.1068, and an e of 0.6854 and 0.2788 respectively. As discussed earlier, when we limit the data so that the algal absorption is at least 10% of the non-algal absorption, the statistics improve significantly. As seen in Tables 4.1 – 4.3 and Figures 4.1 and 4.2, when 10 and 20% noise was introduced to the R_{rs}, the retrievals are a little degraded as expected, but still very good, indicating that the neural network is insensitive to reasonable noise levels. The non-algal particulate and the dissolved absorption coefficient are also retrieved satisfactorily, as can be seen in Fig 4.3 and Tables 4.4 and 4.5. These retrievals seem less sensitive to noise and this is primarily attributable to the non-algal absorption being less sensitive to noise, as can be seen in Figure 4.2.

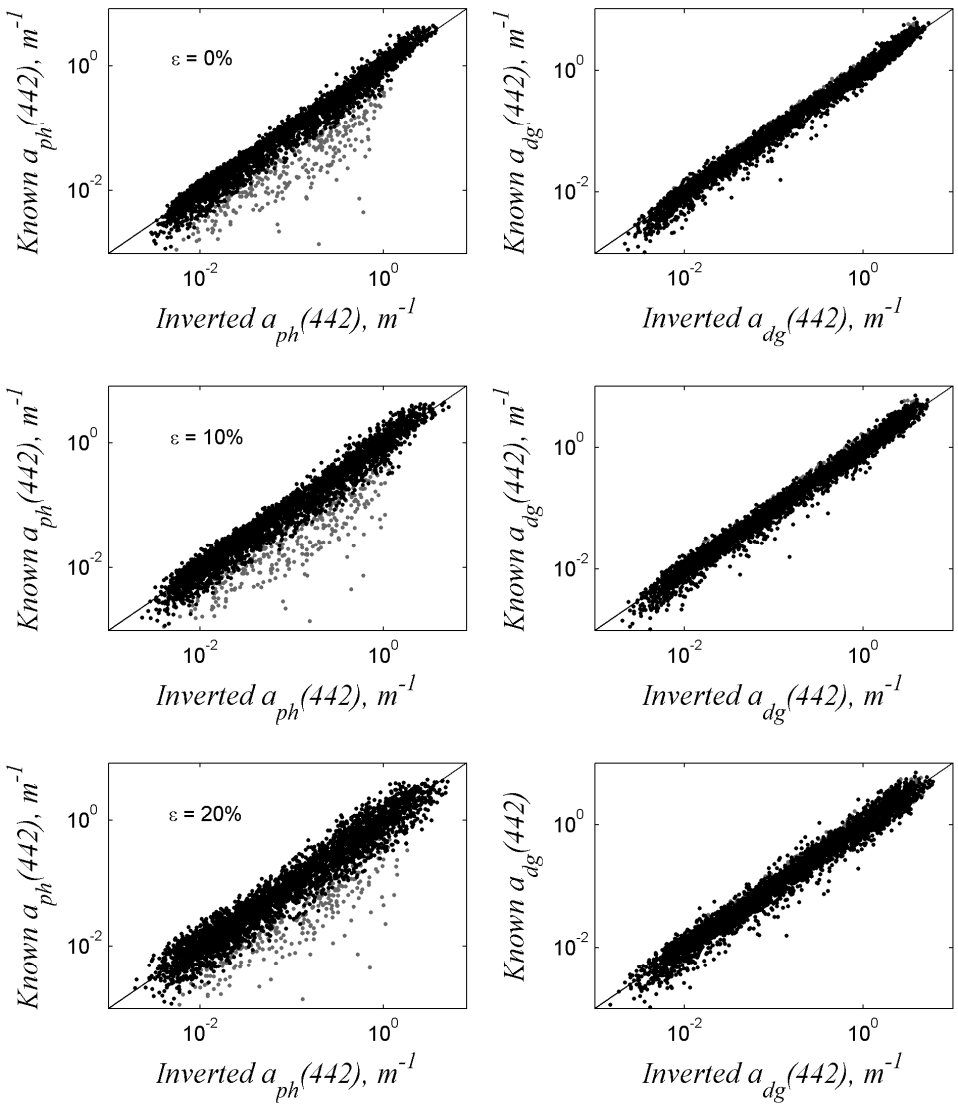

Fig. 4.2. Performance of the neural network on the part of our simulated dataset that was not used in the training stage. Inverted $a_{ph}(442)$ m^{-1} (left columns) and $a_{dg}(442)$ m^{-1} (right) (x-axis) plotted against the "known" values for these parameters from our simulated dataset. Noise levels, ε, up to 20% (the top row is ε=0%) were added at each R_{rs}. The grey dots indicate the cases where $a_{ph}(442)$ is less than 10% of $a_{dg}(442)$. The corresponding statistics are shown in Tables 4.1 - 4.3 below.

Table 4.1. Statistics of comparison for Figures 4.1 and 4.2 without noise. The values in the parenthesis indicate the results when $a_{ph}(442)$ is at least 10% of $a_{dg}(442)$.

	α (442)	b_b (442)	α_{ph} (442)	α_{dg} (442)
R^2	0.9946	0.9932	0.9274(0.9730)	0.9850(0.9851)
slope	1.0001	0.9973	1.0109(1.0240)	1.0172(1.0149)
intercept	0.0013	-0.0037	-0.1322(0.0005)	0.0079(-0.011)
$RMSE_{log10}$	0.0556	0.0583	0.2267(0.1359)	0.1068(0.1070)
e	0.1367	0.1438	0.6854(0.3676)	0.2788(0.2794)
N	3965	3965	3965(3686)	3965(3686)

Table 4.2. Statistics of comparison for Figures 4.1 and 4.2 when 10% noise is added at each R_{rs}. The values in the parenthesis indicate the results when $a_{ph}(442)$ is at least 10% of $a_{dg}(442)$

	α (442)	b_b (442)	α_{ph} (442)	α_{dg} (442)
R^2	0.9923	0.9913	0.9188(0.9645)	0.9823(0.9824)
slope	0.9994	0.9967	1.0038(1.0171)	1.0153(1.0129)
intercept	0.0005	-0.0043	-0.1473(-0.0144)	0.0061(-0.013)
$RMSE_{log10}$	0.0665	0.0662	0.2382(0.1543)	0.1155(0.1158)
e	0.1656	0.1647	0.7304(0.4266)	0.3046(0.3055)
N	3965	3965	3965(3686)	3965(3686)

Table 4.3. Statistics of comparison for Figures 4.1 and 4.2 when 20% noise is added at each $R_{rs.}$ The values in the parenthesis indicate the results when $a_{ph}(442)$ is at least 10% of $a_{dg}(442)$

	α (442)	b_b (442)	α_{ph} (442)	α_{dg} (442)
R^2	0.9863	0.9866	0.8956(0.9428)	0.9750(0.9751)
slope	0.9963	0.9940	0.9813(0.9966)	1.0098(1.0076)
intercept	-0.0036	-0.0098	-0.1986(-0.0591)	-0.0011(-0.02)
$RMSE_{log10}$	0.0886	0.0823	0.2675(0.1937)	0.1363(0.1366)
e	0.2264	0.2086	0.8515(0.5620)	0.3687(0.3698)
N	3965	3965	3965(3686)	3965(3686)

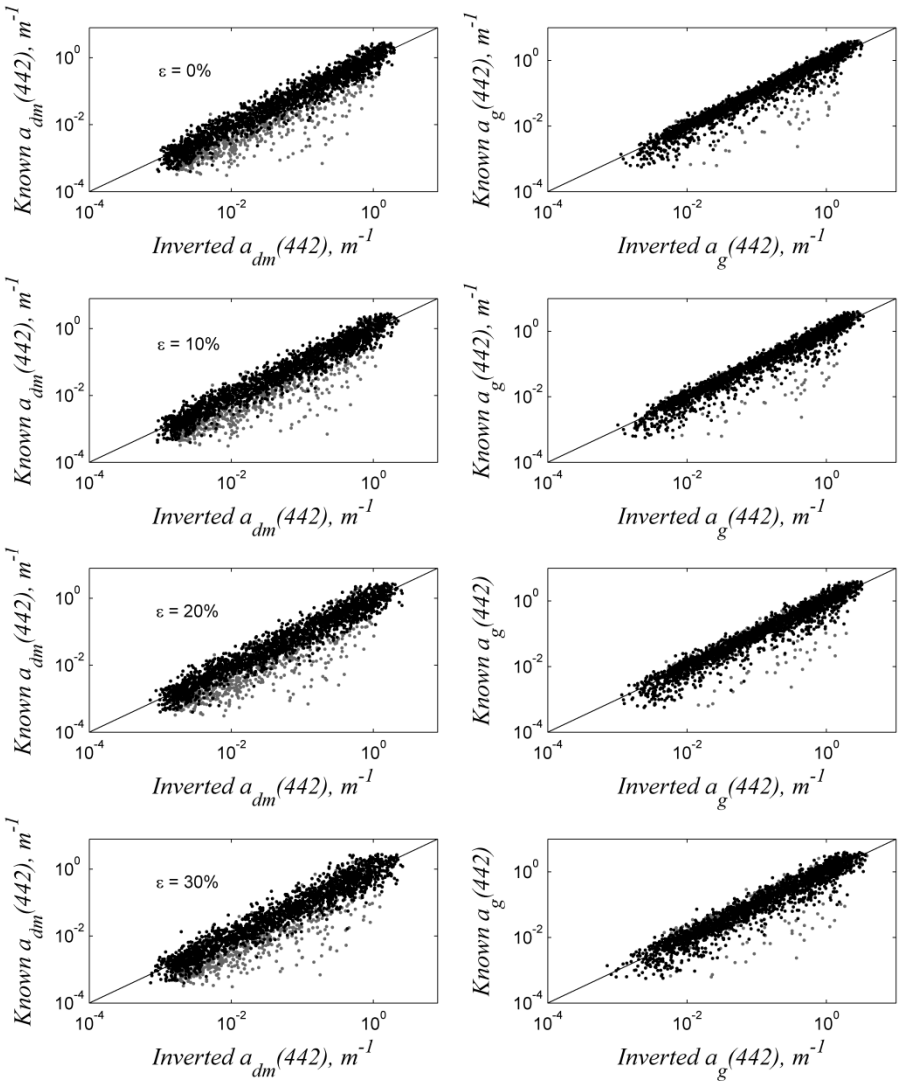

Fig. 4.3. Performance of the neural network on the part of our simulated dataset that was not used in the training stage. Inverted $a_{dm}(442)$ m^{-1} (left columns) and $a_g(442)$ m^{-1} (right) (x-axis) plotted against the "known" values for these parameters from our simulated dataset. Noise levels, ε, up to 30% (the top row is ε=0%) were added at each R_{rs}. The grey dots indicate the cases where $a_{dm}(442)$ is less than 10% of $a_g(442)$ and vice versa. See Table 4.4 and 4.5 for the corresponding statistics.

Table 4.4. Statistics of comparison for Figure 4.3 for $a_{dm}(442)$. The values in the parenthesis indicate the results when $a_{dm}(442)$ is at least 10% of $a_g(442)$ and vice versa. The noise, ε that was added to the reflectance, is indicated in the first column.

ε	0%	10%	20%	30%
R^2	0.8902 (0.9472)	0.8881(0.9454)	0.8821(0.9399)	0.872(0.93)
slope	1.0346(1.0134)	1.0340(1.0131)	1.0317(1.0108)	1.0147(1)
intercept	-0.2327(-0.0685)	-0.2299(-0.0637)	-0.2378(-0.0704)	-0.29(-0.12)
$RMSE_{log10}$	0.3668(0.2302)	0.3689(0.2335)	0.3770(0.2442)	0.389(0.26)
e	1.3269(0.6991)	1.3381(0.7120)	1.3820(0.7553)	1.45(0.83)
N	2439(1962)	2439(1962)	2439(1962)	2439(1962)

Table 4.5. Statistics of comparison for Figure 4.3 for $a_g(442)$. The values in the parenthesis indicate the results when $a_{dm}(442)$ is at least 10% of $a_g(442)$ and vice versa. The noise, ε that was added to the reflectance, is indicated in the first column.

ε	0%	10%	20%	30%
R^2	0.9215(0.949)	0.9199(0.947)	0.9107(0.936)	0.896(0.921)
slope	1.0131(1.027)	1.0118(1.026)	1.0076(1.02)	0.982(0.996)
intercept	-0.0648(-0.04)	-0.0588(-0.033)	-0.0692(-0.044)	-0.12(-0.09)
$RMSE_{log10}$	0.2450(0.206)	0.2467(0.209)	0.2602(0.23)	0.28(0.25)
e	0.7581(0.607)	0.7649(0.618)	0.8203(0.693)	0.907(0.787)
N	2439(1962)	2439(1962)	2439(1962)	2439(1962)

4.1.2 Field Data

For direct validation of the neural network we used both the NASA bio-Optical Marine Algorithm Data set (NOMAD) [*Werdell and Bailey*, 2005] as well as data collected in multiple field campaigns which include the Chesapeake Bay in 2005 and Long Island Sound in 2007 [*Gitelson et al.*, 2007; *Zhou et al.*, 2008]. We wish to emphasize that the NOMAD database, as well as our filed measurements, are only used to test results based on prior NN development and was not used in the actual training of

the NN, thereby providing a true independent testing approach. In the field campaigns the upwelling radiance $L_u(\lambda,0^-)$ was collected using a fiber bundle placed just beneath the water surface and connected to a GER spectroradiometer. The down welling irradiance above the surface $E_d(\lambda,0^+)$ was measured by pointing the same probe bundle at a Spectralon plate. The underwater r_{rs} is then $L_u(\lambda,0^-)/E_d(\lambda,0^+)$ and can be transformed to above surface R_{rs} by multiplying it by a 0.54 [*Hooker et al.*, 2002] surface transmission factor. At the same time an in-situ profiling package assembled by WET Labs (Philomath, Oregon) was deployed to record the related water properties: AC-S measuring absorption and attenuation coefficient between 400 to 750 nm, ECO-BB9 for backscattering coefficient measurement and CTD for temperature, salinity and depth data. Since our R_{rs} measurements are hyperspectral with a resolution of about 1nm we preprocess these by again convolving using MODIS SRF's [*MODIS Aqua SRF*].

The wavelengths for the R_{rs} measurements in the NOMAD dataset are multispectral, and the available wavelengths are slightly different since the data is a compilation of different contributors. In order to best represent the bands, which the network was trained on, and at the same time have a large enough dataset to properly validate our retrievals, we choose for the 547nm inputs, all the measurements at 547nm and the 555nm and for the 667nm - the 665nm and 670nm. For the cases when a channel around 531nm wasn't available we interpolate between 510 and 547 channels. For the blue channels we used the 412nm, 442nm and 489nm bands which match our inputs to the NN. A total of 3058 R_{rs} measurements were constructed in this way from which there are 936 available measurement for a, and 211 for b_b at 442nm.

For the detailed performance of the NN, we refer to Figures 4.4 - 4.7 and Tables 4.6 – 4.8. There is a slight underestimation of the low absorbing waters in the NOMAD dataset. We speculate that this could be due to calibration or due to the R_{rs} estimation. This underestimation doesn't appear in our field dataset since the absorption coefficient is significantly higher than the 0.1 m^{-1} where this underestimation occurs. Whether this underestimation comes from the simulations (modeling or Hydrolight) or from real errors in the measurement is difficult to assess and further exploration of measurement uncertainties should be performed in low absorbing waters.

Another parameter that is related to our retrievals of a and b_b is the diffuse attenuation coefficient, K_d, and there are 1971 NOMAD measurements available for this comparison. The relationship of the measured K_d to a and b_b as retrieved using this NOMAD data with the neural network is found to be:

$$K_d\left\{a(442), b_b(442)\right\} = 1.2574 \times \left\{a(442) + b_b(442)\right\} - 0.0030, \qquad (4.3)$$

Or in the logarithmic domain

$$K_d\left\{a(442), b_b(442)\right\} = 1.2314 \times \left\{a(442) + b_b(442)\right\}^{1.0089}, \qquad (4.4)$$

Eq.(4.3) is shown in Fig 4.4, where it can be seen that the resulting linear relationship has low dispersion, with correlation R^2=97.77%, even though the sun position effect as described in Eq. (10) in *Albert and Mobley* [2003] is ignored. The 1.2574 coefficient obtained, is in reasonable agreement with 1.0546/$cos(\theta_{sun})$, the same coefficient from. *Albert and Mobley* [2003] and which would vary from 1.4914 to

1.0546 for measurements ranging from θ_{sun} 45 to nadir. Although the relationship between the K_d and a plus b_b is plotted in the logarithmic domain as can be seen in Eq. (4.4), their relationship can be approximated by a linear relation Eq. (4.3).

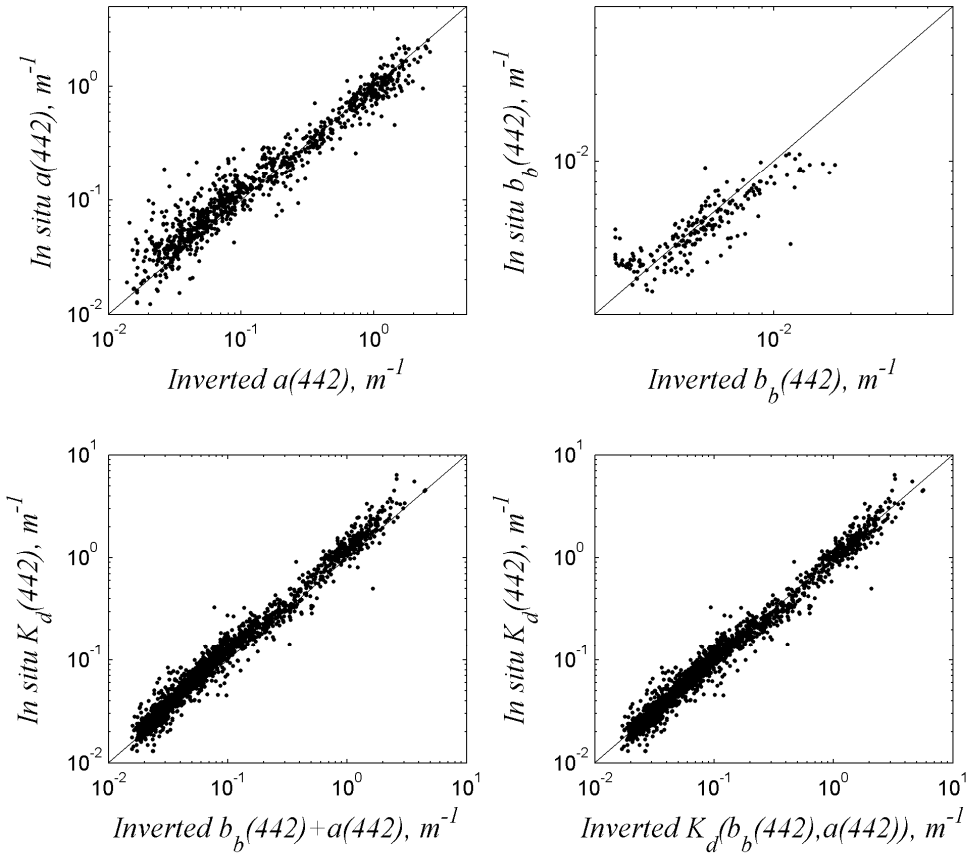

Fig. 4.4. Inverted IOP from the neural network (x-axis) plotted against the in situ values from the NOMAD dataset for $a(442)$ m^{-1}, $b_b(442)$ m^{-1} and K_d (442) m^{-1}. The lower graphs illustrate the relationship of $K_d(442)$ $m^{-1}$and $a(442)$ m^{-1} and $b_b(442)$ m^{-1} (left) and $K_d\{a(442),b_b(442)\}$ m^{-1} from Eq. (4.3) right. Refer to Table 4.7 for statistics.

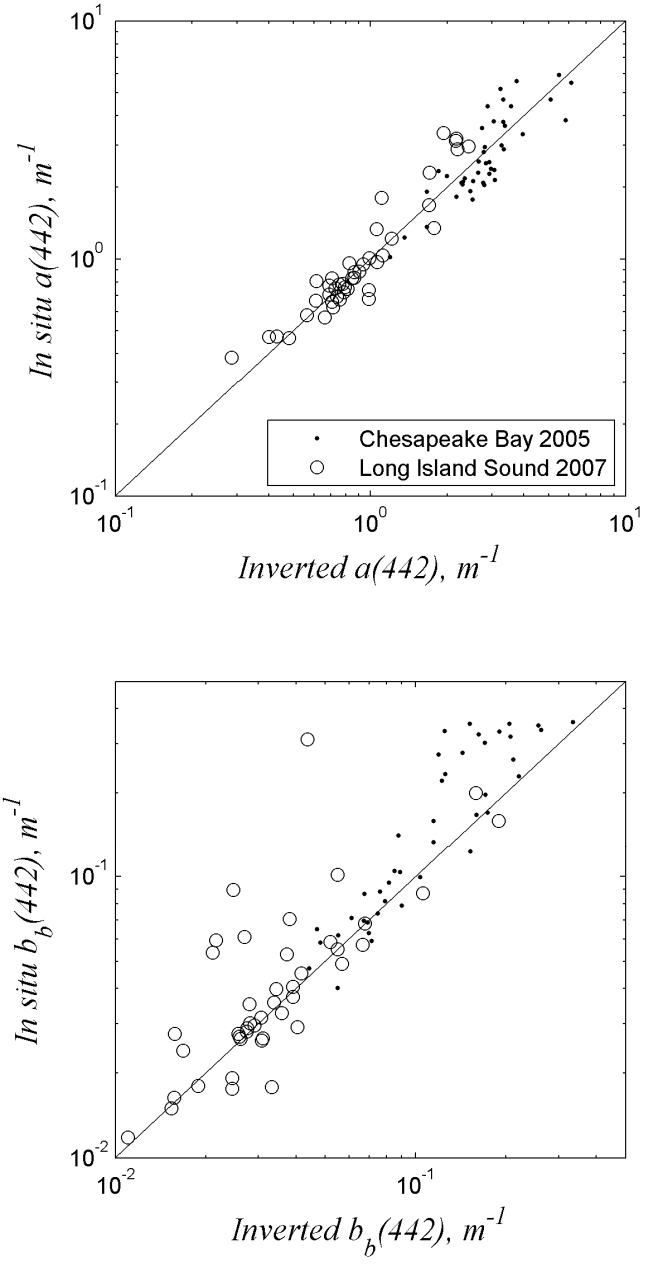

Fig. 4.5. Inverted IOP's from the neural network (x-axis) plotted against the in situ values for our field dataset for $a(442)$ m^{-1} (upper) and $b_b(442)$ m^{-1}(lower). The statistics are shown in the parenthesis in Table 4.6.

Table 4.6. Statistics of comparison for Figure 4.5 Chesapeake Bay and Long Island NY.

	$\alpha(442)$	$b_b(442)$
R^2	0.9187	0.8207
slope	0.9719	1.054
intercept	0.0093	0.1488
$RMSE_{log10}$	0.0909	0.1973
e	0.2329	0.5752
N	89	89

For the second network that was used to model the ratio of algal to non-algal absorption coefficient, we observe a consistent underestimation of the phytoplankton absorption (see Figure 4.6). We then adjusted the output of the second neural network so that the measurement and the retrieval have a slope of one and an intercept of zero. This is done by fitting the retrieved algal absorption to the measured one, and then substituting the fitted result of the neural network output into,

$$R_{a_{dg}}^{a_{ph}}(442) = \frac{a_{ph}(442)}{a_{pg}(442) - a_{ph}(442)} \tag{4.5}$$

Having the desired ratio and the output (before de-normalization) of the second neural network we can fit the two, in the $\log_{10}$ domain. What we are basically doing is adjusting the μ and σ of the second network output so that we can obtain a set of coefficients for these values that are based on measurements rather than the modeling in the simulations. This step required a small number of iterations since the underestimation of the algal absorption would become greater than the total absorption, after fitting it to the measured algal absorption, and thus negative values would appear

in the denominator of Eq. (4.5). Therefore those values must be excluded in the initial fitting. As the coefficients gradually adjust, there are no negative values, and a fit with a slope of one and an intercept of zero is obtained. These adjusted fitting coefficients were used when we separate the combined dissolved and non-algal particulate to its independent components of $a_{dm}(442)$ m^{-1} and $a_g(442)$ m^{-1}. With an estimation of the non-algal particulate a_{dm} (442) m^{-1} and the previous retrieval of the algal absorption $a_{ph}(442)$ m^{-1} we can obtain a new estimate of the particulate absorption coefficient where $a_p(442)$ m^{-1}= $a_{ph}(442)$ m^{-1}+$a_{dm}(442)$ m^{-1}. The particulate absorption, $a_p(442)$ m^{-1}, is plotted along with the retrievals of the $a_{dm}(442)$ m^{-1} and $a_g(442)$ m^{-1} against the in-situ measurements in Figure 4.7 and the corresponding statistics in Table 4.8 indicate that the results are in agreement with our simulated data although some disagreement is shown in the higher values of the $a_g(442)$ m^{-1}. The underestimation of the lower values of $a_g(442)$ m^{-1} are influenced by the underestimation of the total absorption coefficient at these low values (Figure 4.4).

Table 4.7. Statistics of comparison for Figures 4.4 and 4.6 for the NOMAD dataset. The values in the parenthesis for $a_{ph}(442)$ and $a_{dg}(442)$ indicate the statistics after the 'Fitting'(see text).

	$K_d(442)$	*$\alpha(442)$*	*$b_b(442)$*	*$\alpha_{ph}(442)$*	*$\alpha_{dg}(442)$*
R^2	0.978	0.9375	0.6169	0.9077(0.9067)	0.8688(0.8643)
slope	0.984	0.8745	0.5656	0.9965(1)	0.84(0.7872)
intercept	-0.013	-0.048	-1.018	0.181(0)	-0.1824(-0.14)
$RMSE_{log10}$	0.088	0.164	0.1277	0.2559(0.1765)	0.245(0.2944)
e	0.224	0.458	0.3418	0.8026(0.5015)	0.7578(0.9699)
N	1971	936	211	936(936)	936(936)

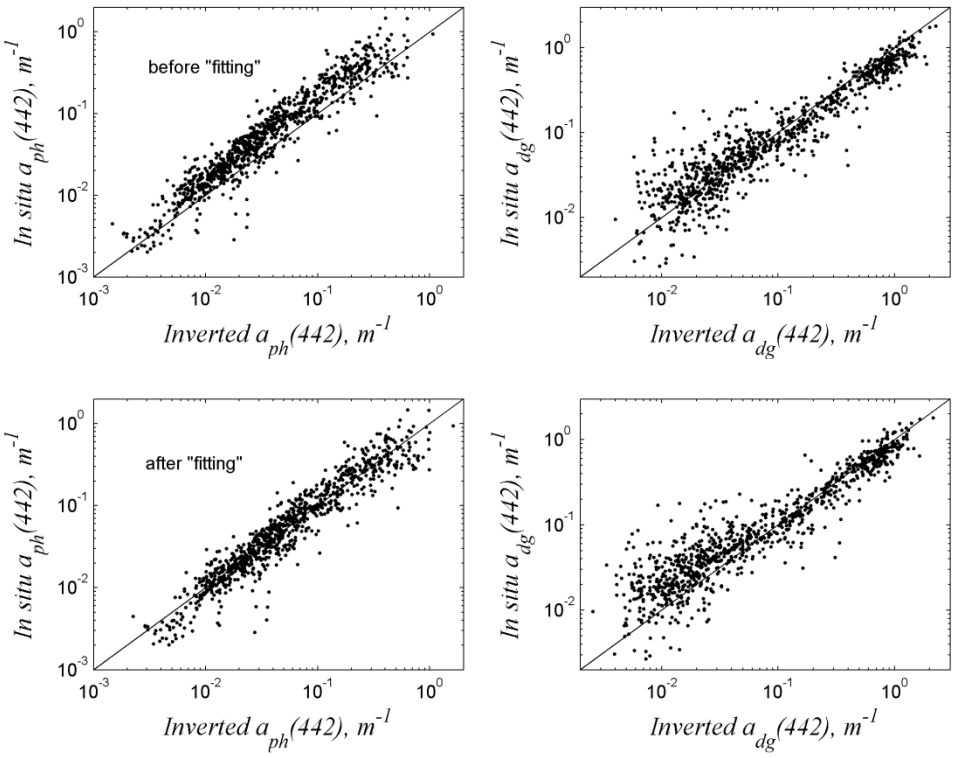

Fig. 4.6. Inverted IOP's from the neural network (x-axis) plotted against the in situ values from the NOMAD dataset for a_{ph} (442) $m^{-1}$and a_{gd} (442) m^{-1}. The first row represents the outputs of the neural network before "fitting" the output with the measurements (see text). The second row represents the results after the adjustment with the field data. Statistics are shown in Table 4.7.

Table 4.8. Statistics of comparison for the NOMAD dataset Figure 4.7 for a_{dm}(442) and a_g(442) and a_p(442), m^{-1}.

	$\alpha_{dm}(442)$	$\alpha_g(442)$	$\alpha_p(442)$
R^2	0.8724	0.7790	0.9342
slope	0.9438	0.7307	1.0042
intercept	-0.0912	-0.2454	0.0132
$RMSE_{log10}$	0.2819	0.3390	0.1599
e	0.9139	1.1828	0.4452
N	936	936	936

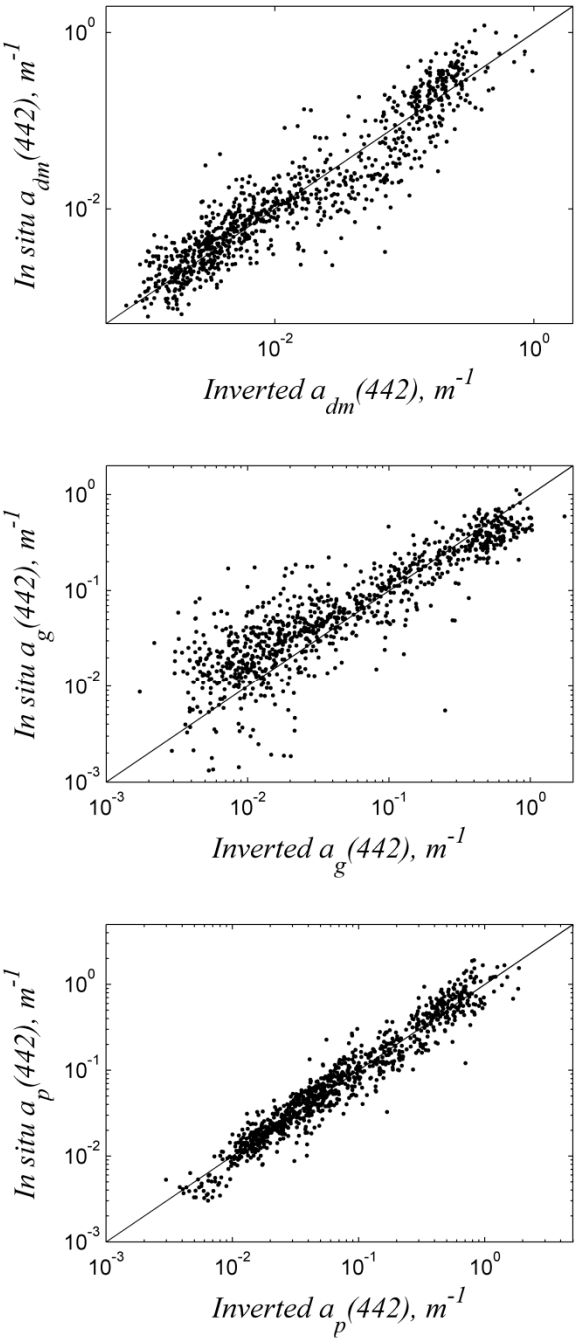

Fig. 4.7. Inverted IOP's from the neural network (x-axis) plotted against the in situ values from the NOMAD dataset for a_{dm} (442) m^{-1} (upper plot) and a_g (442) m^{-1} (middle) and a_p (442) m^{-1} (lower). The corresponding statistics are shown in Table 4.8.

4.2 Comparison of the Algorithms

4.2.1 Field Data

Following the successful testing of the NN on both the simulated and field datasets, we compare our algorithm with the Over-constrained linear matrix inversion algorithm [*Wang et al.*, 2005] as described in [IOCCG report 5, 2006] with both the 10% and the 20% criterion, as well as the QAA [*Lee et al.*, 2002] and for the latest update that was used in this study QAA-v5 [*Lee et al.*, 2009]. The R_{rs} used as input to these algorithms is described in the previous section. As it can be observed in Figure 8 all three algorithms have a similar retrieval for $a(442)$ $m^{-1}$when the 10% constraint is used. Similar behavior is observed when the 20% constraint is used (not shown). The statistics (see Table 4.9) are similar although the NN performs consistently better in all situations.

Table 4.9. Statistics of comparison of the three algorithms for $a(442)$ m^{-1}. N is the number of successful retrievals of the SAA (with the 10 and 20% criterion) and QAA.

	SAA	QAA-v5	NN	SAA	QAA-v5	NN	QAA-v5	NN
R^2	0.9255	0.9200	0.9402	0.9300	0.92	0.9393	0.924	0.9375
slope	0.8352	0.9319	0.8890	0.8137	0.910	0.872	0.822	0.875
intercept	-0.095	0.0405	-0.047	-0.066	0.025	-0.046	-0.073	-0.048
$RMSE_{log10}$	0.1471	0.1531	0.1216	0.1744	0.167	0.140	0.202	0.164
e	0.4032	0.4226	0.3231	0.4941	0.467	0.382	0.593	0.458
N	392	392	392	590	590	590	936	936

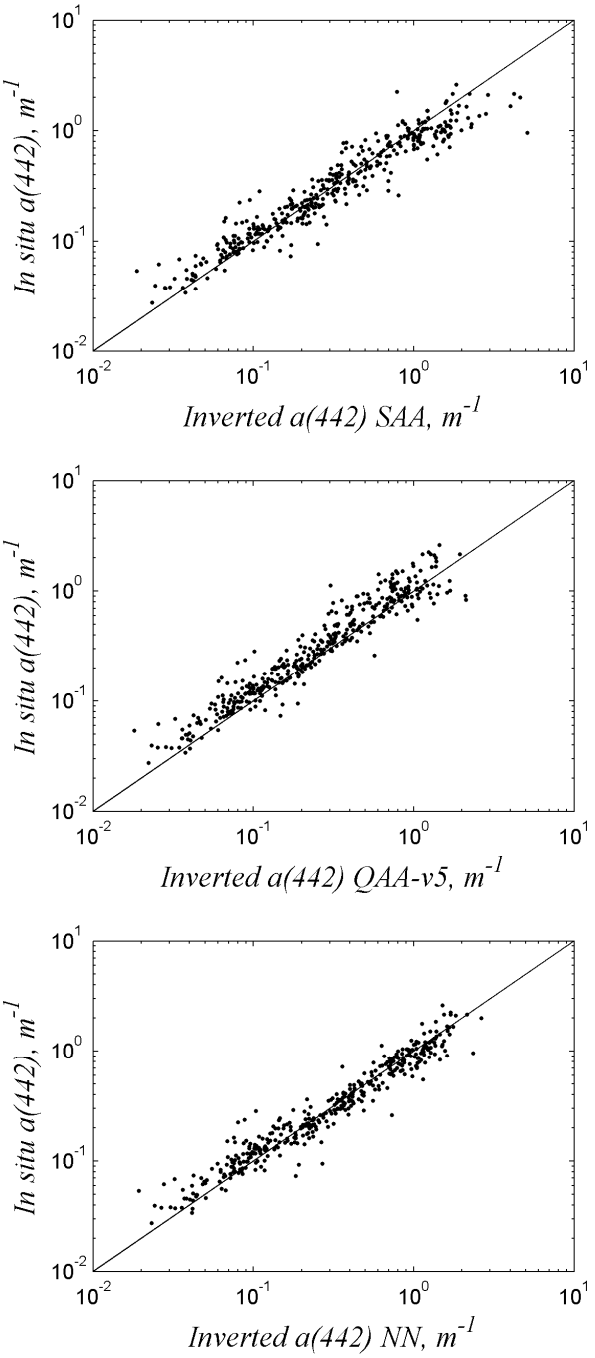

Fig. 4.8. Retrievals of the SAA, QAA and neural network (x-axis) vs. in-situ measurement for $a(442)$ m^{-1}.

Tables 4.10 – 4.12 illustrate the relationship of both algorithms for the remaining in situ measurement for all the cases that retrieval for the SAA and QAA was available. The number of successful retrievals, which are constrained by the SAA (10% and 20% criterion) as well as positive retrievals for the QAA, is indicated with the index N and it is shown at the bottom row of each Table. Although a good agreement (Figure 4.9) is also observed for $a_{ph}(442)$ for all three algorithms, the neural network performs significantly better.

Table 4.10. Statistics of comparison of the three algorithms for $a_{ph}(442)$ m^{-1}. N is the number of successful retrievals of the SAA (with the 10 and 20% criterion) and QAA.

	SAA	QAA-v5	NN	SAA	QAA-v5	NN	QAA-v5	NN
R^2	0.679	0.8033	0.8703	0.7741	0.7270	0.8725	0.8048	0.91
slope	0.716	0.8587	0.9971	0.6808	0.7821	0.9863	0.8968	1.004
intercept	-0.243	-0.147	0.0020	-0.230	-0.225	-0.009	-0.145	0.009
$RMSE_{log10}$	0.299	0.2094	0.1627	0.3451	0.2728	0.1717	0.2577	0.17
e	0.994	0.6195	0.4546	1.2137	0.8740	0.4850	0.8101	0.479
N	383	383	383	567	567	567	882	882

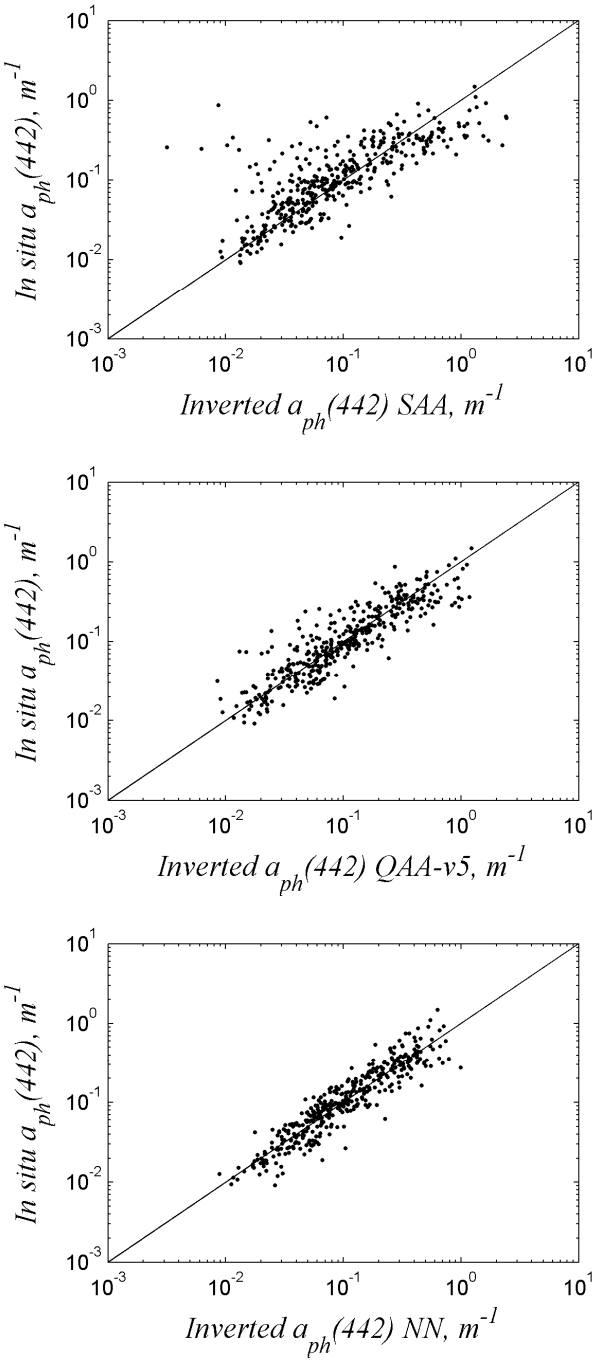

Fig. 4.9. Retrievals of the SAA, QAA, and neural network (x-axis) vs. in-situ measurement for $a_{ph}(442)$ m^{-1}.

For $a_{dg}(442)$ the statistics of all three algorithms are similar. It can be observed in Figure 4.10 that the NN output has a closer relationship with the measured $a_{dg}(442)$ when absorptions are greater than $0.1m^{-1}$. For $b_b(442)$ (Figure 4.11), since the data were not screened, the statistics illustrated in Table 4.12 are not representative of the accuracy of each algorithm as the outliers are probably due to error in the measurement of either $b_b(442)$ or R_{rs}.

Table 4.11. Statistics of comparison of the three algorithms for $a_{dg}(442)$ m^{-1}. N is the number of successful retrievals of the SAA (with the 10 and 20% criterion) and QAA.

	SAA	QAA-v5	NN	SAA	QAA-v5	NN	QAA-v5	NN
R^2	0.8939	0.8176	0.8703	0.8735	0.812	0.8725	0.81	0.856
Slope	0.8010	0.8927	0.8161	0.8122	0.888	0.7854	0.89	0.782
intercept	-0.164	0.0531	-0.135	-0.143	0.035	-0.140	0.019	-0.148
$RMSE_{log10}$	0.2029	0.2706	0.2058	0.2272	0.285	0.2436	0.311	0.3
E	0.5956	0.8645	0.6061	0.6872	0.929	0.7521	1.048	0.997
N	383	383	383	567	567	567	882	882

Table 4.12. Statistics of comparison of the three algorithms for $b_b(442)$ m^{-1}. N is the number of successful retrievals of the SAA (with the 10 and 20% criterion) and QAA.

	SAA	QAA-v5	NN	SAA	QAA-v5	NN	QAA-v5	NN
R^2	0.4131	0.4012	0.3441	0.5363	0.5133	0.4954	0.5913	0.617
slope	0.4121	0.7802	0.4042	0.4840	0.9431	0.4941	0.9956	0.566
intercept	-1.349	-0.484	-1.351	-1.189	-0.121	-1.166	0.0031	-1.02
$RMSE_{log10}$	0.1730	0.1228	0.1581	0.1401	0.1200	0.1368	0.1207	0.128
e	0.4895	0.3268	0.4391	0.3807	0.3183	0.3702	0.3205	0.342
N	96	96	96	153	153	153	211	211

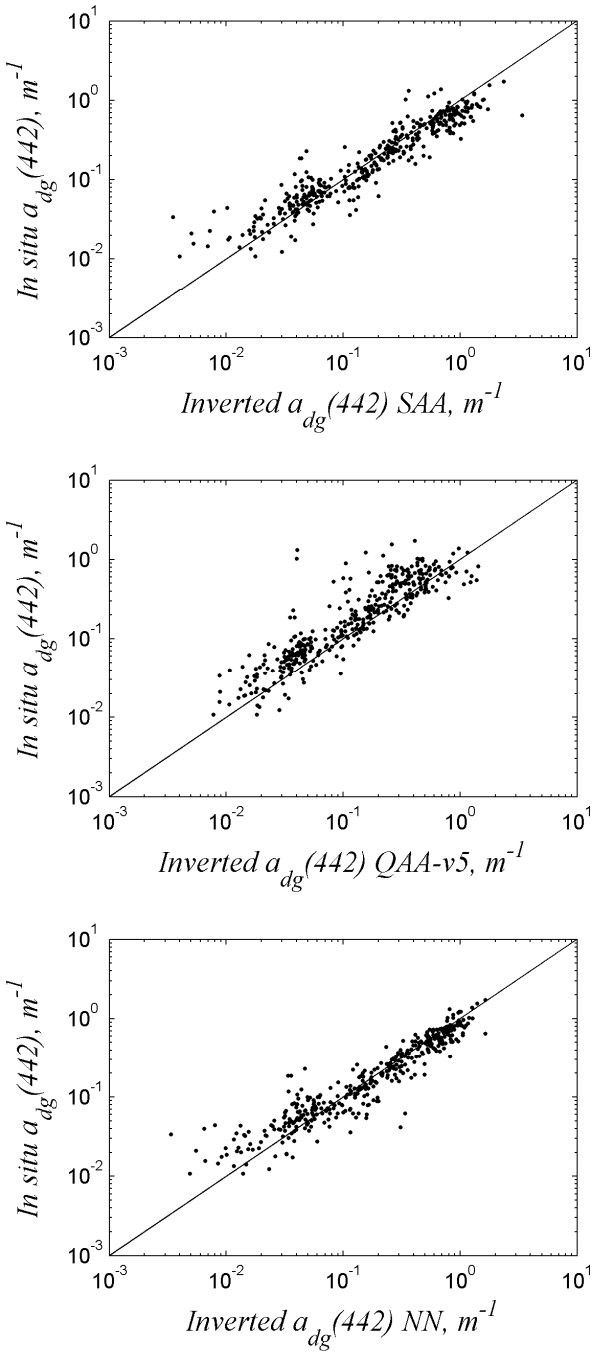

Fig. 4.10. Retrievals of the SAA, QAA and neural network (x-axis) vs. the in-situ measurement for $a_{dg}(442)$ m^{-1}.

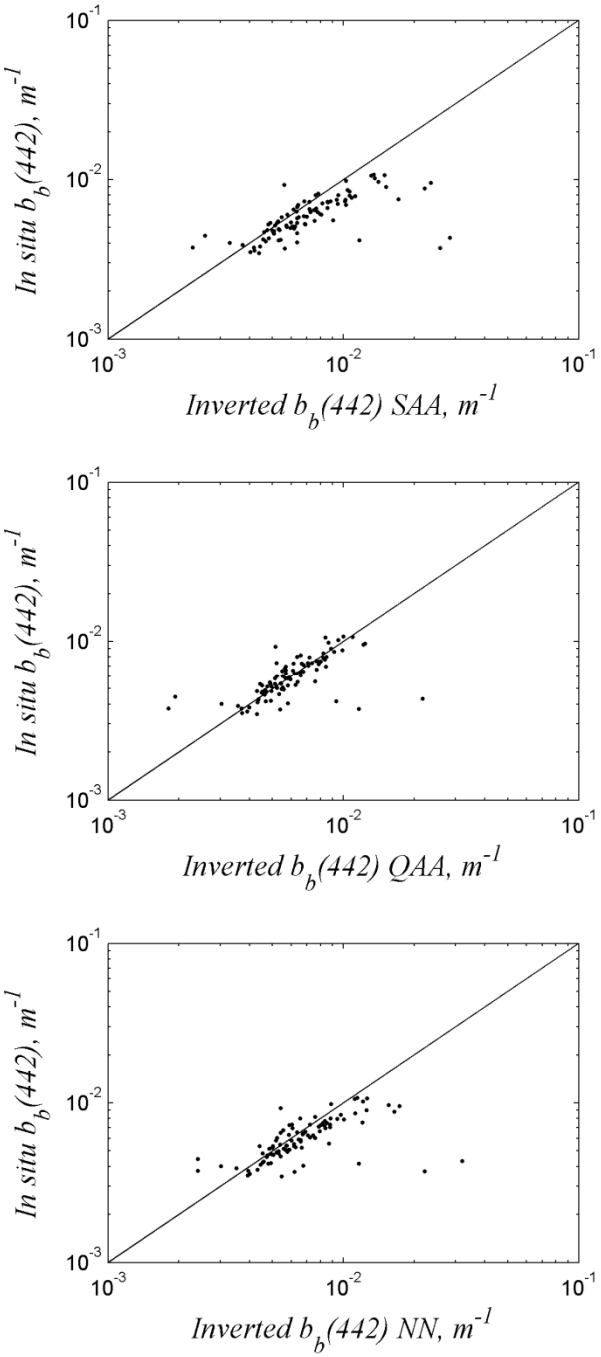

Fig. 4.11. Retrievals of the SAA, QAA and neural network (x-axis) vs. in-situ measurement for $b_b(442)$ m^{-1}.

4.2.2 Implementation on Satellite Data

Following the successful testing of our neural network, we explore its robustness when applied to satellite imagery. The image chosen here is a level 2 file illustrating the east coast of the US and is directly downloadable from the NASA Ocean Color website (http://oceancolor.gsfc.nasa.gov/) for May 3rd 2005 (file#A2005123181500.L2_LAC). We choose this region because we have performed extensive measurements there, and at the same time it represents a good example, since this region covers all the range of water types, from clear to turbid. Before analyzing the image we eliminated the unrealistic R_{rs} retrievals, those that were negative or had unrealistically high values. More specifically, the pixels that were not eliminated are the ones that meet the following criteria: R_{rs} at all input wavelengths must be greater than 10^{-4}, $R_{rs}(488)/R_{rs}(547)$ must be less than 5, $R_{rs}(412)/R_{rs}(443)$ less than 3.5 and greater than 0.1 and finally $R_{rs}(667)$ must be less than $R_{rs}(547)$ and less than 0.06. All points in our simulated data fall within these criteria. After this elimination 179824 pixels were left for analysis. The retrieved parameters of $a(442)$, $a_{ph}(442)$, $a_{dg}(442)$, $a_g(442)$, $a_{dm}(442)$ and $b_b(442)$ are shown in the images illustrated in Figures 4.12, 4.16, 4.20 and 4.21. Based mainly on visual inspection of these images, and noting that no anomalous discontinuities or graininess occurs, the results seem quite reasonable. To go beyond the visualization of the image we apply the SAA and QAA to the same image. When applied to the same pixels, the SAA produced about 86% (154424 pixels) successful inversions for all parameters. An insignificant amount of these retrievals are in the turbid region of Chesapeake Bay indicating that this algorithm cannot find a solution in these waters and this is probably due to the poor remote estimation of the

water leaving signal in these regions, mainly due to errors in the estimation of the atmospheric signal. Images of the available retrievals of the SAA are shown in the images in Figure 4.13 and Figure 4.17. Although the QAA has 100% retrieval for $a(442)$ and $b_b(442)$ and almost 100% for $a_{dg}(442)$, there are only about 73% positive values for $a_{ph}(442)$. The significantly reduced number of retrievals of QAA for $a_{ph}(442)$ is due to the poor estimation of $R_{rs}(412)$. The QAA retrievals where not plotted as they are very similar to the neural network algorithm, especially for the total absorption and backscattering coefficients. The NN algorithm has excellent agreement (as expected) with both the SAA and QAA when we compare the $a(442)$ and $b_b(442)$ retrievals (see Figure 4.14 and Figure 4.15).

Good correlation (Figure 4.18) also exists with both algorithms for $a_{dg}(442)$ m^{-1}. In contrast, the correlation, although still present, degrades significantly for $a_{ph}(442)$ m^{-1} (Figure 4.19). This is due to difficulties arising from the separation of the algal and non-algal absorptions. It should be noted that the NN approach is capable of retrievals for all cases, for all parameters, whereas the SAA algorithms are not.

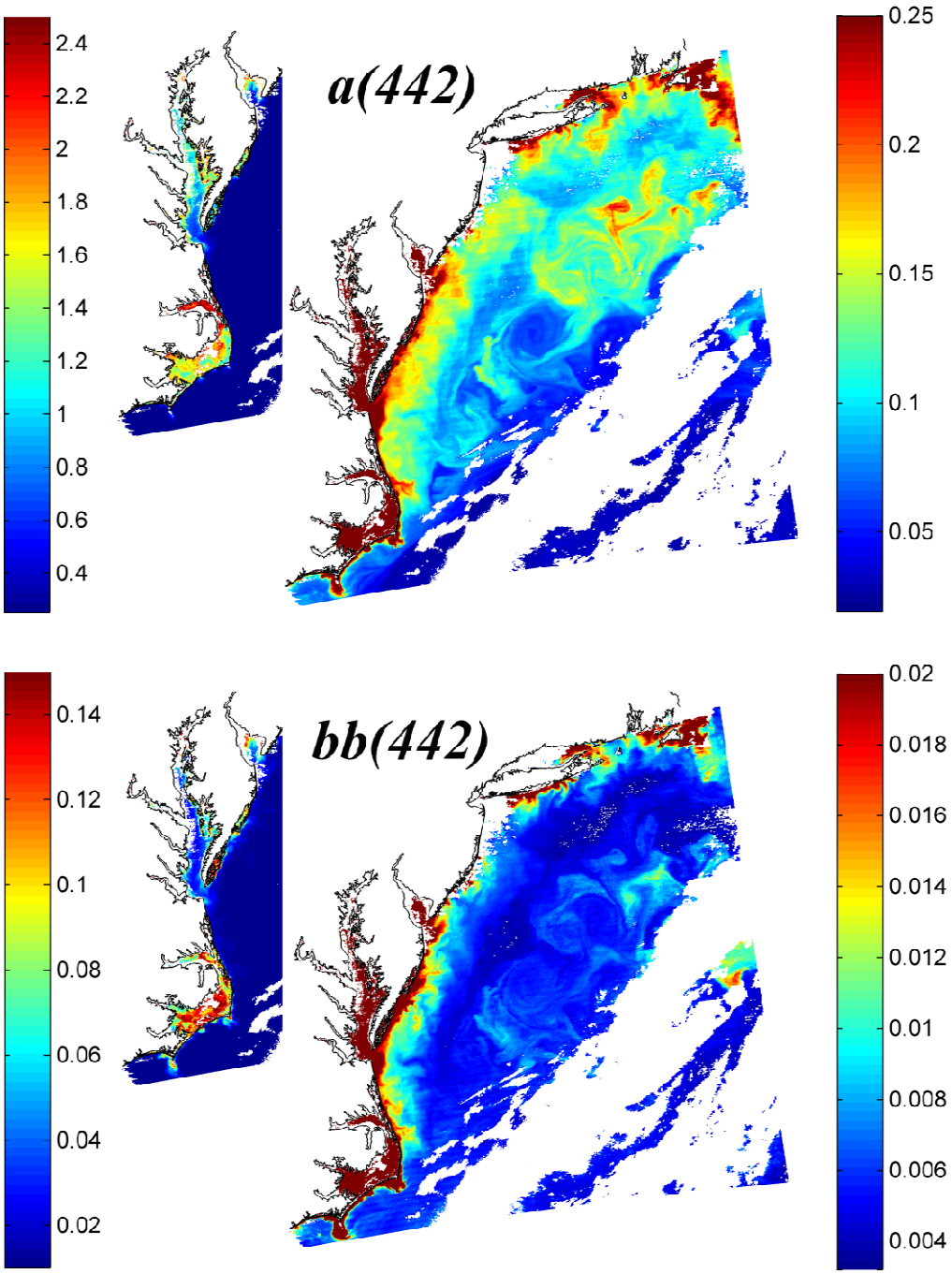

Fig. 4.12. Retrievals of the neural network of the total absorption coefficient, $a(442)$ m^{-1}(upper), and the total backscattering coefficient $b_b(442)$ m^{-1} (lower). The color bar is adjusted in the smaller images on the left to make the turbid regions visible.

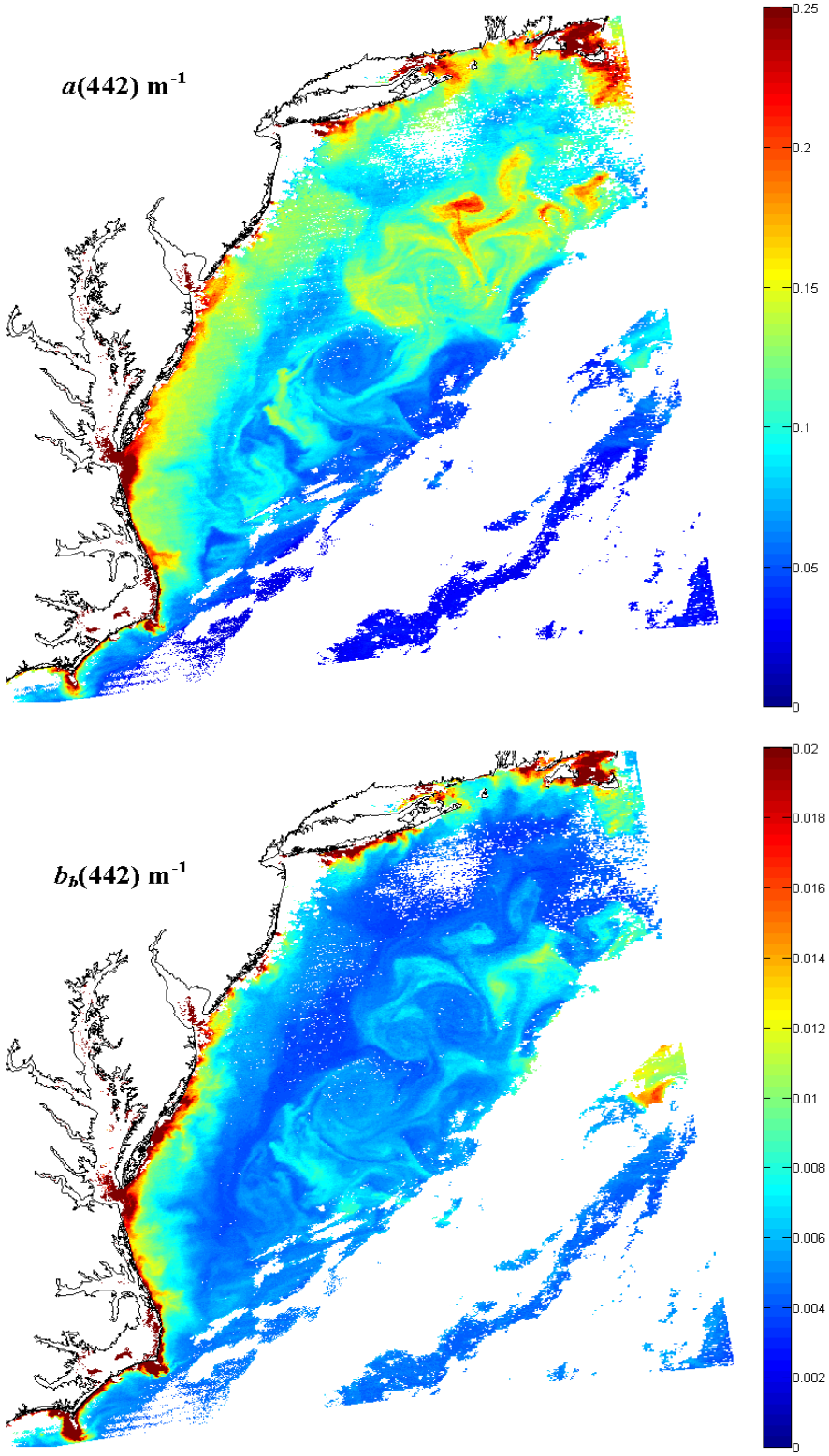

Fig. 4.13. Retrievals of the SAA of the total absorption coefficient, $a(442)$, m^{-1} (upper), and the total backscattering coefficient $b_b(442)$ m^{-1} (lower).

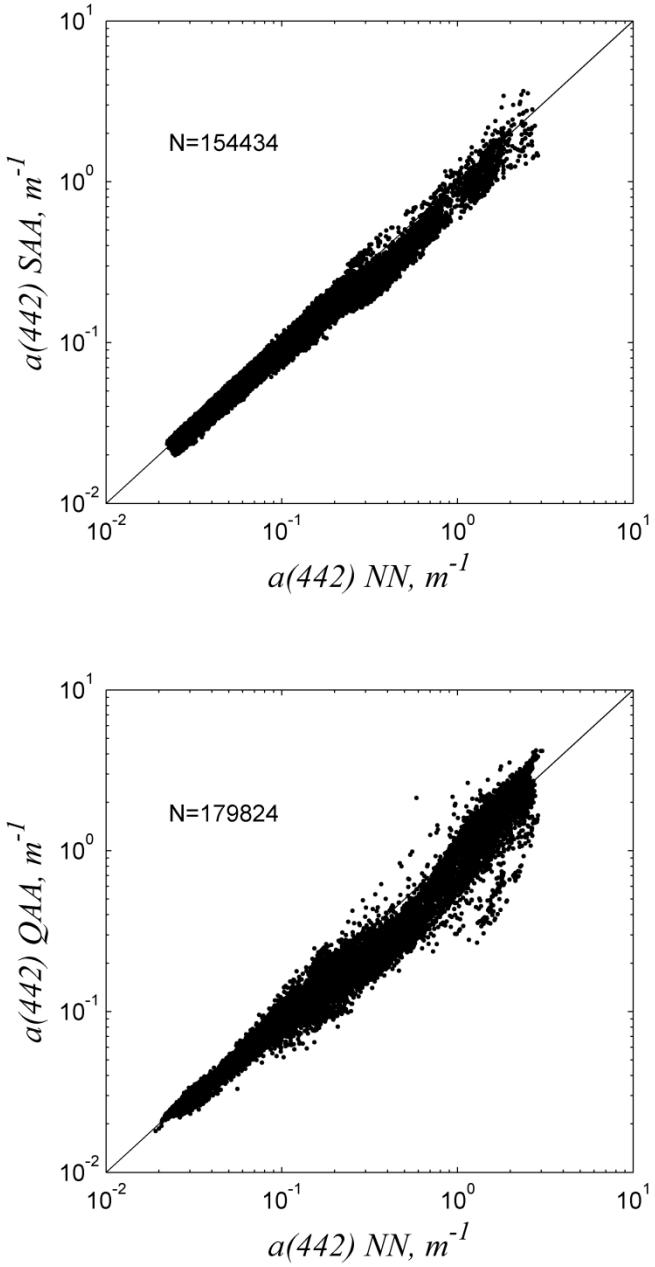

Fig. 4.14. The NN retrieval of $a(442)$ m^{-1} x-axis plotted against the SAA (top) and QAA (lower). R^2=99.16 with a slope of 0.9421 and an intercept of -0.0945 for the SAA, and R^2=0.9915, a slope of 1.0365 and an intercept of -0.0359 for the QAA. All the available retrievals for all algorithms are shown.

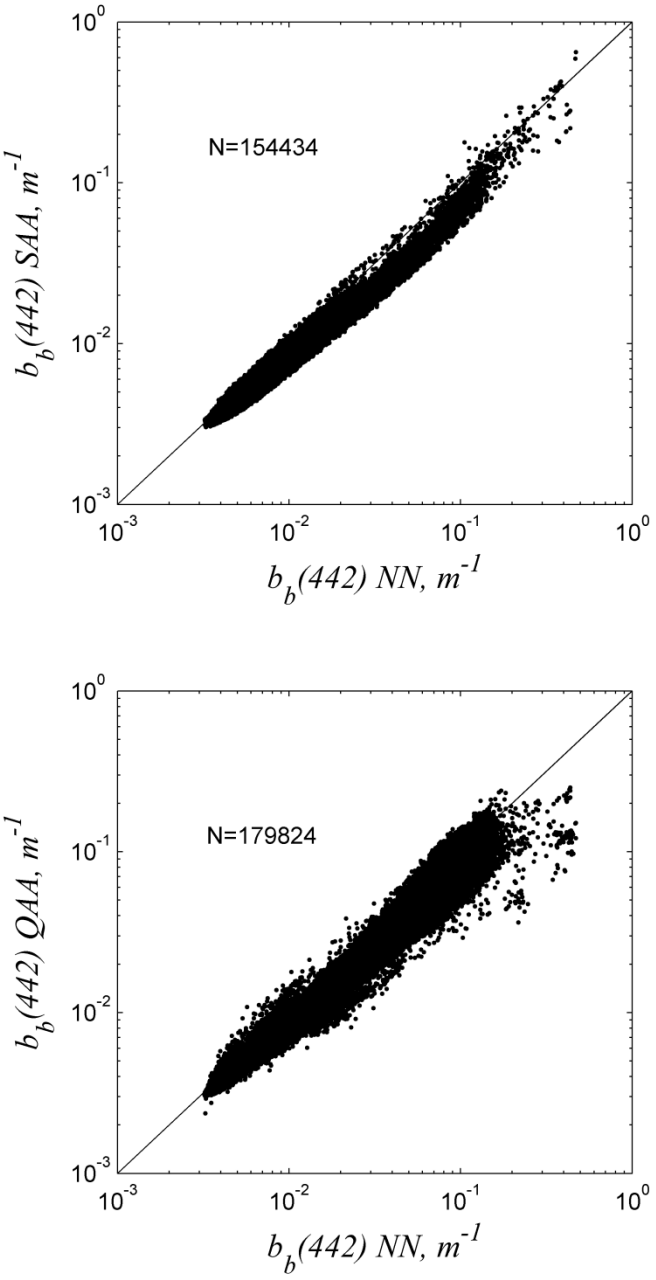

Fig. 4.15. The NN retrieval of $b_b(442)$ m^{-1} x-axis plotted against the SAA left and QAA right. R^2= 0.9822 with a slope of 0.8854 and an intercept of -0.298 for the SAA, and R^2= 0.9866, a slope of 0.9426 and an intercept of -0.18 for the QAA. All the available retrievals for all algorithms are shown.

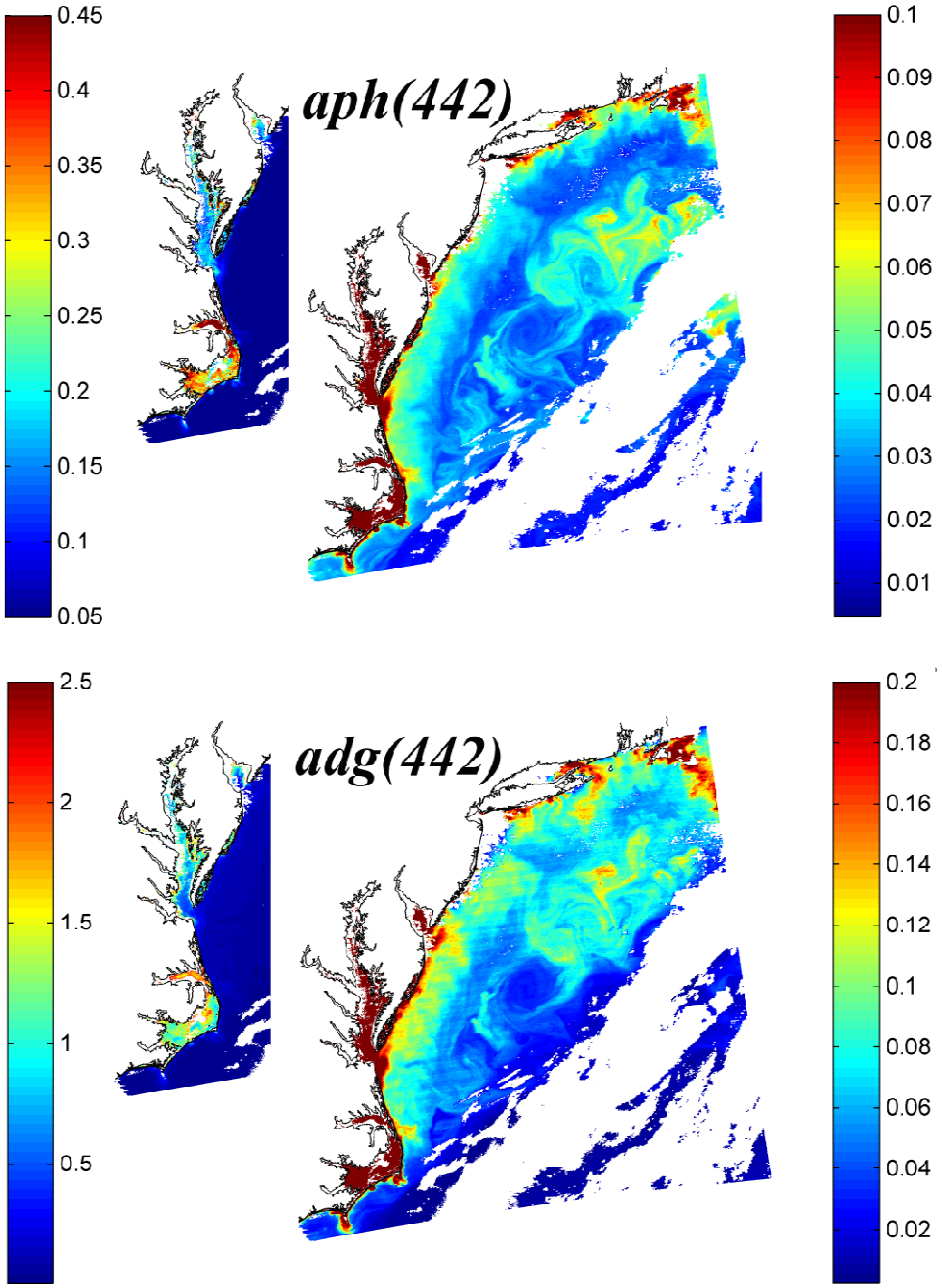

Fig. 4.16. Retrievals of the neural network of the phytoplankton absorption coefficient, $a_{ph}(442)$ m^{-1} (upper), and the non-algal and dissolved absorption coefficient $a_{dg}(442)$ m^{-1} (lower). The color bar is adjusted in the smaller images on the left to make the turbid regions visible.

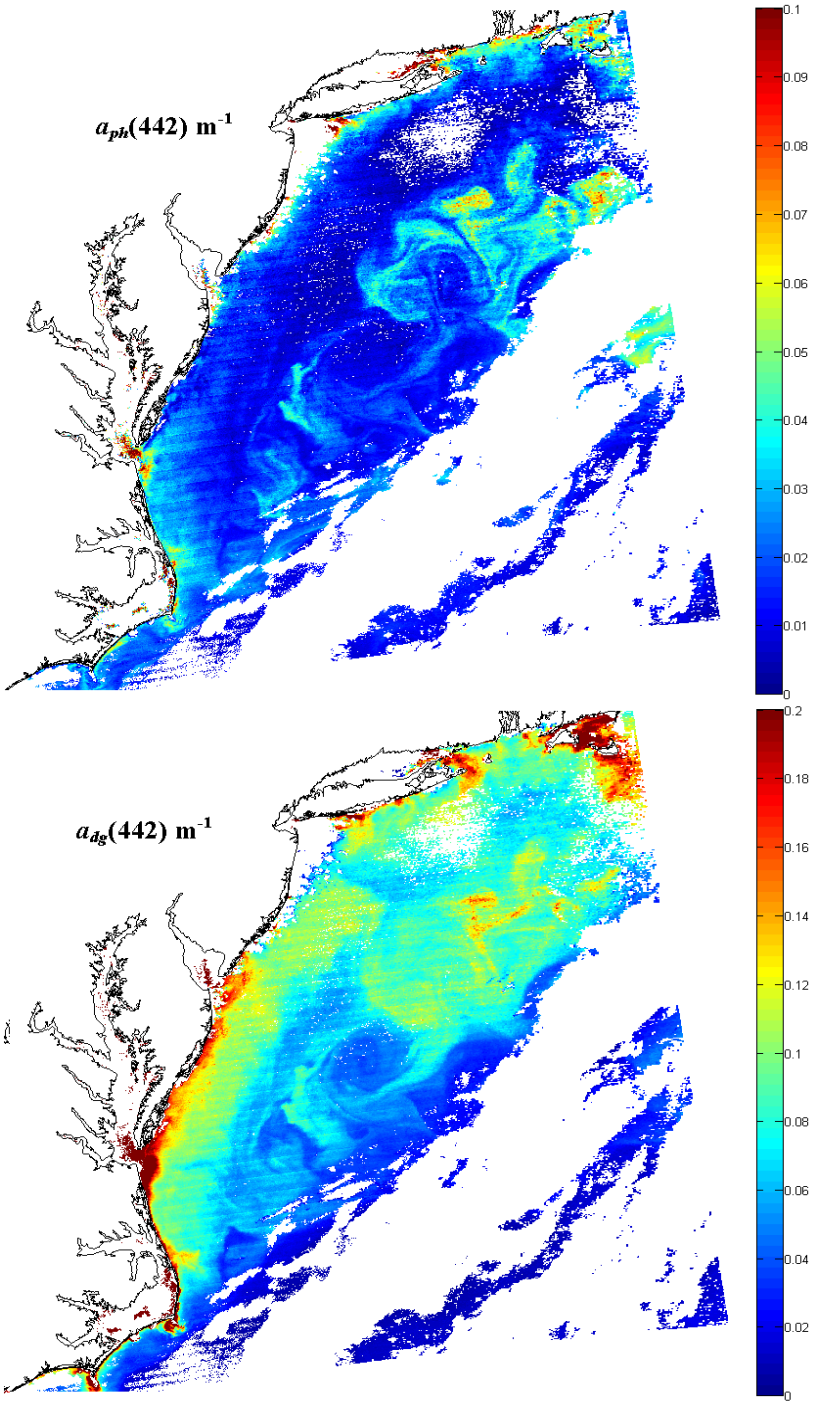

Fig. 4.17. Retrievals of the SAA of the phytoplankton absorption coefficient, $a_{ph}(442)$ m^{-1} (upper), and the non-algal and dissolved absorption coefficient $a_{dg}(442)$ m^{-1} (lower).

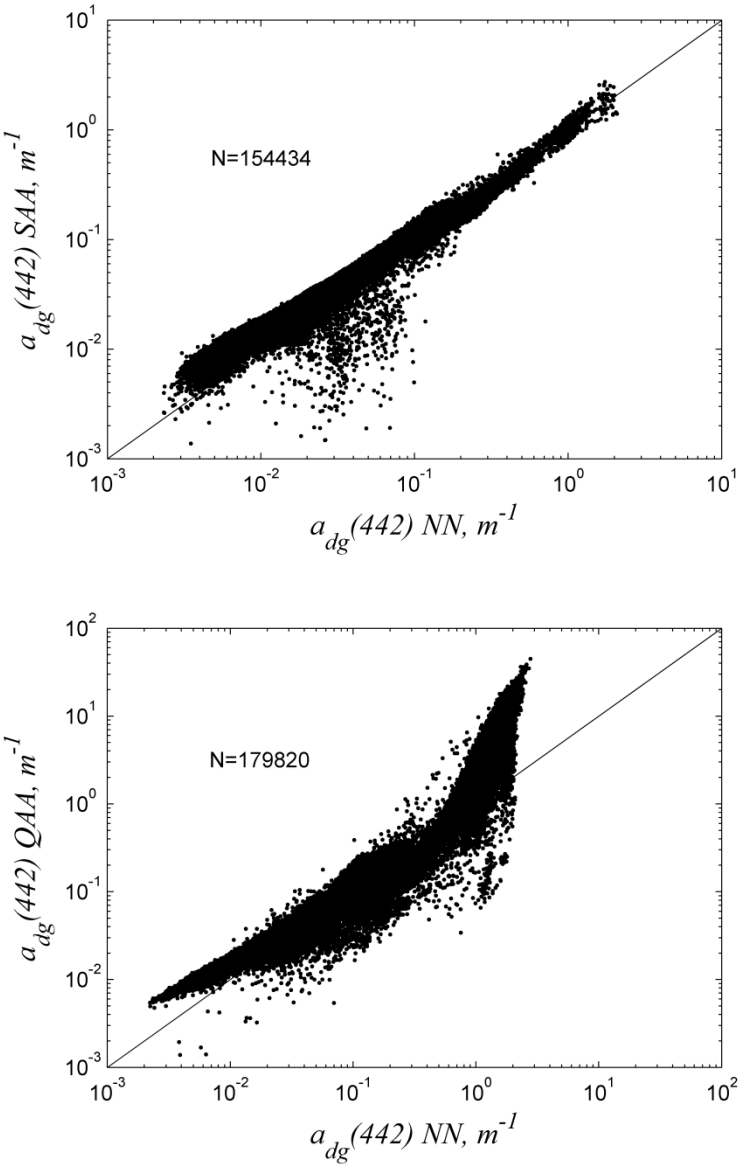

Fig. 4.18. The NN retrieval of $a_{dg}(442)$ m^{-1} x-axis plotted against the SAA (top) and QAA (lower). R^2= 0.9806 with a slope of 0.8569 and an intercept of -0.1179 for the SAA, and R^2= 0.9620, a slope of 1.0143 and an intercept of 0.0948 for the QAA. All the available retrievals for all algorithms are shown.

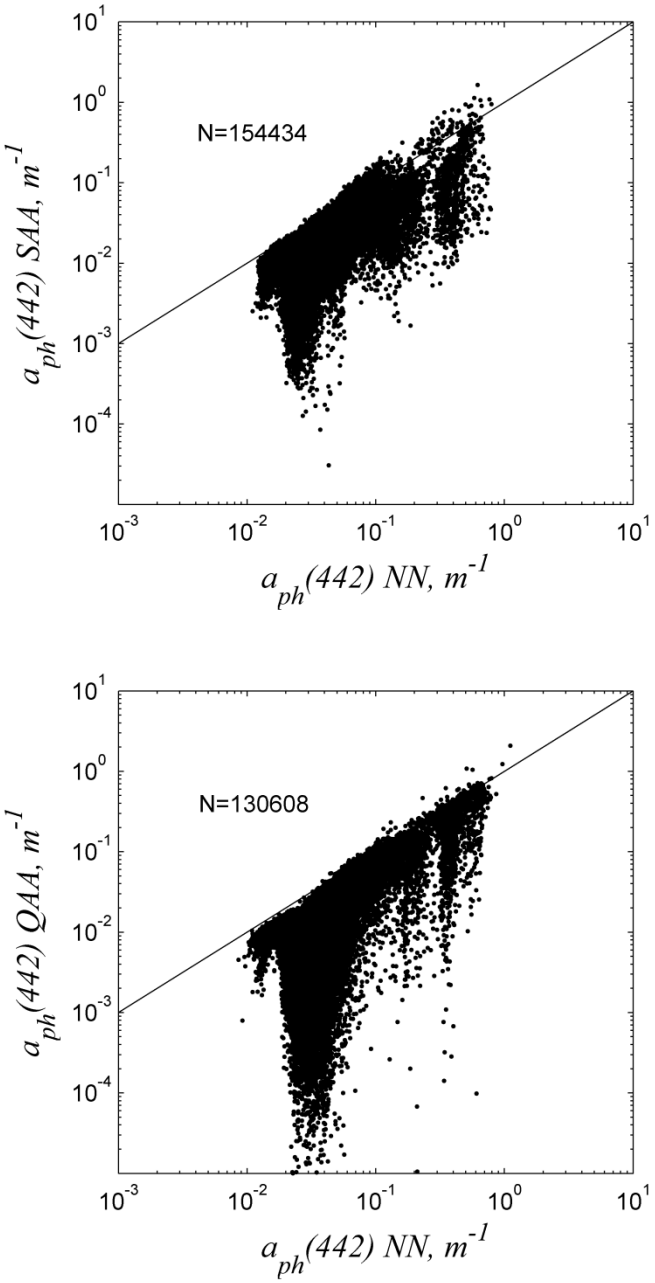

Fig. 4.19. The NN retrieval of $a_{ph}(442)$ m^{-1} x-axis plotted against the SAA (top) and QAA (lower). R^2= 0.6893 with a slope of 1.0641 and an intercept of -0.2264 for the SAA, and R^2=0.5949, a slope of 1.0802 and an intercept of -0.2648 for the QAA. All the available retrievals for all algorithms are shown.

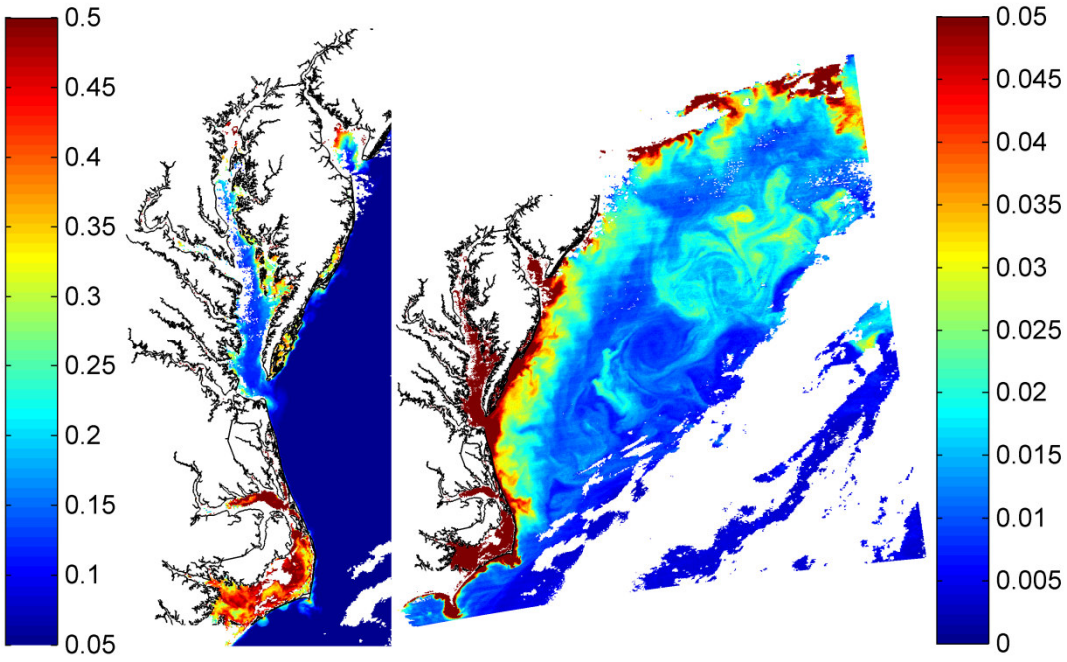

Fig. 4.20. Retrievals of the neural network of the non-algal particulate absorption coefficient, $a_{dm}(442)$ m^{-1}. The color bar is adjusted in the left image to make the turbid regions visible.

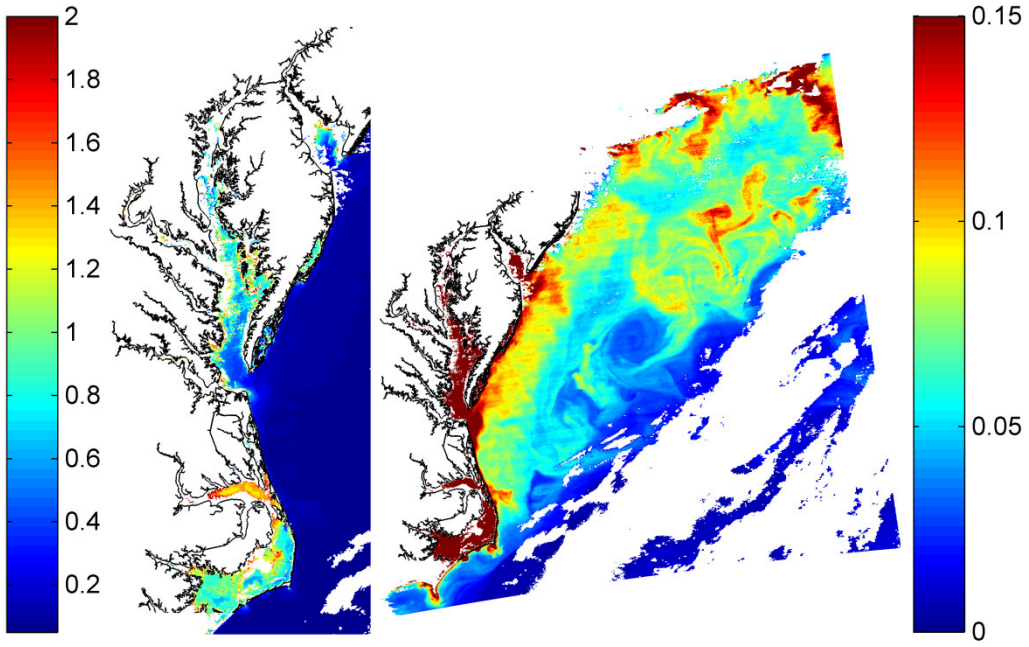

Fig. 4.21. Retrievals of the neural network of the dissolved absorption coefficient $a_g(442)$ m^{-1}. The color bar is adjusted in the left image to make the turbid regions visible.

As a further consistency check, we also observe a relationship between the derived specific absorption of algae and the [*Chl*] mg m^{-3} obtained from MODIS. This relationship is illustrated in Figure 4.22 and indicates the decrease of the specific absorption with the increase in [*Chl*] mg m^{-1}. Superimposed onto this relationship are the models from [*Morel,* 1991], [*Bricaud et al.*, 1995] and [*IOCCG Dataset,* 2003]. Specific absorptions observed of less than 0.01 are probably due to CDOM contaminated [*Chl*] mg m^{-3} retrievals since these values consistently appear at higher [*Chl*] mg m^{-3}. To show this underestimation we look for a relationship between the retrieved $a_{ph}(442)$ m^{-1} and the [*Chl*] mg m^{-3}. As can be seen in Figure 23 we can see the

difference between case 1 and case 2 waters. Noticeably in case 2 waters there is no relationship between the $a_{ph}(442)$ m^{-1} derived from the neural network algorithm and the MODIS product of [*Chl*] mg m^{-3}. The disagreement of the two algorithms in the higher [*Chl*] mg m^{-3} (red ellipse) values indicates case 2 waters. There is a very good agreement between the two algorithms for all other cases, namely case 1 waters. This pattern results from the fact that the main three absorption components covary to some extent.

Since we don't have other products to compare our retrievals of $a_g(442)$ m^{-1} $a_{dm}(442)$ m^{-1} we explore relationships between to empirical variables. A relationship between the measured $R_{rs}(667)$ sr^{-1} and the non-algal particulate should exist as these particulates are significant scatterers. This relationship is shown in Figure 4.24. The spread in this relationship exists due to the slope of the scattering function of these particulates as well as the increased non water absorption (mostly due to algae) at 667 nm. Despite these factors a very close relationship between the two variables exists. On the other hand no relationship exists between the retrieved CDOM absorption, $a_{dm}(442)$ m^{-1}, as these constituents are very insignificant contributors to the scattering. This relationship is shown in Figure 4.25 where the apparent relationship between the $R_{rs}(667)$ sr^{-1} and $a_g(442)$ m^{-1} for the low absorbing waters (usually case 1) is most likely due to the co-variation of the dissolved substance with the other scattering constituents .

Since the dissolved substance is dominating the light absorption in the Blue region of the spectrum and the non- algal particulates are not so effective absorbers a relationship between the traditional blue green ratio $R_{rs}(488)/R_{rs}(547)$ and $a_g(442)$ m^{-1}

should be more prominent, where a less prominent (if any) relationship should exist for the $a_{dm}(442)$ m^{-1}. As can be seen from Figure 4.26 and Figure 4.27 our assumptions about the relationship between the Blue Green ratio and these two parameters are true. A week relationship between $a_{dm}(442)$ m^{-1} and $R_{rs}(488)/R_{rs}(547)$ does exist. The relationship between $a_g(442)$ m^{-1} and $R_{rs}(488)/R_{rs}(547)$ is much stronger as expected.

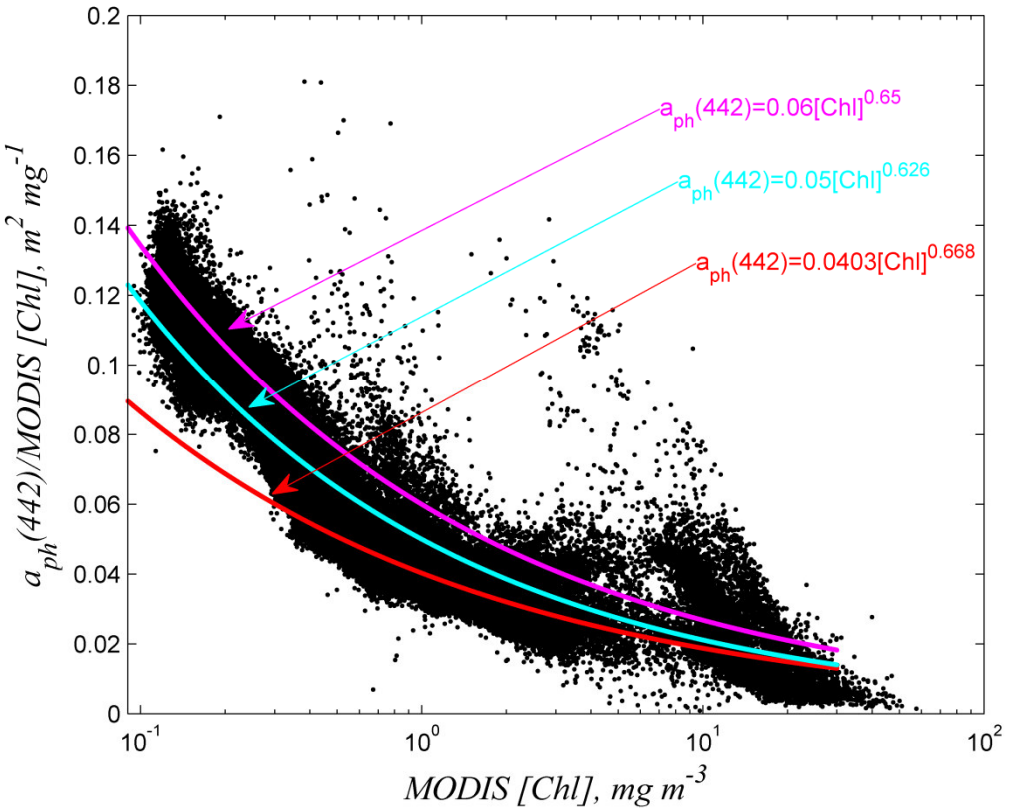

Fig. 4.22. The MODIS [*Chl*] product x-axis plotted against the NN retrieval of $a_{ph}(442)$ m^{-1} divided by the MODIS [*Chl*] mg m^{-3} (specific absorption of algae). Specific absorptions of less than 0.01 which consistently appear in the higher [*Chl*] mg m^{-3} are probably due to CDOM contaminated [*Chl*] mg m^{-3} retrievals. Three models are shown from [*Morel,* 1991] (magenta), [Bricaud, 1995] (red) and [*IOCCG Dataset,* 2003] (cyan).

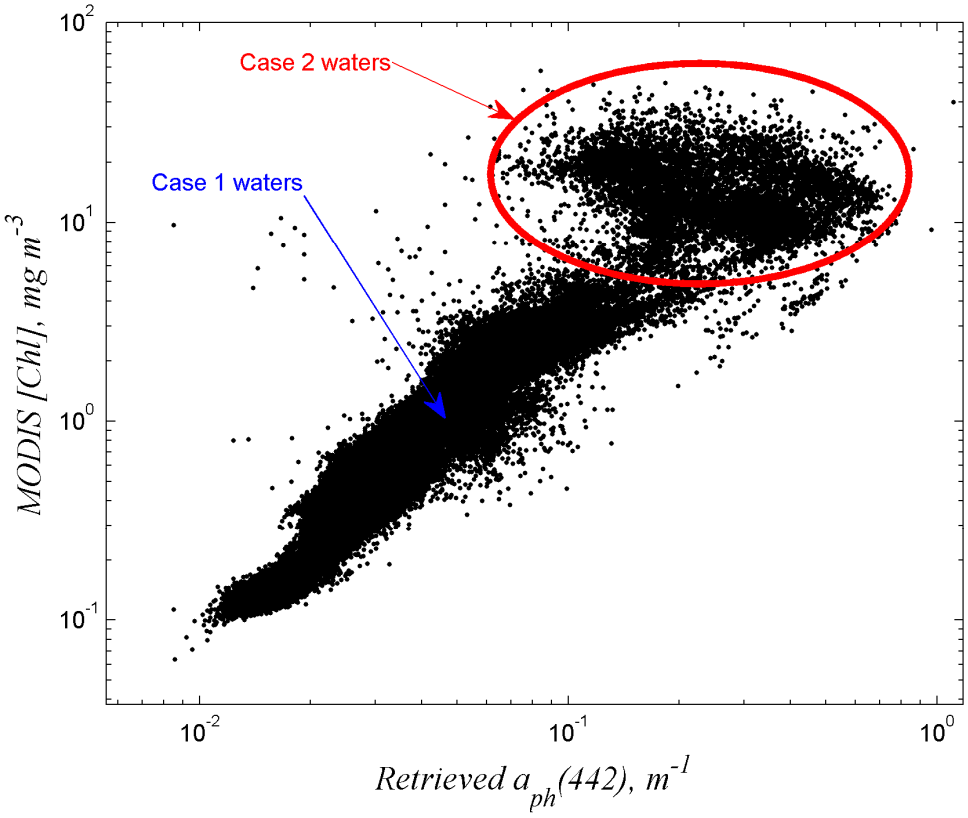

Fig. 4.23. The NN retrieval of $a_{ph}(442)$ m^{-1} x-axis plotted against the MODIS [*Chl*] mg m^{-3} product. The disagreement of the two algorithms in the higher [*Chl*] mg m^{-3} (red ellipse) values indicates case 2 waters. There is a very good agreement between the two algorithms in the [*Chl*] mg m^{-3} for all other cases indicating that the all constituents increase in a similar manner which indicates case 1 waters.

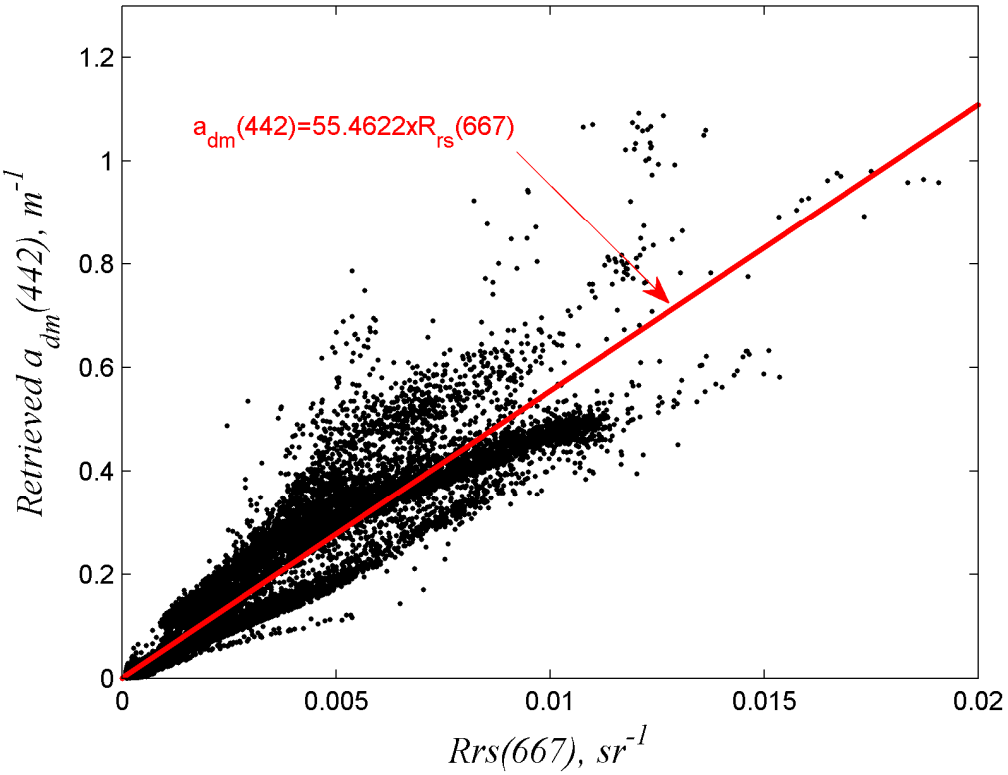

Fig. 4.24. The MODIS measurement of $R_{rs}(667)$ sr^{-1} x-axis plotted against the NN retrieval of $a_{dm}(442)$ m^{-1}. The red line indicates the relationship between the two parameters.

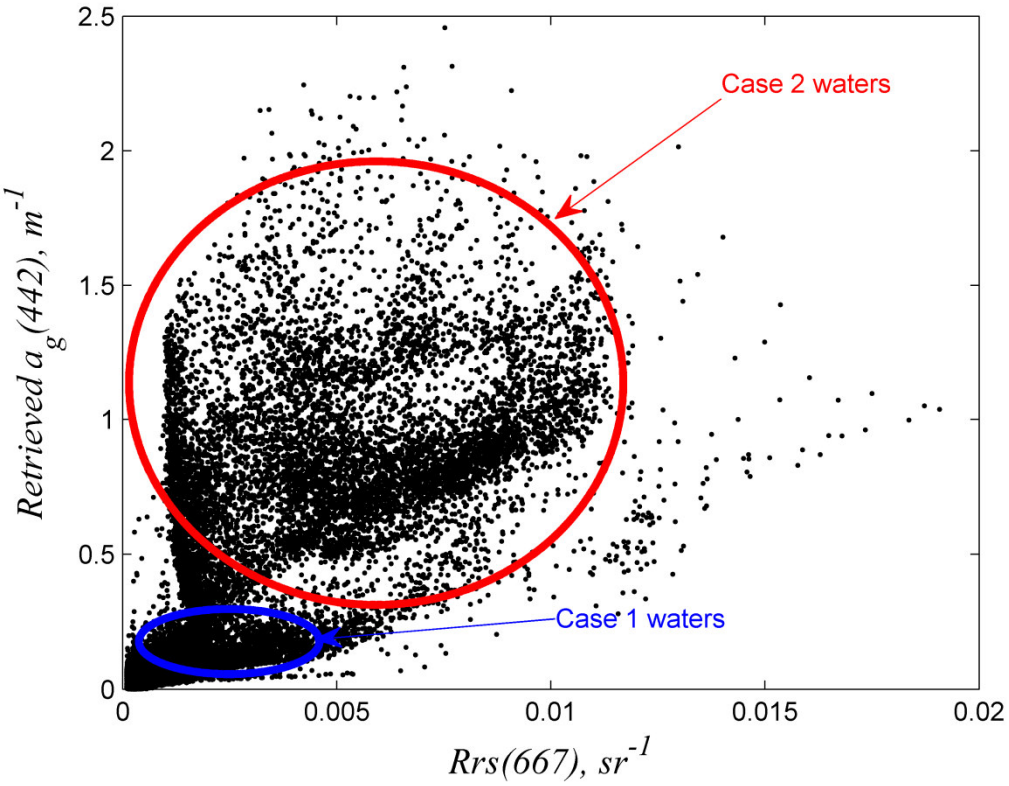

Fig. 4.25. The MODIS measurement of $R_{rs}(667)$ sr^{-1} x-axis plotted against the NN retrieval of $a_g(442)$ m^{-1}. The two ellipses indicate Case 1(blue) and Case 2(red) waters. The apparent relationship between the $R_{rs}(667)$ sr^{-1} and $a_g(442)$ m^{-1} for the low absorbing waters (usually case 1) is most likely due to the co-variation of the dissolved substance with the other scattering constituents .

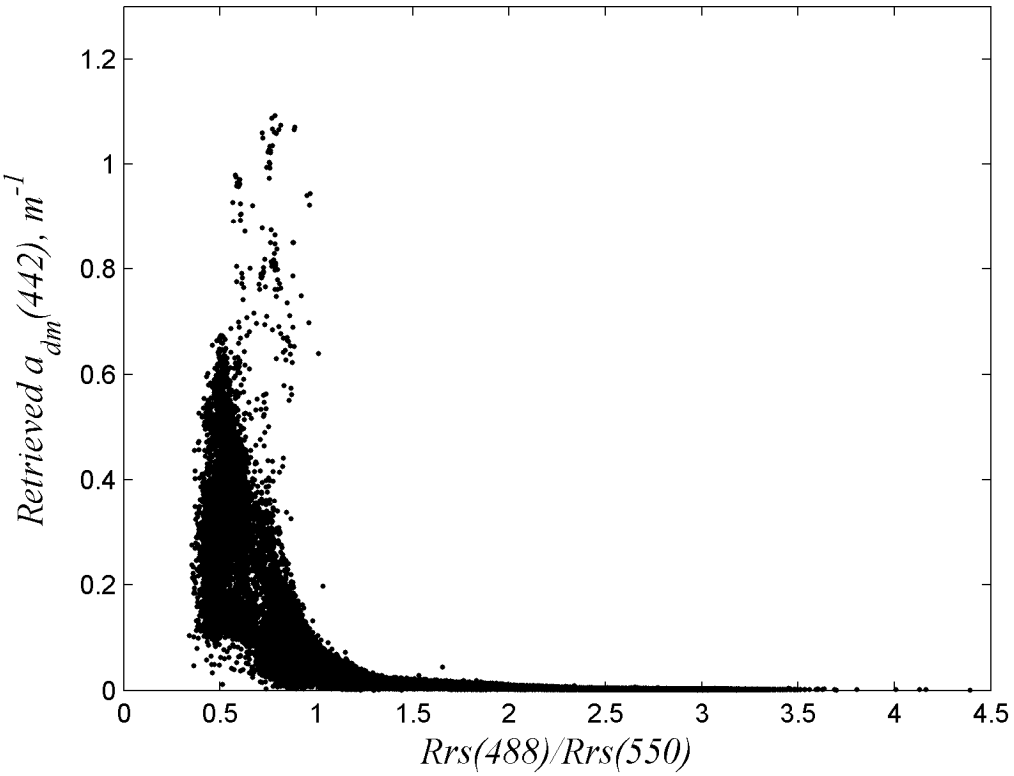

Fig. 4.26. The MODIS Blue Green ratio $R_{rs}(488)/ R_{rs}(547)$ x-axis plotted against the NN retrieval of $a_{dm}(442)$ m^{-1}. The relationship between these two parameters is weak as the non-algal particulate absorption is not dominant.

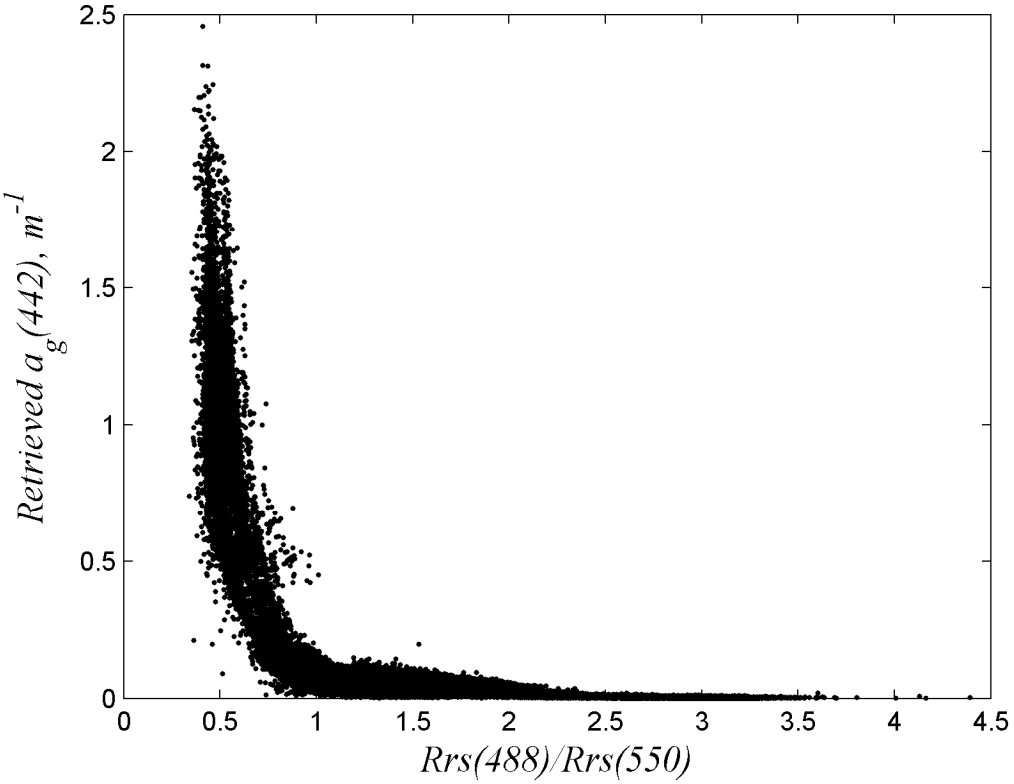

Fig. 4.27. The MODIS Blue Green ratio $R_{rs}(488)/ R_{rs}(547)$ x-axis plotted against the NN retrieval of $a_g(442)$ m^{-1}. The relationship between these two parameters is strong as the CDOM absorption dominates the blue part of the spectrum.

4.3 Summary

We have developed three neural networks, working in parallel, to model the inverse problem and retrieve 4 components of the water body; the particulate backscattering coefficient, as well as the algal, non-algal particulate and dissolved absorption coefficients at 442nm. We successfully retrieve these parameters in our simulated dataset, and further validated the algorithm with the NOMAD and our field dataset. Very reasonable values were also retrieved from satellite images.

The NN algorithm developed is accurate, fast, and insensitive to reasonable noise levels. It is easy to implement and yields accurate retrieval for each parameter for all reasonable R_{rs} inputs through a single set (i.e. global) of numerically evaluated NN parameters. This makes the NN algorithm ideal not only for scientists, but also for coastal management to implement on field data and satellite images. The NN algorithm was primarily designed here for use with the MODIS sensor, but it is not restricted to the exact bands used, as can be seen from the application to the NOMAD dataset where large quantity of data was interpolated between the 510nm and the 547nm channels to model measurements at 531nm. The NN algorithm, using these coefficients should be sufficiently effective for use with the existing datasets of the Sea-viewing Wide Field-of-view Sensor (SeaWiFS) as well as for the future mission Visible Infrared Imager Radiometer Suite (VIIRS) since the 531nm channel can be modeled using the 510nm and 555nm channels for the first sensor, and the 488nm and 555nm channels for the second.

Chapter 5 How well do the empirical relationships describe the IOPs?

5.1 Predicting the Absorption at multispectral Visible Bands

5.1.1 Empirical relationships for algal, non-algal particulate, and CDOM absorptions

Estimating the algal, non-algal particulate and CDOM absorption coefficients at all visible wavelengths is important since these values can be used to estimate important physiological processes from remote measurements, as described in *IOCCG Report 7* [2008]. In this chapter we examine whether the empirical relationships used to describe the three main natural water absorbing components are adequate for estimating these absorptions over the range of visible wavelengths. We also introduce, a simple empirical model to estimate the absorption of phytoplankton at other MODIS bands, based on parameterization of the NOMAD dataset [*Werdell and Bailey*, 2005]. And, finally using this empirical model, we analytically estimate the size parameter, S_f, [*Ciotti et al.*, 2002], and the [*Chl*].

The absorptions of CDOM and NAP can be modeled by exponential decaying functions, extrapolated over all visible wavelengths using the average functional shapes derived in *Babin et al.* [2003]. Both these functional shapes can be represented by commonly used exponential decaying functions. Thus, CDOM absorption is,

$$a_g(\lambda) = a_g(442) \times \exp[0.0176 \times (442 - \lambda)] \quad m^{-1} \tag{5.1}$$

and the NAP absorption is,

$$a_{dm}(\lambda) = a_{dm}(442) \times \exp[0.0123 \times (442 - \lambda)] \quad m^{-1} \tag{5.2}$$

As can be seen in Figures 4 and 14 in *Babin et al.* [2003], the resulting constant average slopes don't play a significant role in the estimation of the absorption at different wavelengths. For the phytoplankton absorption, we can independently adopt the two shapes for micro- and pico-plankton used in our simulations [*Ciotti et al.*, 2002]. This should permit a better judgment to be made of whether these functional shapes can predict the absorption of phytoplankton at other wavelengths. The assumed functional shapes for phytoplankton absorption are shown in Figure 5.1 along with the other functional shapes assumed for the non-algal constituent absorptions [*Babin et al.*, 2003], all normalized at 442nm.

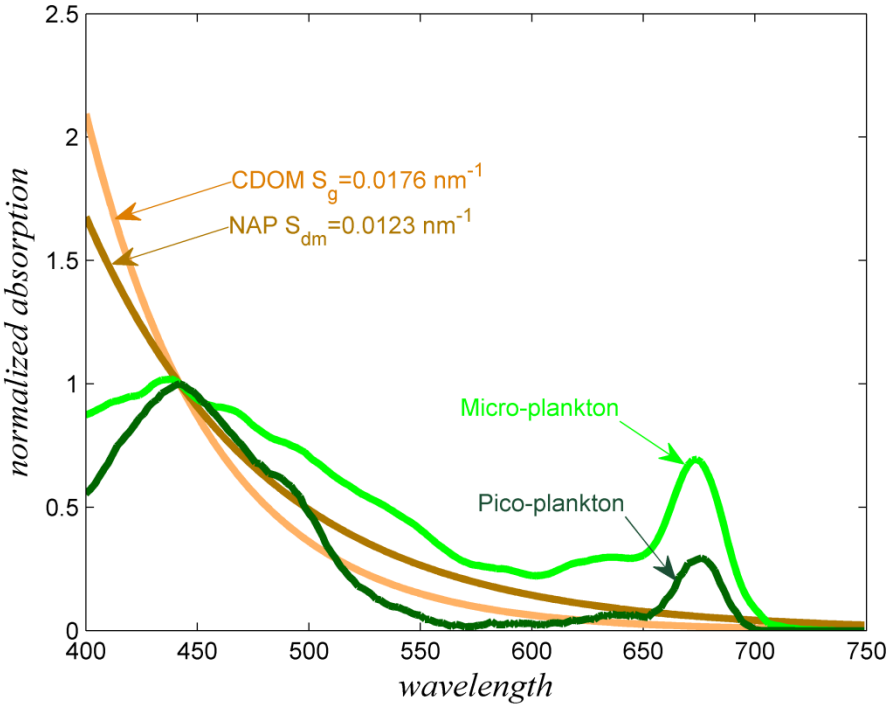

Fig. 5.1. Phytoplankton, CDOM and NAP absorptions used in this chapter to predict the absorption of these three components at other wavelengths. All functions are

normalized at 442 nm (in conformity with the outputs of the NN algorithm; Chapter 3 Section 3.3).

5.1.2 Estimating the absorption at MODIS bands

Using the above mentioned absorption functional shapes and the retrieved parameters from the neural network algorithm at 442 nm, as described in Chapter 3 section 3.3, we predict the absorption due to these components at other visible wavelengths. We then compare the absorption of each retrieved parameter with the one measured from the NOMAD dataset at 412, 488, 547 and 667 nm [*Werdell and Bailey*, 2005].

The predicted absorption values are plotted against the measured parameters for the total absorption, algal absorption, non- algal particulate and dissolved absorption coefficient at 412nm in Figure 5.2, and the corresponding retrieval statistics are shown in Table 5.1. As can be seen, the non-algal parameters can be predicted reasonably well at 412nm using the average functional shapes Eq. (5.1) and Eq. (5.2) and no significant difference in the prediction of the algal absorption and total absorption coefficient is observed between the two functional shapes of micro- and pico-plankton [*Ciotti et al.*, 2002]. These same functional shapes can also predict reasonably well the absorptions at 488 nm. Again, no significant difference in the prediction of the algal absorption and total absorption coefficient is observed for the two shapes of micro- and pico-plankton in Figure 5.3 and Table 5.2.

Although the functional shapes appear to predict reasonably well absorptions of the non-algal particulate and dissolve absorption at the 547 and 667nm, the phytoplankton absorption indicates a change in the relationship between the 442 nm

band and the 547 and 667nm bands, which translates to overestimation/underestimation of both the phytoplankton absorption and the total absorption coefficient, at these wavelengths. Significant difference in the prediction of the algal absorption coefficient is observed for the two functional shapes of micro- and pico-plankton. The pico-plankton functional absorption shape seems to better describe low phytoplankton absorptions, whereas the micro-plankton function better describe the higher phytoplankton absorptions. This is understandable if, as is commonly believed, low phytoplankton absorbing waters are populated primarily by pico- plankton, and the high phytoplankton absorbing waters are populated primarily by micro-plankton. This is supported by both theoretical [*Morel and Bricaud*, 1981; *Kirk*, 1994] and experimental [*Sosik and Mitchell*, 1991; *Bricaud et al.*, 1995; *Stuart et al.*, 1998] work of studies that indicate that the chlorophyll-a specific absorption coefficient of phytoplankton, is affected by cell size. Figure 5.4 and Figure 5.5 support these previous results.

Figure 5.4 and Figure 5.5 along with Table 5.3 and Table 5.4 also illustrate with what accuracy the non-algal particulate and dissolved absorptions coefficients can be estimated at longer wavelengths.

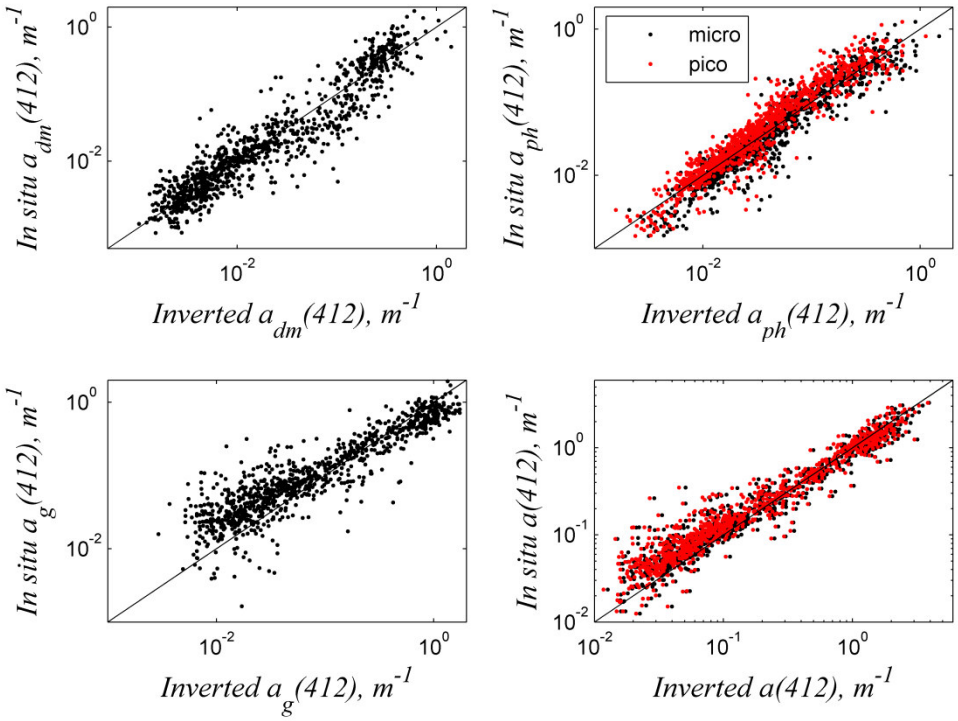

Fig. 5.2. Inverted IOP's (x-axis) plotted against the in situ values from the NOMAD dataset for $a_{dm}(412)$ m^{-1}, a_{ph} (412) m^{-1}, a_g (412) m^{-1} and $a(412)$ m^{-1}. The parameters are extrapolated to 412 nm from the neural network retrieved parameters at 442 nm and the empirical functional shapes discussed in this chapter.

Table 5.1. Statistics for Figure 5.2. Units in m^{-1}.

	$\alpha(412)$ *(pico)*	$\alpha(412)$ *(micro)*	$\alpha_{ph}(412)$ *(pico)*	$\alpha_{ph}(412)$ *(micro)*	$\alpha_{dm}(412)$	$\alpha_g(412)$
R^2	0.93	0.932	0.901	0.901	0.879	0.821
slope	0.84	0.85	1.040	1.040	0.962	0.719
intercept	-0.03	-0.052	0.131	0.004	-0.072	-0.19
$RMSE_{log10}$	0.204	0.185	0.202	0.196	0.273	0.331
e	0.6	0.53	0.593	0.569	0.873	1.142
N	929	929	1031	1031	1032	977

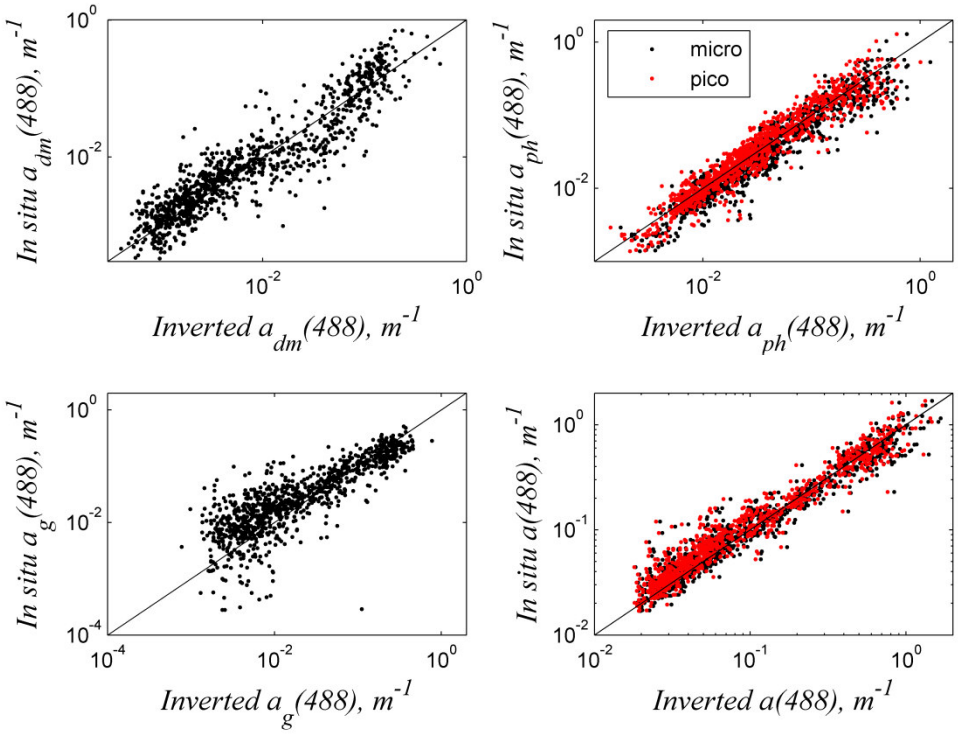

Fig. 5.3. Inverted IOP's (x-axis) plotted against the in situ values from the NOMAD dataset for $a_{dm}(488)$ m^{-1}, a_{ph} (488) m^{-1}, a_g (488) m^{-1} and $a(488)$ m^{-1}. The parameters are extrapolated to 488nm from the neural network retrieved parameters at 442nm and the empirical functional shapes described in this chapter.

Table 5.2. Statistics for Figure 5.3. Units in m^{-1}.

	α(488) (pico)	*α(488) (micro)*	$\alpha_{ph}(488)$ *(pico)*	$\alpha_{ph}(488)$ *(micro)*	$\alpha_{dm}(488)$	$\alpha_g(488)$
R^2	0.938	0.939	0.905	0.905	0.857	0.700
slope	0.9	0.897	0.984	0.984	0.929	0.323
intercept	-0.046	-0.082	-0.019	-0.11	-0.119	-0.3
$RMSE_{log10}$	0.139	0.129	0.173	0.193	0.294	0.409
e	0.378	0.344	0.489	0.56	0.968	1.563
N	935	935	1031	1031	1038	977

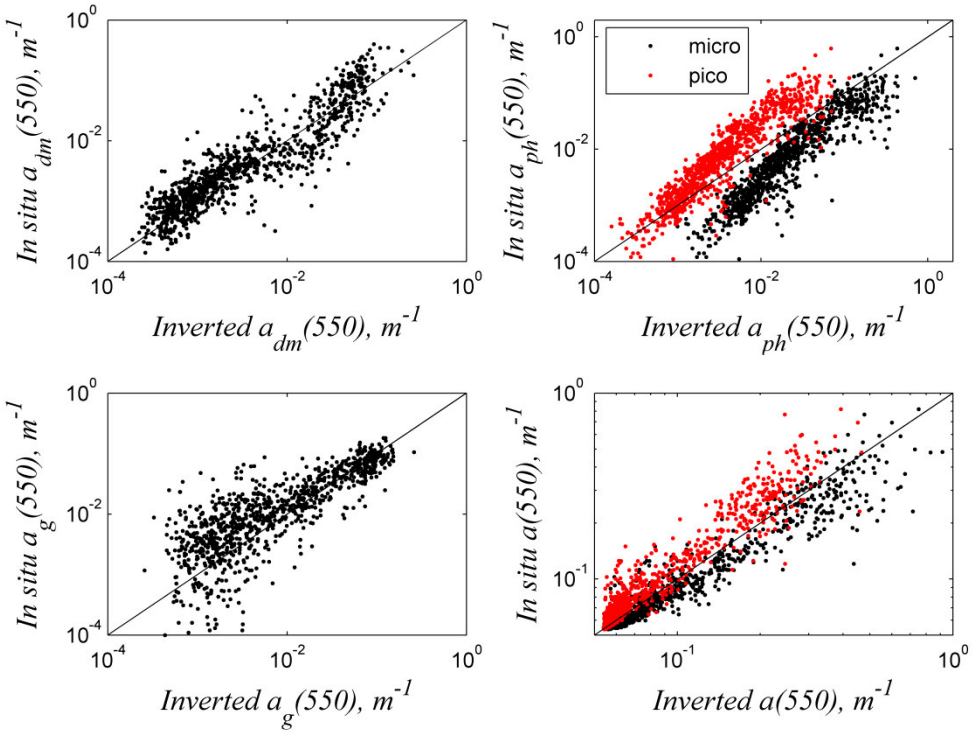

Fig. 5.4. Inverted IOP's (x-axis) plotted against the in situ values from the NOMAD dataset for $a_{dm}(547)$ m^{-1}, a_{ph} (547) m^{-1}, a_g (547) m^{-1} and $a(547)$ m^{-1}. The parameters are extrapolated to 547nm from the neural network retrieved parameters at 442nm and the empirical shapes described in this chapter. Evidently there is a considerable difference in the estimates of the algal absorption at this wavelength for the two functional shapes. Clearly the optimum functional shape lies between that for each of the species.

Table 5.3. Statistics for Figure 5.4. Units in m^{-1}.

	$\alpha(547)$ (pico)	$\alpha(547)$ (micro)	$\alpha_{ph}(547)$ (pico)	$\alpha_{ph}(547)$ (micro)	$\alpha_{dm}(547)$	$\alpha_g(547)$
R^2	0.92	0.918	0.855	0.855	0.8315	0.594
slope	1.1093	0.871	1.217	1.217	0.9105	0.331
intercept	0.1861	-0.165	0.834	-0.13	-0.1456	-0.36
$RMSE_{log10}$	0.105	0.094	0.423	0.574	0.3267	0.5
e	0.273	0.241	1.647	2.746	1.1217	2.16
N	927	927	1031	1031	1028	977

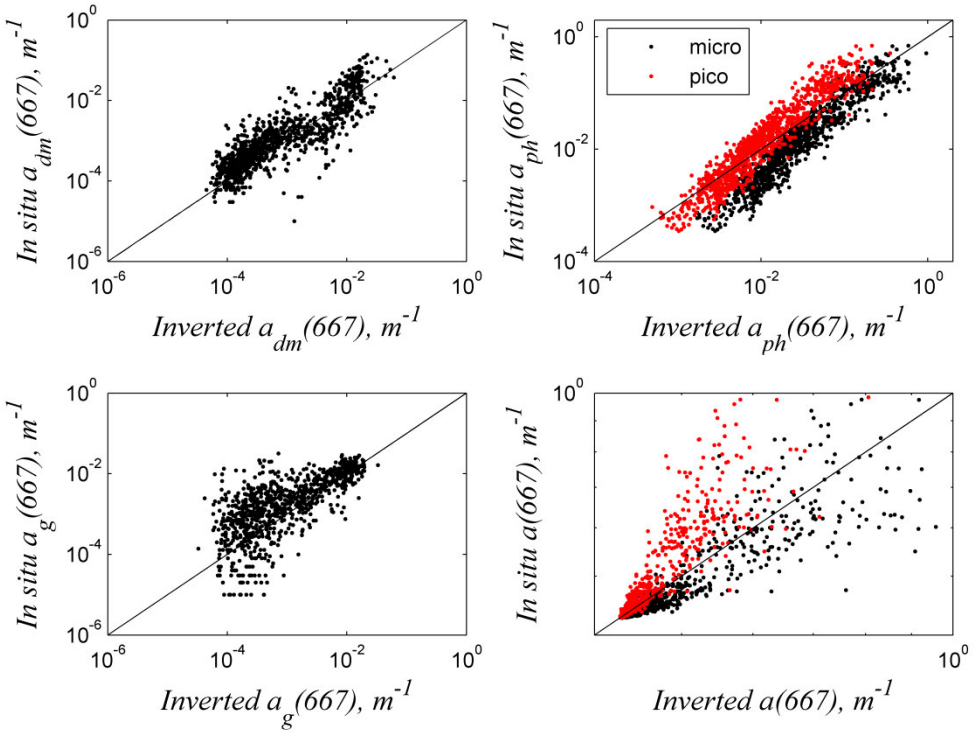

Fig. 5.5. Inverted IOP's (x-axis) plotted against the in situ values from the NOMAD dataset for $a_{dm}(667)$ m^{-1}, a_{ph} (667) m^{-1}, a_g (667) m^{-1} and $a(667)$ m^{-1}. The parameters are extrapolated to 667nm from the neural network retrieved parameters at 442nm and the empirical functional shapes described in this chapter. Evidently there is a considerable difference in estimates of the algal absorption at this wavelength between the functional two shapes.

Table 5.4. Statistics for Figure 5.5. Units in m^{-1}.

	a(667) (pico)	*α(667) (micro)*	$\alpha_{ph}(667)$ *(pico)*	$\alpha_{ph}(667)$ *(micro)*	$\alpha_{dm}(667)$	$\alpha_g(667)$
R^2	0.804	0.8	0.903	0.903	0.7410	0.49
slope	1.6489	0.8277	1.244	1.244	0.8648	0.32
intercept	0.2422	-0.0653	0.581	0.04	-0.2572	-0.53
$RMSE_{log10}$	0.0473	0.0380	0.276	0.423	0.4301	0.617
e	0.1150	0.0915	0.888	1.6500	1.6922	3.139
N	935	935	1031	1031	1038	977

5.2 Parameterization of the algal normalized specific absorption

5.2.1 Parameterization for multispectral satellite bands

Clearly each of the functional empirical shapes alone cannot be used to estimate the phytoplankton absorption over all absorbing ranges, especially at longer wavelengths (i.e. 547 and 667nm). To address this issue we introduce here a way to estimate the phytoplankton absorption at 412, 442, 488, 550 and 667 nm as a function of the algal absorption coefficient at 442nm. We first define a new normalized (at 442nm) specific functional absorption shape that will be a function of the algal absorption coefficient at 442nm. This is similar to the work of *Bricaud et al.* [1995] with the difference being that instead of modeling the algal absorption as a function of [*Chl*] we parameterize it as a function of $a_{ph}(442)$ analogous to *Lee* [1994]. This is primarily done because our retrieval (neural network) is the algal absorption at 442nm, therefore we need an empirical representation (as a function $a_{ph}(442)$) to model the absorption of phytoplankton at longer wavelengths, since the [*Chl*] isn't *a' priori* known. Using the available NOMAD dataset [*Werdell and Bailey*, 2005] measurements we obtain a relationship of the measured algal absorptions at each of these wavelengths normalized to the algal absorption at 442nm as a function of the algal absorption at 442nm. In this way the normalized specific absorption will change as a function of the retrieved algal absorption coefficient at 442nm. The normalized specific absorption coefficient is given next for each of the 5 wavelengths, 412, 488, 547, and 667 nm. At 442 nm it is clearly equal to 1. The normalized algal absorption at the 5 wavelengths was found to be:

$$\frac{a_{ph}(412)}{a_{ph}(442)} = 0.881 \times \{a_{ph}(442)\}^{0.0275} \tag{5.3}$$

$$\frac{a_{ph}(442)}{a_{ph}(442)} = 1, \tag{5.4}$$

$$\frac{a_{ph}(488)}{a_{ph}(442)} = 0.6898 \times \{a_{ph}(442)\}^{0.0231} \tag{5.5}$$

$$\frac{a_{ph}(550)}{a_{ph}(442)} = 0.2601 \times \{a_{ph}(442)\}^{0.2061} \tag{5.6}$$

$$\frac{a_{ph}(667)}{a_{ph}(442)} = 0.4388 \times \{a_{ph}(442)\}^{0.1583} \tag{5.7}$$

The way in which specific absorption (normalized at 442 nm) is changing as a function of wavelength is shown in Figure 5.6. While Figure 5.7 illustrates the dependence of this normalized specific absorption with $a_{ph}(442)$ for each wavelength. The absorption of micro- and pico-plankton [*Ciotti et al.*, 2002] is also shown normalized at 442 nm in Figure 5.6 for comparison. Clearly the range of variability falls very well within the absorption of these two species.

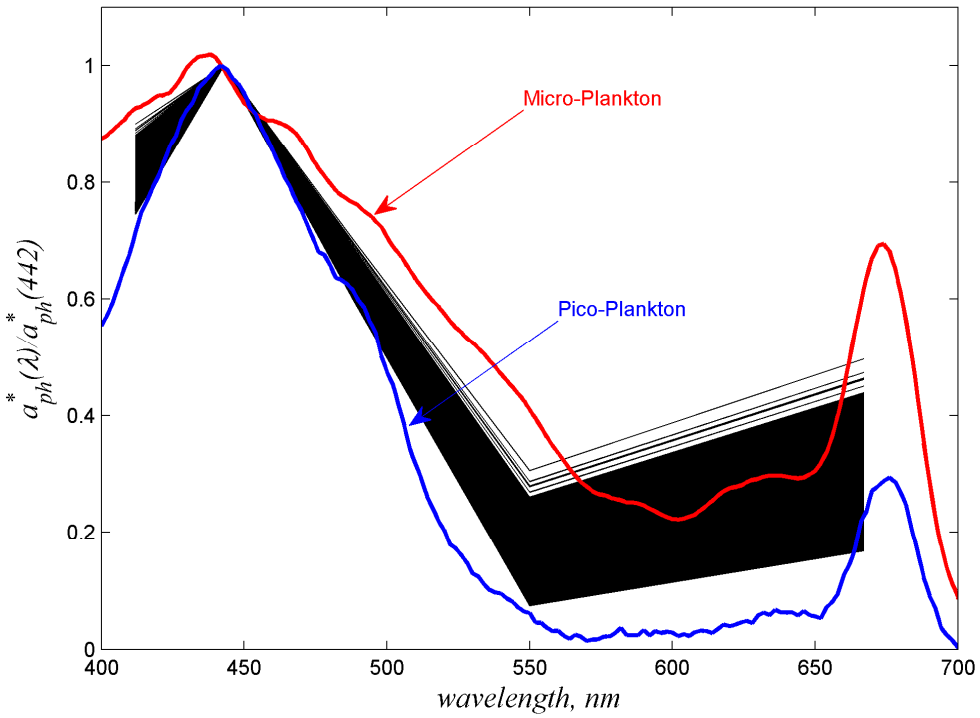

Fig. 5.6. Algal absorption normalized at 442 nm (normalized specific absorption) as a function of wavelength for all available NOMAD data. The normalized at 442nm absorption of micro- and pico- plankton are also shown. This is the expected range of change of the normalized specific algal absorption. The black lines represent the NOMAD dataset measurement at 442nm and are extrapolated to the other wavelengths using the parameterization from Eqs. (5.3)-(5.7). Also see Figure 5.7.

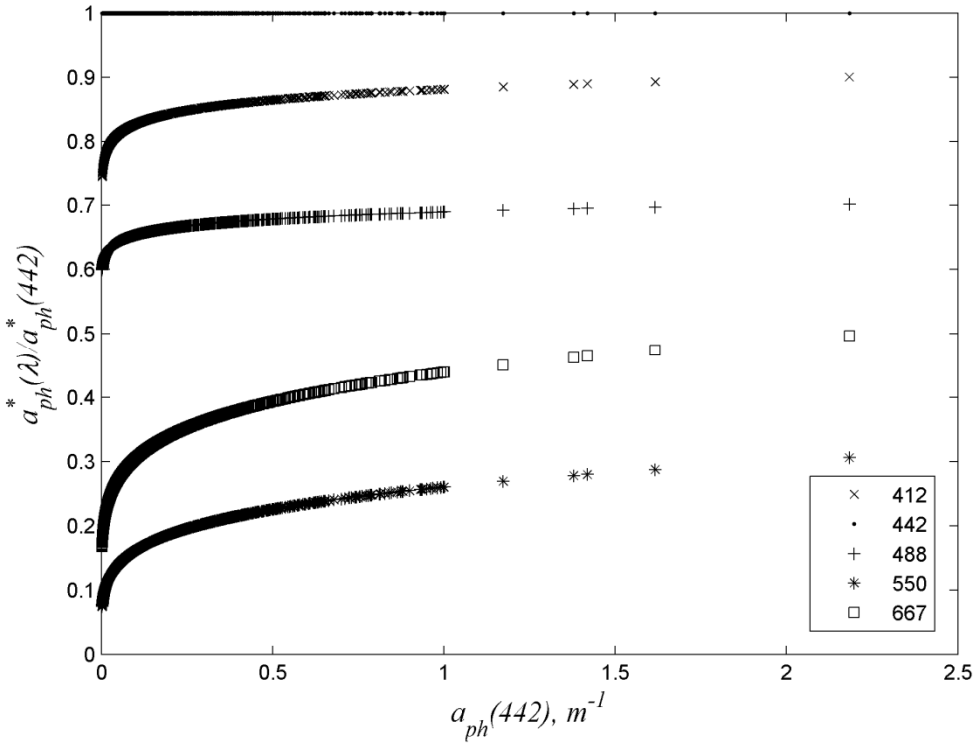

Fig. 5.7. Specific absorption of algae normalized at 442nm (y-axis) as a function of $a_{ph}(442)$ m^{-1} , Eqs. (5.3) - (5.7). The $a_{ph}(442)$ m^{-1} is the measurement from the NOMAD dataset.

How well these relationships describe the extrapolation of the algal absorption at these additional 4 visible wavelengths is shown in Figure 5.8 and the accuracies with which they are retrieved are shown in Table 5.5. The predictions for total absorption were also improved as can be seen in Figure 5.9 and in the statistics shown in Table 5.6. These results show that with our modeling we can predict the algal absorption at all MODIS wavelengths very well.

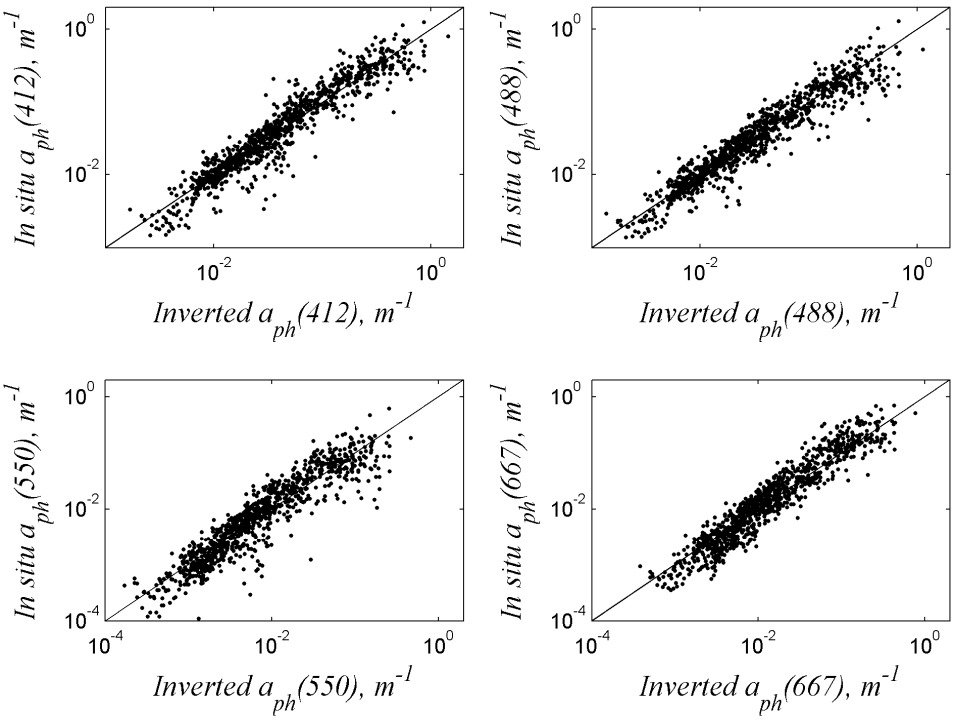

Fig. 5.8. Predicted algal absorption at 412, 488, 547 and 667 nm using the modeling of $a_{ph}(442)$ m^{-1} described in Eq. (5.3), Eq. (5.5), Eq. (5.6) and Eq. (5.7) and the retrieved $a_{ph}(442)$ m^{-1} from the neural network algorithm.

Table 5.5. Statistics for Figure 5.8. Units in m^{-1}.

	$\alpha_{ph}(412)$	$\alpha_{ph}(488)$	$\alpha_{ph}(547)$	$\alpha_{ph}(667)$
R^2	0.901	0.905	0.855	0.904
slope	1.013	0.961	1.009	1.074
intercept	-0.023	-0.067	0.023	0.141
$RMSE_{log10}$	0.188	0.174	0.273	0.226
e	0.541	0.493	0.874	0.682
N	1031	1037	1026	1030

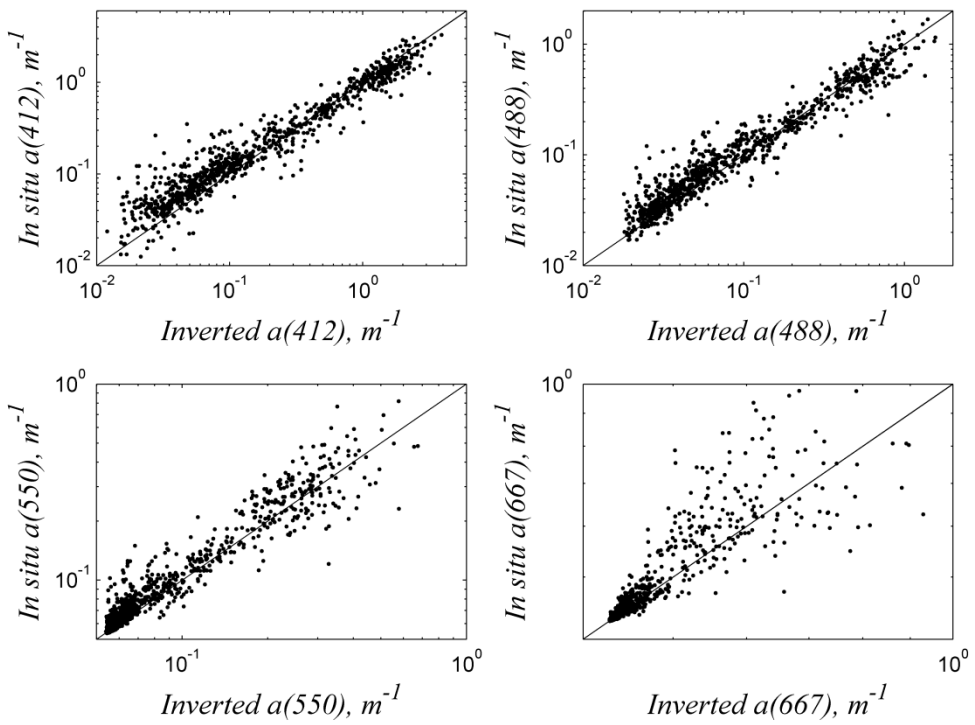

Fig. 5.9. Predicted total absorption at 412, 488, 547 and 667 nm using the modeling of $a_{ph}(442)$ m^{-1} described in Eq. (5.3), Eq. (5.5), Eq. (5.6) and Eq. (5.7) and the non-algal shapes described in Eq. (5.1) and Eq. (5.2) and the retrieved parameters of $a_g(442)$ m^{-1}, $a_{dm}(442)$ m^{-1} and $a_{ph}(442)$ m^{-1} from the neural network algorithm.

Table 5.6. Statistics for Figure 5.9. Units in m^{-1}.

	$\alpha(412)$	$\alpha(488)$	$\alpha(547)$	$\alpha(667)$
R^2	0.931	0.938	0.919	0.783
slope	0.84	0.892	0.96	1.05
intercept	-0.046	-0.061	-0.007	0.026
$RMSE_{log10}$	0.195	0.138	0.083	0.036
e	0.567	0.375	0.211	0.086
N	929	935	927	889

5.2.2 Solving for the size parameter, Sf and [Chl]

In the previous section we showed how well we can predict the absorption of retrieved parameters at longer wavelengths using empirical relationships. We primarily focused on the parameterization of the algal spectral absorption as a function of the retrieved absorption coefficient at 442 nm. As we observed in the previous section, the predicted absorption spectral shapes for the MODIS bands fall well within the measured absorption shapes for micro- and pico-plankton [*Ciotti et al.*, 2002], at least in the blue and green region.

Based on this observation, we use, in this section, one of the empirical relationships derived in the previously, Eq. (5.6) to predict the algal absorption at 547 nm given the retrieved absorption at 442 nm. We choose to use this derived relationship as this is where the maximum variability was observed in our parameterization. Knowing the absorption at these two wavelengths we can solve Eq. 5.8 below for the two unknown parameters, the size parameter, S_f (dimensionless) as described in *Ciotti et al.*[2002] and the chlorophyll concentration, [*Chl*] mg m^{-3},

$$a_{ph}(\lambda) = \{S_f \times a^*_{pico}(\lambda) + (1 - S_f) \times a^*_{micro}(\lambda)\} \times [Chl] \quad m^{-1} \tag{5.8}$$

the solution we obtain for S_f is,

$$S_f = \frac{a^*_{micro}(442) \times \dfrac{a_{ph}(550)}{a_{ph}(442)} - a^*_{micro}(550)}{a^*_{pico}(550) - a^*_{micro}(550) + a^*_{micro}(442) \times \dfrac{a_{ph}(550)}{a_{ph}(442)} - a^*_{pico}(442) \times \dfrac{a_{ph}(550)}{a_{ph}(442)}} \tag{5.9}$$

Where $\frac{a_{ph}(550)}{a_{ph}(442)}$ is approximated by Eq. (5.6), and reproducing here the results of *Ciotti et al.* [2002], interpolating from the available wavelengths, for the specific absorption of micro- and pico- plankton at the two wavelengths of interest,

$$\begin{aligned} a^*_{pico}(550) &= 0.005 \quad m^2 mg^{-1} \\ a^*_{pico}(442) &= 0.0783 \quad m^2 mg^{-1} \\ a^*_{micro}(550) &= 0.005 \quad m^2 mg^{-1} \\ a^*_{micro}(442) &= 0.0124 \quad m^2 mg^{-1} \end{aligned} \tag{5.10}$$

we obtain a numerical solution for the size parameter, S_f.

Knowing S_f from Eq. (5.9) and $a_{ph}(442)$ m^{-1} from the neural network inversion we can easily solve Eq. (5.8) for the [*Chl*] mg m^{-3},

$$[Chl] = \frac{a_{ph}(442)}{\{S_f \times a^*_{pico}(442) + (1 - S_f) \times a^*_{micro}(442)\}} \quad mg \quad m^{-3} \tag{5.11}$$

It should be remembered the size parameter, S_f , and the [*Chl*] mg m^{-3} product (Eq.(5.10) and Eq. (5.11)) depend on the retrievals of the neural network ($a_{ph}(442)$) and the empirical relationship between $a_{ph}(442)$ and $a_{ph}(547)$ that was derived earlier in this chapter. Using this relationship and the independent modeling of the micro- and pico-plankton absorptions shapes from *Ciotti et al.* [2002] we obtain a solution for Eq. 5.8 for these parameters. In Figure 5.10 we show the relationship of the size parameter, S_f, with the phytoplankton absorption at 442 nm, $a_{ph}(442)$, and the calculated [*Chl*] mg m^{-3} (Eq 5.11) in both the linear and logarithmic domain. Using this calculated size parameter, S_f, we can also produce a normalized at 442 nm specific absorption at all visible wavelengths (400-700 nm). We can then, in a similar manner to the one

followed in the previous section, predict the absorption at the 4 additional MODIS bands (412, 488, 547 and 667 nm) and compare them with the measured spectra of both phytoplankton and total absorption coefficients at these wavelengths. The relationship between the measured and estimated phytoplankton absorption is very similar to the one obtained in the previous section as can be seen in Figure 5.11 and in the statistics, Table 5.7. The results for the total absorption coefficient are also very similar to the previous modeling (section 5.3.1), as can be seen in Table 5.8 and in Figure 5.12. The benefit of this method is that we can predict the absorption using the size parameter at all visible wavelengths and also obtain an estimate of the [*Chl*] mg m^{-3} using modeled absorptions of the micro- and pico- plankton. For the [*Chl*] obtained in Eq. 5.11 to be valid for [*Chl*] < 1 mg m^{-3} the retrieved parameter needs to be adjusted with the 0.626 exponent used in our modeling, or,

$$[Chl] = \begin{Bmatrix} [Chl]^{\frac{1}{0.626}}, [Chl] < 1 mg/m^{-3} \\ [Chl] \quad\quad , [Chl] > 1 mg/m^{-3} \end{Bmatrix} mg/m^{-3} \tag{5.12}$$

The reason for the 0.626 exponent is to model higher specific algal absorptions that cannot be represented by the *Ciotti et al.* [2002] modeling as the maximum specific absorption that can be modeled with the pico- plankton at 442nm is 0.0783 m^2 mg^{-1}. Reported specific absorptions at this wavelength can reach values as high as 0.17 or higher [*Bricaud et al.*, 1995]. These specific absorptions are probably due to the effect of accessory pigments that become prominent in the low [*Chl*] mg m^{-3} waters.

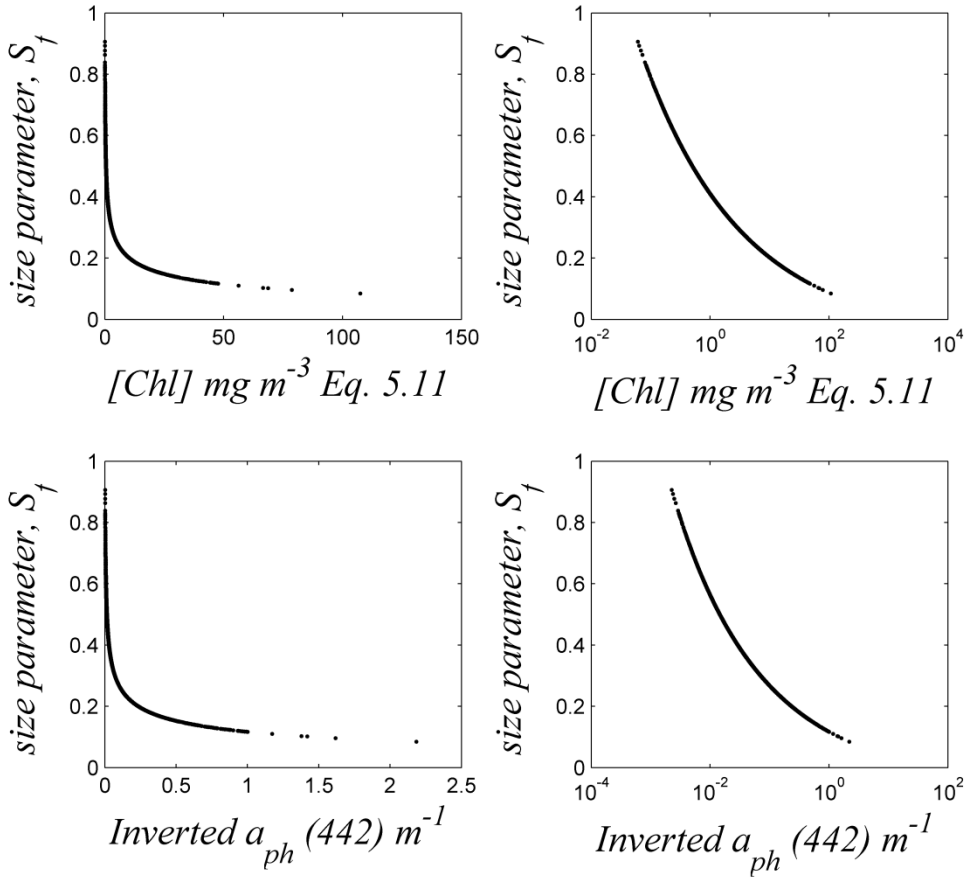

Fig. 5.10. Relationship of the size parameter, S_f (Eq. 5.9), and [*Chl*] mg m^{-3} (Eq 5.11) (upper figures) and $a_{ph}(442)$ m^{-1} (lower figures) in both the linear (left) and logarithmic domain (right). The size parameter is reduced as a function of these two parameters in agreement with previous studies [*Morel,* 1991; *Bricaud et al.*, 1995].

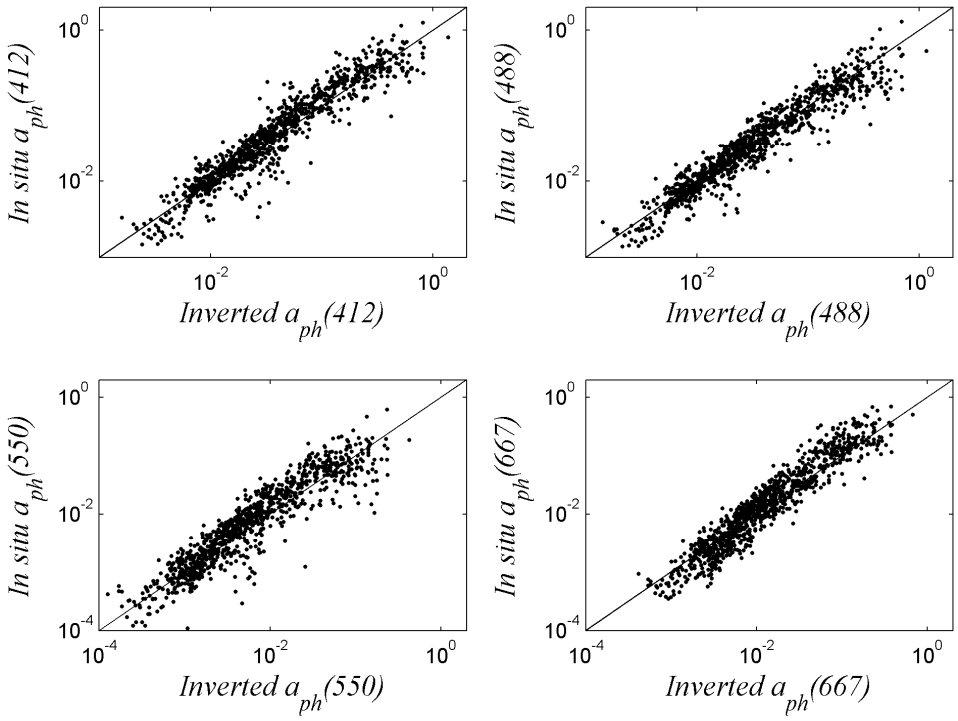

Fig. 5.11. Predicted algal absorption at 412, 488, 547 and 667 nm from Eq. (5.9) and the retrieved $a_{ph}(442)$ m^{-1} from the neural network algorithm.

Table 5.7. Statistics for Figure 5.11. Units in m^{-1}.

	$\alpha_{ph}(412)$	$\alpha_{ph}(488)$	$\alpha_{ph}(547)$	$\alpha_{ph}(667)$
R^2	0.9005	0.905	0.855	0.902
slope	1.0125	0.964	0.985	1.104
intercept	0.0579	-0.071	0.039	0.227
$RMSE_{log10}$	0.1923	0.175	0.282	0.233
e	0.5571	0.496	0.913	0.708
N	1031	1037	1026	1030

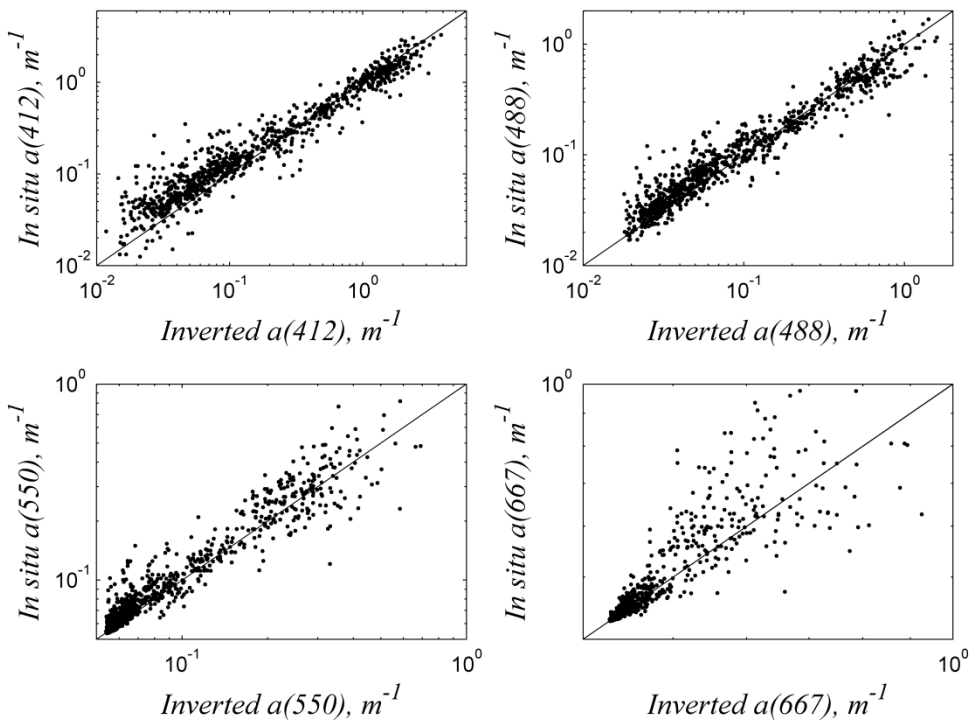

Fig. 5.12. Predicted total absorption at 412, 488, 547 and 667 nm using the modeling of $a_{ph}(442)$ m^{-1} described in Eq. (5.9) and the non-algal shapes described in Eq. (5.1) and Eq. (5.2) and the retrieved parameters of $a_g(442)$ m^{-1}, $a_{dm}(442)$ m^{-1} and $a_{ph}(442)$ m^{-1} from the neural network algorithm.

Table 5.8. Statistics for Figure 5.12. Units in m^{-1}.

	$\alpha(412)$	$\alpha(488)$	$\alpha(547)$	$\alpha(667)$
R^2	0.931	0.938	0.92	0.7865
slope	0.838	0.892	0.96	1.05
intercept	-0.04	-0.063	-0.013	0.025
$RMSE_{log10}$	0.2	0.137	0.083	0.0353
e	0.587	0.371	0.21	0.0848
N	929	935	927	889

5.3 Implementation of the model on MODIS data

5.3.1 Comparing our results with the MODIS [Chl] product

In this section we explore the same MODIS image as discussed in section 4.2.2 to evaluate physical parameters that are based on the modeling approach described in this chapter for the [*Chl*] mg m^{-3}. In Figure 5.13 we present a [*Chl*] mg m^{-3} image from Eq. 5.11 adjusted using Eq. 5.12 for the [*Chl*]<1 mg m^{-3}. Figure 5.14 exemplifies the [*Chl*] mg m^{-3} product of the MODIS [*O'Reilly et al.*, 1998]. In the following, we perform an extensive analysis of the similarities and the differences of the two products. In Figure 5.15 we show the relationship of the two products which is, for the most part, similar. There is a significant difference between the two methods when the MODIS [*Chl*] mg m^{-3} estimate is greater than 5 mg m^{-3} as can be seen in Figure 5.15, where the two retrieved chlorophyll concentration estimates are plotted against each other. In the image of Figure 5.16 we show their percent differences,

$$\%Diff = \frac{[Chl]_{MODIS} - [Chl]_{S_f}}{[Chl]_{MODIS} + [Chl]_{S_f}} \times 200 \tag{5.13}$$

We deliberately removed the absolute values from Eq. 5.13 in order to show whether the MODIS [*Chl*] algorithm depicts a deficiency or overestimation.

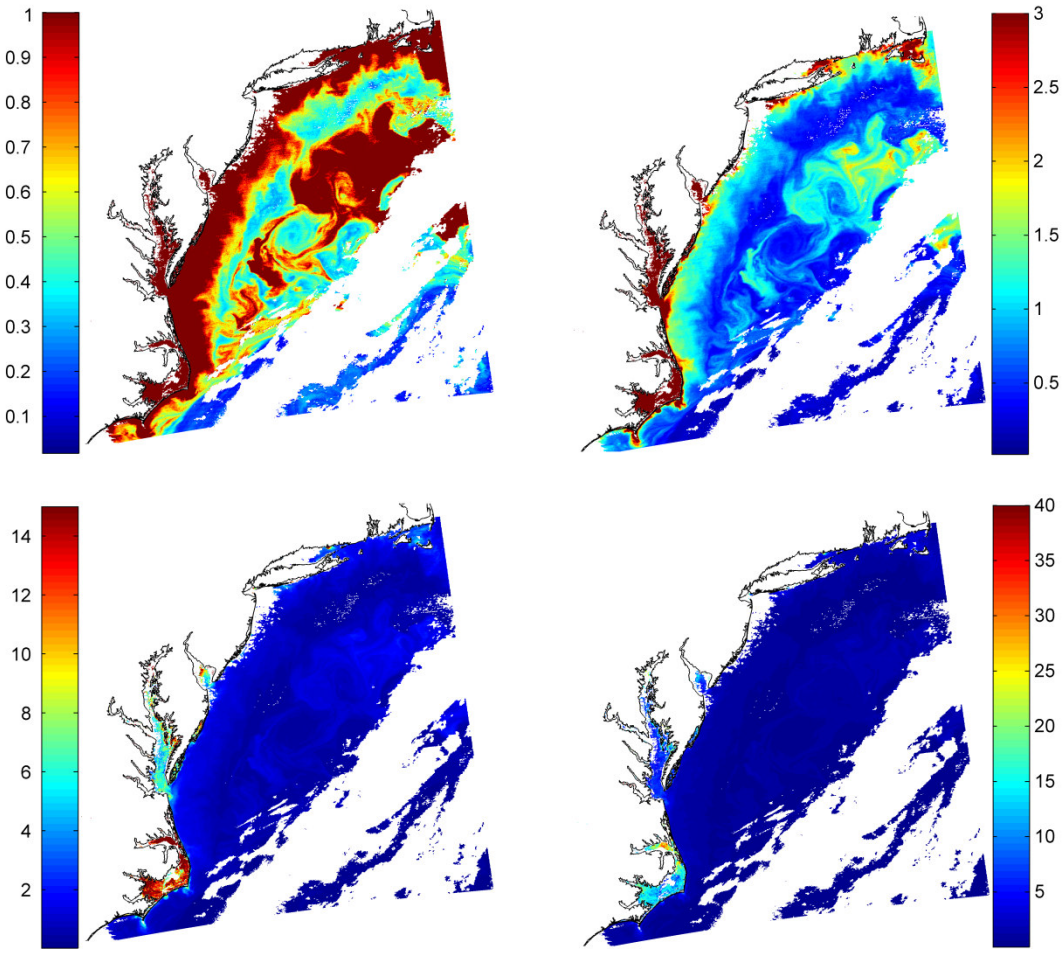

Fig. 5.13. Image of the [*Chl*] mg m^{-3} based on the size parameter, S_f, parameterization as described Eq. (5.11) and Eq.(5.12). The color bars next to each map indicate the range of [*Chl*] mg m^{-3}.

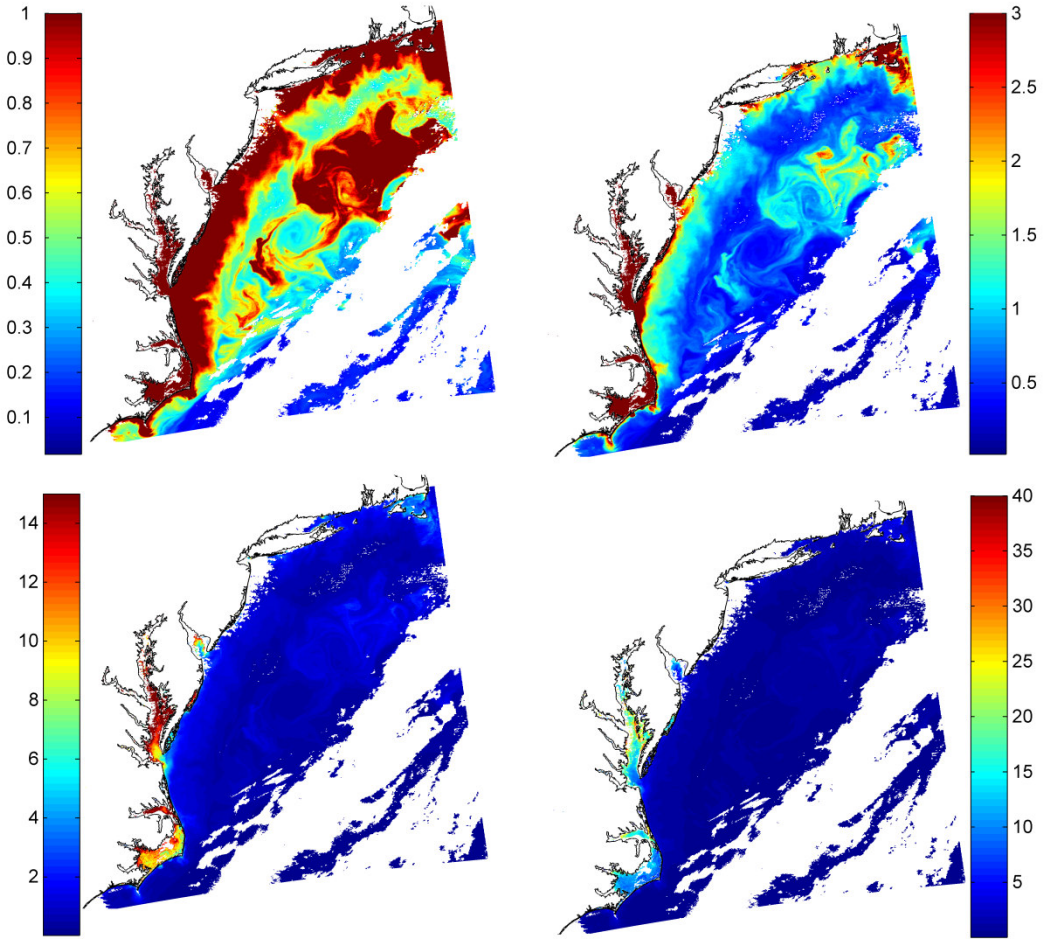

Fig. 5.14. Image of the MODIS [*Chl*] mg m^{-3} product [*O'Reilly et al.*, 1998]. The color bars next to each map indicate the range of [*Chl*] mg m^{-3}.

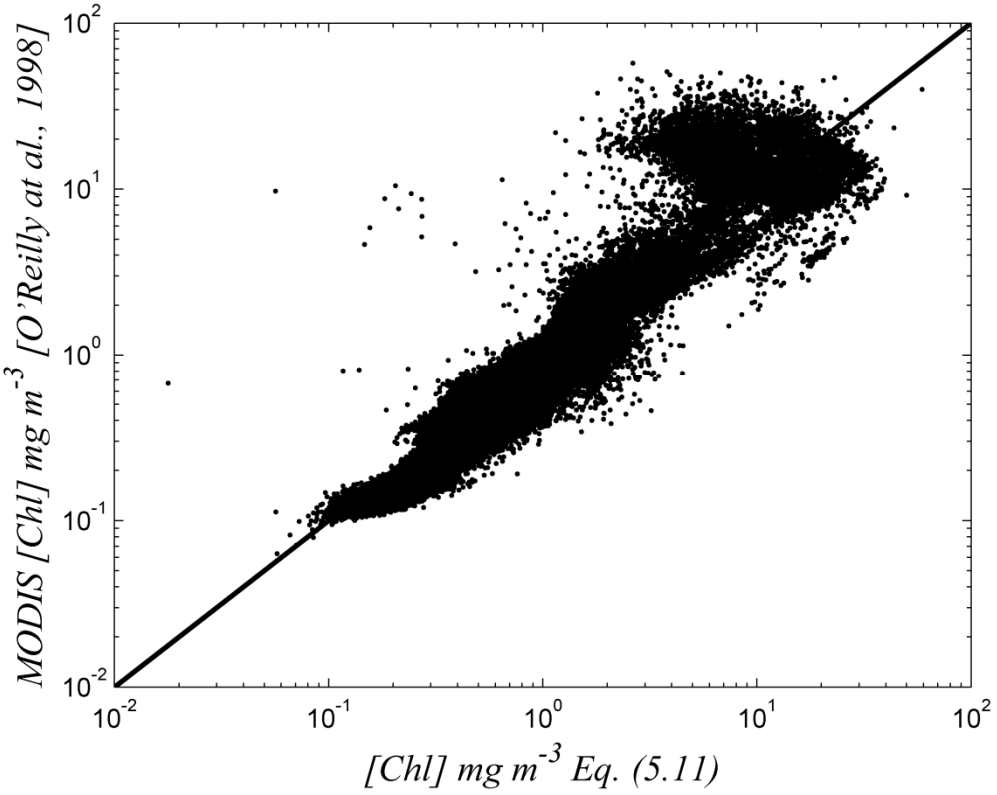

Fig. 5.15. The [*Chl*] mg m^{-3} based on the size parameter, S_f, parameterization as described in Eq. (5.11) and Eq. (5.12) vs. the MODIS [*Chl*] mg m^{-3} product (y-axis).

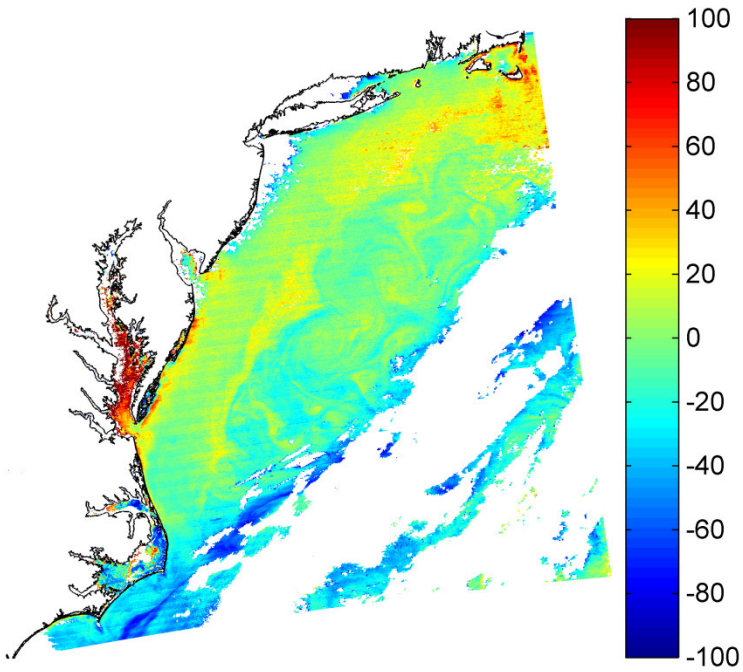

Fig. 5.16. Percent Difference Eq. (5.13) of the derived [*Chl*] mg m^{-3} using the size parameter, S_f and the MODIS [*Chl*] mg m^{-3} product as shown in Eq. (5.12).

5.3.2 Exploring the influence of the non- algal components on the MODIS [Chl] product

To observe whether the underestimation (or overestimation) that the MODIS [*Chl*] mg m^{-3} product exhibits [*O'Reilly et al.*, 1998] when compared to our product, we compare the percent difference from Eq. 5.13 with the ratio $a_{dm}(442)$ m^{-1} /$a_g(442)$ m^{-1}. This ratio is simply the output of the third neural network in our algorithm (see Chapter 3). This relationship is shown in Figure 5.17 in the logarithmic domain. As we expect positive values (overestimations of the MODIS [*Chl*] mg m^{-3} product) of Eq. 5.13 appear mostly when the ratio between the two substances is low (relatively high $a_g(442)$ contribution to the signal) due to the strong absorption behavior of these substances. Negative values of Eq. 5.13 appear primarily when the same ratio ($a_{dm}(442)$ m^{-1}/ $a_g(442)$) is high, which means increased contribution of $a_{dm}(442)$ and furthermore strong presence of non-algal particulates. The increased a_{dm} contribution translates to an increase of the blue channels intensity since the non-algal particulates mostly exhibit a steeper scattering slope that decrease as a function of wavelength. Raised blue channels force the blue green ratio algorithm [*O'Reilly et al.*, 1998] to generally underestimate the [*Chl*] mg m^{-3}.

The ratio $a_{ph}(442)$ m^{-1} /$a_g(442)$ m^{-1} shown in Figure 5.18 depicts the strong influence that the CDOM absorption has to the underestimation/overestimation of the blue/green ratio algorithm [*O'Reilly et al.*, 1998]. Again low $a_{ph}(442)$ m^{-1} /$a_g(442)$ m^{-1} indicate the strong presence of CDOM. On the other hand the ratio $a_{ph}(442)$ m^{-1} /$a_{dm}(442)$ m^{-1} shown in Figure 5.19 doesn't exhibit and relationship with Eq. 5.13.

Of course there are cases where both algorithms agree (within 20-30%) and where the blue/green ratio algorithm [*O'Reilly et al.*, 1998] is valid. This can be seen in Figures 5.16 - 5.19.

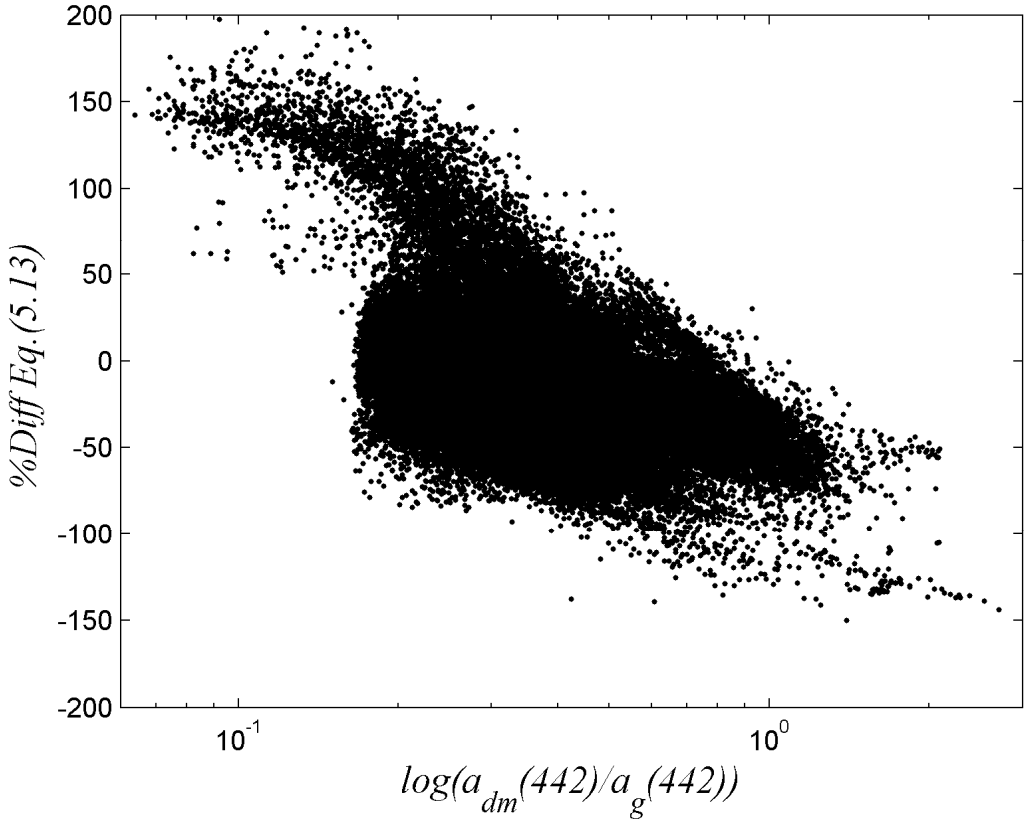

Fig. 5.17. Percent Difference Eq. 5.13 as a function of the log(a_{dm}(442) /a_g(442)). Clearly the underestimation/overestimation is a function of the contribution of the constituents other than phytoplankton.

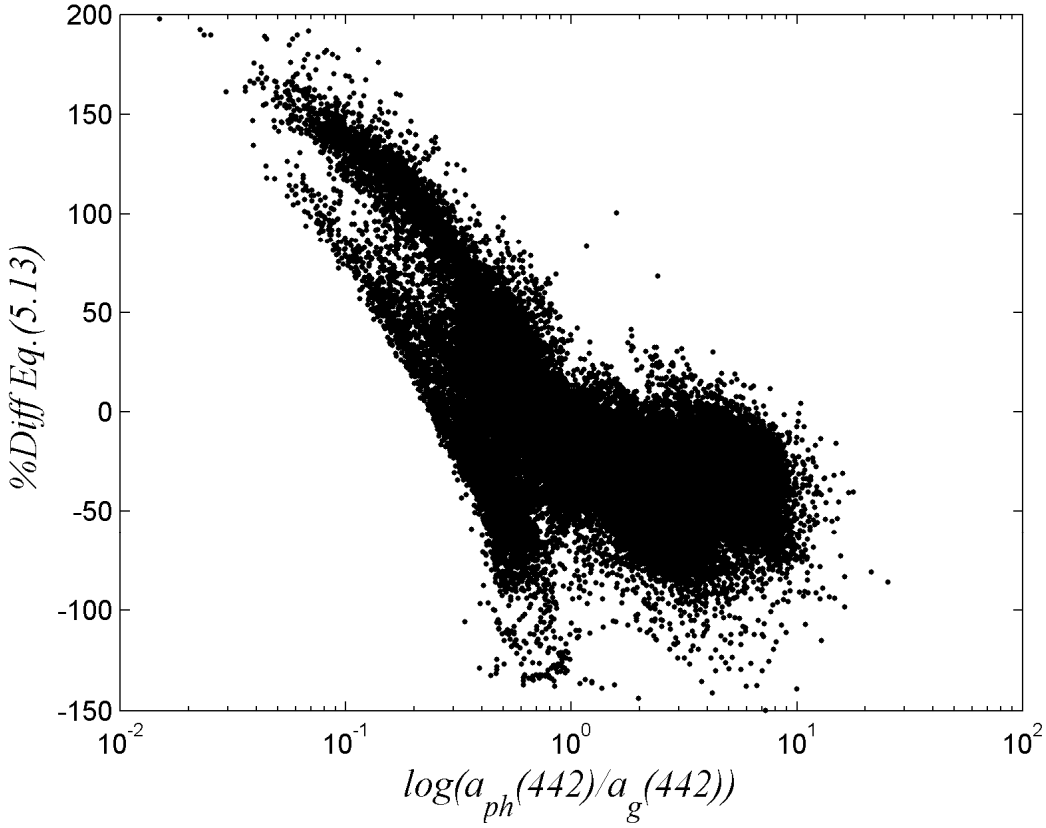

Fig. 5.18. Percent Difference Eq. 5.13 as a function of the log (a_{ph}(442) /a_g(442)). Clearly the underestimation/overestimation depends on the presence of CDOM.

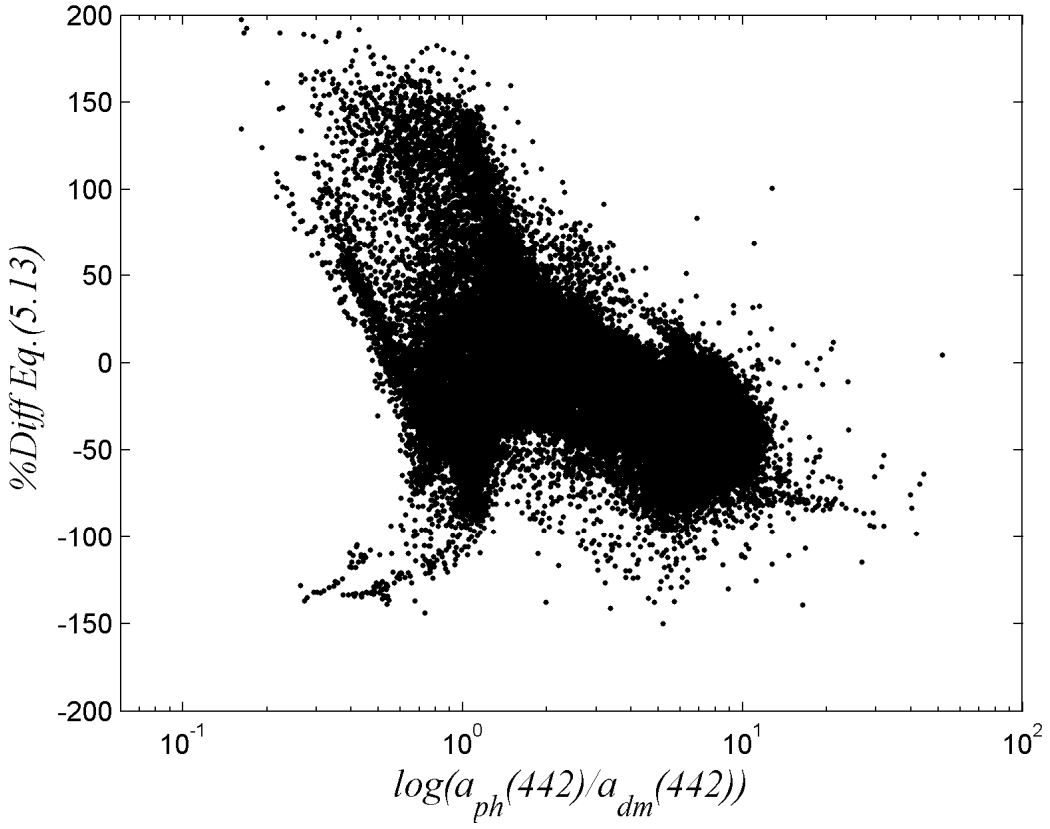

Fig. 5.19. Percent Difference Eq. 5.13 as a function of the log (a_{ph}(442) /a_{dm}(442)). There is no clear relationship that can explain the difference of the two algorithms by the non algal particulate absorptions.

5.5 Summary

In this chapter we introduced a way to extrapolate the absorption of the three primary constituents to the other MODIS wavelengths. We have shown that Eq. (5.1) and Eq. (5.2) *Babin et al.* [2003] can predict the absorption CDOM and NAP at these wavelengths relatively well. Although the algal absorption can be predicted satisfactory at the wavelengths around 442nm (412 and 488 nm) relatively well with both micro- and pico- plankton [*Ciotti et al.*, 2002], it cannot be retrieved at the longer wavelengths

(547 and 667 nm). The overestimation of the algal absorption at these longer wavelengths is a strong function of the algal absorption at 442nm where a retrieval using our neural network algorithm exists. Therefore we parameterize a normalized (at 442nm) algal specific absorption as a function of the retrieved algal absorption at 442nm. This relationship was empirically obtained using the NOMAD dataset [*Werdell and Bailey*, 2005] and is described in Eq. 5.3 through Eq. 5.7. This modeling can predict the algal absorption at other MODIS wavelengths very well as can be seen in Figure 5.8 and Table 5.4. Furthermore we used this empirical parameterization (Eq. 5.6) and our retrieval of $a_{ph}(442)$ m^{-1} to solve analytically for the size parameter, S_f, and the chlorophyll concentration [*Chl*] mg m^{-3} [*Ciotti et al.*, 2002]. Although the results of the solution using the size parameter are similar to the results obtain using the empirical parameterization, the benefit of this method is that we can obtain the algal absorption at all wavelengths (hypersectral) and most importantly we can obtain an estimate of the *Chl*] mg m^{-3}.

Chapter 6 Summary of the study

In this study we presented a neural network approach to relate the nadir-viewing spectral remote-sensing reflectance just above the surface, $R_{rs}(\lambda)$ sr^{-1}, (at the six visible MODIS bands), to two outputs the particulate and dissolved absorption coefficient, a_{pg}, and particulate backscattering coefficient, $b_{b\text{-}p}$, both at 442 nm. With two additional information, an estimate of the algal to non-algal absorption ratio, $R_{a_{dg}}^{a_{ph}}$ and an estimate of the non-algal particulate to dissolved absorption ratio, $R_{a_g}^{a_{dm}}$, both also at 442 nm we can analytically solve for the absorption magnitudes of each of the three major constituents a_{ph} , a_g and a_{dm} at 442nm. These two ratios are obtained from the same $R_{rs}(\lambda)$ measurement with neural network modeling.

After the successful training and validation of the neural network algorithm we can obtain 3 absorption amplitudes, the a_{ph}, a_g and a_{dm} at 442 nm. We then, using the NOMAD dataset [*Werdell and Bailey*, 2005], explored whether these three absorption values along with the average absorption functional shapes described in *Babin et al.* [2003] for the non-algal absorption components and micro- and pico- plankton [*Ciotti et al.*, 2002] absorption representations for the algal component, can be used to extrapolate the absorption of each parameter to the other MODIS visible bands. We have shown that although the average shape of the non-algal constituents a_g and a_{dm} [*Babin et al.*, 2003] can predict relatively well the absorption of these constituents at the MODIS bands (412, 443, 488, 547 and 667 nm) the micro- and pico- plankton [*Ciotti et al.*, 2002] absorption shapes give a very different result for the phytoplankton absorption in the longer 547 and 667nm wavelengths. To compensate for this

overestimation we then introduced a normalized (at 442 nm) phytoplankton absorption spectral shape at the same 5 MODIS bands. This modeling was obtain with parameterization of the NOMAD dataset [*Werdell and Bailey*, 2005] and provides the normalized phytoplankton absorption, a_{ph}, at each wavelength as a function of the phytoplankton absorption at 442 nm similar to the *Bricaud et al.*, [1995] with the difference of expressing the algal absorption shape as a function of $a_{ph}(442)$ instead of a function of [*Chl*] mg m^{-3}. We also observed that this new normalized algal shape falls within the micro- and pico- plankton normalized shapes [*Ciotti et al.*, 2002]. Due to this agreement we then used the empirical relationship (Eq. 5.6) between the 442 and 547 nm phytoplankton absorption relationship (the largest difference occurs at this wavelength) to solve for the size parameter, S_f [*Ciotti et al.*, 2002], and finally using the same formulation obtain an estimate of [*Chl*] mg m^{-3}. With the size parameter, S_f empirical modeling and the averages slopes of *Babin et al.* [2003] we can estimate the absorption of each constituent at all visible wavelengths. Finally we compare our size parameter, S_f, based [*Chl*] mg m^{-3} retrieval with the MODIS [*Chl*] mg m^{-3} [*O'Reilly et al.*, 1998] product and explain the differences.

Bibliography

Aires, F., C. Prigent, W.B. Rossow and M. Rothstein (2001), A neural network approach including first guess for retrieval of atmospheric water vapor, cloud liquid water path, surface temperature, and emissivities over land from satellite microwave observations, J. Geoph.l Res., 106, 14887-14907, (2001).

Aires F., C. Prigent, and W.B. Rossow, "Neural network uncertainty assessment using Bayesian statistics: A remote sensing application," neural Comput., 16, 2415-2458, (2004)

Albert A. and C. D. Mobley, "An analytical model for subsurface irradiance and remote sensing reflectance in deep and shallow case-2 waters," Opt. Express 11, 2873-2890, (2003).

Austin, R. W. and T. J. Petzold, "The determination of the diffuse attenuation coefficient of sea water using the coastal zone color scanner," in Oceanography from Space, J. F. R. Gower, ed. Plenum, New York, (1981).

Babin, M., D. Stramski, G. M. Ferrari, H. Claustre, A. Bricaud, G. Obolensky, and N. Hoepffner, "Variations in the light absorption coefficients of phytoplankton, nonalgal particles, and dissolved organic matter in coastal waters around Europe," J. Geophys. Res., 108, 4:1-20, (2003).

Babin, M., A. Morel, V. Fournier-Sicre, F. Fell and D. Stramski."Light scattering properties of marine particles in coastal and oceanic waters as related to the particle mass concentration." Limnology and Oceanography, 48, 843-859, (2003).

Bricaud, A., M. Babin, A. Morel, and H. Claustre, "Variability in the chlorophyll-specific absorption coefficients of naturnal phytoplankton: Analysis and parameterization," J. Geophy. Res., 100, 13321-13332, (1995).

Bukata, R. P., J. H. Jerome, K. Y. Kondratyev, and D. V. Pozdnyakov, "Optical Properties and Remote Sensing of Inland and Coastal Waters," (CRC Press 1995).

Carder, K.L., Hawes, S.K., Baker, K.A., Smith, R.C., Steward, R.G., and Mitchell, B.G. "Reflectance model for quantifying chlorophyll a in the presence of productivity degradation products." J. Geophys. Res. 96: 20599-20611, (1991).

Carder, K. L., F. R. Chen, Z. P. Lee, S. K. Hawes, and D. Kamykowski, "Semianalytic Moderate-Resolution Imaging Spectrometer algorithms for chlorophyll-a and absorption with bio-optical domains based on nitrate-depletion temperatures," J. Geophys, Res. 104, 5403–5421 (1999).

Chang, G., K. Mahoney, A. Briggs-Whitmire, D.D.R. Kohler, C.D. Mobley, M. Lewis, M.A. Moline, E. Boss, M. Kim, W. Philpot, and T.D. Dickey, "The New Age of Hyperspectral Oceanography", Oceanography, Vol. 17, 16-23, (2004).

Ciotti, A. M., M. R. Lewis, and J. J. Cullen, “Assessment of the relationships between dominant cell size in natural phytoplankton communities and the spectral shape of the absorption coefficient,” Limnol. Oceanogr., 47, 404–417 (2002).

Crone, L. and D. Crosby, “Statistical applications of a metric on subspaces to satellite meteorology”, Technometrics, 37, 324-328, (1995).

Cybenko, G. “Approximation by superpositions of a sigmoidal function,” Math. Control Signals Syst., 2, 303-314, (1989).

Doerffer, R., and Schiller, H. “Neural network for retrieval of concentrations of water constituents with the possibility of detecting exceptional out of scope spectra.” IEEE 2000 International Geoscience and Remote Sensing Symposium, Honolulu, Hawaii USA, p. 714-717, (2000).

Doerffer, R., Heymann, K., and Schiller, H. “Case 2 water algorithm for the medium resolution imaging spectrometer (MERIS) on ENVISAT.” In: Proceedings of the ENVISAT validation workshop, 9-13 December 2002, ESA report, (2002).

Doerffer, R., and Schiller, H. “The MERIS case 2 water algorithm.” Int. J. Remote Sens., (2006).

Foresee, F.D., and M.T. Hagan, "Gauss-Newton approximation to Bayesian regularization," Proceedings of the 1997 International Joint Conference on neural networks, 1997, pp. 1930–1935, (1997).

Garver A. H. and D. A. Siegel, "Inherent optical property inversion of ocean color spectra and its biogeochemical interpretation.1. Time series from the Sargasso Sea," J. Geophys, Res. 102, 18607–18625 (1997).

Gilerson, A., Zhou, J., Hlaing, S., Ioannou, I., Schalles, J., Gross, B., Moshary, F. and Ahmed, S., "Fluorescence component in the reflectance spectra from coastal waters. Dependence on water composition," *Opt. Express*, 15 (24), 15702– 15721, (2007).

Gitelson, A., J. F. Schalles, and C. M. Hladik, "Remote chlorophyll-a retrieval in turbid, productive estuaries: Chesapeake Bay case study," Remote Sens. Environ. 109, 464-472, (2007).

Gordon H. R. and A. Morel, "Remote Assessment of Ocean Color for Interpretation of Satellite Visible Imagery: A Review", R. T. Barber, C.N. K. Mooers, M. J. Bowman, and B. Zeitzschel, eds. Springer-Verlag, New York (1983).

Gordon, H. R., D. K. Clark, J. W. Brown, O. B. Brown, R. H. Evans, and W. W. Broenkow, "Phytoplankton pigment concentrations in the Middle Atlantic Bight: comparison of ship determinations and CZCS estimates," Appl. Opt. 22, 20–36,

(1983).

Gordon, H.R., Brown, O.B., Evans, R.H., Brown, J.W., Smith, R.C., Baker, K.S., and Clark, D.K. “A semianalytic radiance model of ocean color.” J. Geophys. Res. 93: 10,909-10,924, (1988).

Gordon, H. R. and M. Wang, "Retrieval of water-leaving radiance and aerosol optical thickness over the oceans with SeaWiFS: a preliminary algorithm," Appl. Opt. 33, 442-452, (1994).

Gross, L., S. Thiria, and R. Frouin, “Applying artificial neural network methodology to ocean color remote sensing”. Eco. Model., 120, 237-246 (1999).

Hamre, B., O. Frette, S. R. Erga, J. J. Stamnes and K. Stamnes, “Paramterization and analysis of the optical absorption and scattering coefficients in a western Norwegian fjord: a case II water study”, Appl. Opt. 42, 883-892 (2003)

Hoge, F. E. and P. E. Lyon, “Satellite retrieval of inherent optical properties by linear matrix inversion of oceanic radiance models: an analysis of model and radiance measurement errors,” J. Geophys. Res. 101, 16631–16648 (1996).

Hooker, S. B., G. Lazin, G. Zibordi, S. McLean.” An Evaluation of Above- and In-Water Methods for Determining Water-Leaving Radiances.” *J. Atmos. Oceanic Technol.*, 19, 486–515, (2002).

Horrnik, K., M. Stinchcombe and H. White, “multilayer feedforward networks are universal approximators.” neural networks, 2, 359-366, (1989).

Ioannou, I., Gilerson, A., Gross, B., Moshary F., and Ahmed, S.,” A neural network approach to retrieve the inherent optical properties of the ocean from the observations of MODIS,” *Applied Optics*, in press, 2011.

IOCCG Dataset, http://www.ioccg.org/groups/lee_data.pdf, Z. P. Lee, (2003).

IOCCG,” Remote Sensing of Inherent Optical Properties: Fundamentals, Tests of Algorithms, and Applications.” Report 5 ZhongPing Lee, ed., (2006).

IOCCG, "Why Ocean Colour? The Societal Benefits of Ocean-Colour Technology," Report 7 (IOCCG, Dartmouth, Canada, 2008).

Kirk, J. T. O., ”Light and Photosynthesis in Aquatic Ecosystems.” Cambridge University Press, Cambridge, 509 pp. (1994).

Lee, Z. P., “Visible-infrared remote-sensing model and applications for ocean waters,” Ph.D. dissertation ~Department of Marine Science, University of South Florida, St. Petersburg, Fla., (1994).

Lee, Z. P., K. L. Carder, R. G. Steward, T. G. Peacock, C. O. Davis, and J. S. Patch, "An empirical algorithm for light absorption by ocean water based on color," J. Geophys. Res. 103, 27967–27978 (1998).

Lee, Z. P., K. L. Carder, C. D. Mobley, R. G. Steward, and J. S. Patch, "Hyperspectral remote sensing for shallow waters: 2.Deriving bottom depths and water properties by optimization," Appl. Opt. 38, 3831–3843, (1999).

Lee, Z. P., K. L. Carder, R. A. Armone, "Deriving inherent optical properties from water color: A multiband quasi-analytical algorithm for optically deep waters," Appl. Opt., 41, 5755-5772, (2002).

Lee, Z. P., http://www.ioccg.org/groups/Software_OCA/QAA_v5.pdf, (2009).

Levenberg, K."A Method for the Solution of Certain Non-linear Problems in Least Squares." Quarterly of Applied Mathematics, 2(2):164–168, Jul. (1944).

Livingstone, D.S. (ed.), "Artificial neural networks: Methods and applications." (Humana Press, New Jersey, 2009).

Loisel, H., D. Stramski, B. G. Mitchell, F. Fell, V. Fournier- Sicre, B. Lemasle, and M. Babin," Comparison of the ocean inherent optical properties obtained from measurements and inverse modeling" Appl. Opt. 40, 2384–2397 (2001).

MacKay, D.J.C., “Bayesian interpolation,” neural Computation,Vol. 4, No. 3, 1992, pp. 415–447, (1992).

Marquardt, D.W. “An Algorithm for the Least-Squares Estimation of Nonlinear Parameters.” SIAM Journal of Applied Mathematics, 11(2):431–441, (1963).

Mobley, C. D., “Light and Water: Radiative Transfer in Natural Waters”, (Academic Press, New York, 1994).

Mobley, C. D. and L. K. Sundman, HYDROLIGHT 5, Sequoia Scientific, Inc. (2008).

MODIS Aqua SRF

http://oceancolor.gsfc.nasa.gov/DOCS/RSR/Aqua_detdep_RSRs.txt

Morel, A., “Optical properties of pure water and pure sea water,” in Optical Aspects of Oceanography, N. G. Jerlov and E. S. Nielsen, eds., Academic, pp. 1-24, (New York, 1974).

Morel, A. and L. Prieur, “Analysis of variations in ocean color,” Limnol. Oceanogr. 22, 709–722 (1977).

Morel, A. and Bricaud, A.,”Theoretical results concerning light absorption in a discrete medium, and application to specific absorption of phytoplankton.” Deep-Sea Res., 28,

1375–1393, (1981).

Morel, A.”Light and marine photosynthesis: A spectral model with geochemical and climatological implications,” *Progress in Oceanography,* 26, 263-306, (1991).

Morel, A., D. Antoine and B. Gentili. "Bidirectional reflectance of oceanic waters: accounting for Raman emission and varying particle scattering phase function." Applied Optics 41(30): 6289-6306, (2002).

Morel, A., Gentili, B., Claustre, H., Babin, M., Bricaud, A., Ras, J., and Tieche, F.,” Optical properties of the ‘‘clearest’’ natural waters,” Limnol. Oceanogr. ,52(1), 217–229, (2007).

Oishi, T., Y. Takahashi, A. Tanaka, M. Kishino, and A. Tsuchiya, “Relation between the backward as well as total scattering coefficients and the volume scattering functions by cultured phytoplankton,” J. School Mar. Sci. Technol. Tokai Univ., 53, 1-15, (2002).

O’Reilly, J., S. Maritorena, B. G. Mitchell, D. Siegel, K. L. Carder, S. Garver, M. Kahru, and C. McClain, “Ocean color chlorophyll algorithms for SeaWiFS,” J. Geophys. Res. 103, 24937–24953 (1998).

Pope, R. and E. Fry, “Absorption spectrum _380–700 nm_ of pure waters: II. Integrating cavity measurements,” Appl.Opt., 36, 8710–8723, (1997).

Preisendorfer, R. W., “Hydrologic Optics,” U.S. Department of Commerce, NOAA, ERL (1976).

Press, W. H., B. P. Flannery, S. A. Teukolsky, and W. T. Vetterling, in Numerical Recipes in FORTRAN: The Art of Scientific Computing, 2nd ed., pp. 655– 675, (Cambridge U. Press, 1992).

Roesler , C. S. and M. J. Perry, “In situ phytoplankton absorption, fluorescence emission, and particulate backscattering spectra determined from reflectance,” J. Geophys. Res. 100, 13279–13294, (1995).

Sathyendranath, S., F. E. Hoge, T. Platt, and R. N. Swift, “Detection of phytoplankton pigments from ocean color: improved algorithms,” Appl. Opt. 33, 1081–1089 (1994).

Sathyendranath, S., Platt, T., Stuart, V., Irwin, B. D., Veldhuis, M. J.W., Kraay, G.W. and Harrison,W. G., “Some bio-optical characteristics of phytoplankton in the NW Indian Ocean.” Mar. Ecol. Prog. Ser., 132, 299–311, (1996).

Schiller, H., R. Doerffer, “Neural network for emulation of an inverse mode-operational derivation of case II water properties from MERIS data”. International

Journal of Remote Sensing, 20(9), 1735-1746, (1999).

Schiller, H., and Doerffer, R. “Improved determination of coastal water constituent concentrations from MERIS data.” IEEE Trans. Geosci. Remote Sens. 43: 1585-1591, (2005).

Sosik, H. M. and Mitchell, B. G. “Absorption, fluorescence, and quantum yield for growth in nitrogen-limited Dunaliella tertiolecta.” Limnol. Oceanogr., 36, 910–921, (1991).

Stramski, D., A. Bricaud, and A. Morel, “Modeling the inherent optical properties of the ocean based on the detailed composition of the planktonic community,” Appl. Opt. 40, 2929-2945 (2001).

Stuart, V., Sathyendranath, S., Platt, T., Maass, H. and Irwin, B. D., “Pigments and species composition of natural phytoplankton populations: effect on the absorption spectra.” J. Plankton Res., 20, 187–217, (1998).

Sydor, M., R. Arnone, R. W. Gould, G. E. Terrie, S. D. Ladner, and C. G. Wood, “Remote-sensing technique for determination of the volume absorption coefficient of turbid water,” Appl.Opt. 37, 4944–4950 (1998).

Tanaka, A., M. Kishino, R. Doerffer, H. Schiller, T. Oishi and T. Kubota,

"Development of a neural network Algorithm for Retrieving Concentrations of Chlorophyll, Suspended Matter and Yellow Substance from Radiance Data of the Ocean Color and Temperature Scanner", Journal of Oceanography, 60,519-531, (2004).

Tyler J. E. and R. W. Preisendorfer, "In The Sea, Vol. 2," M. N. Hill, Ed., Interscience, New York (1962).

Wang, P., E. S. Boss, and C. Roesler, "Uncertainties of inherent optical properties obtained from semianalytical inversions of ocean color" Appl. Opt. 44, 4074–4085, (2005).

Werdell P. J., Bailey S. W," An improved in-situ bio-optical data set for ocean color algorithm development and satellite data product validation," *Remote Sensing of Environment*, 98, 122-140, (2005).

Zhou, J., A. Gilerson, I. Ioannou, S. Hlaing, J. Schalles, B. Gross, F. Moshary, and S. Ahmed, "Retrieving quantum yield of sun-induced chlorophyll fluorescence near surface from hyperspectral in-situ measurement in productive water," Opt. Express, 16, 17468-17483, (2008).